TABLE OF CONTENTS

	Page	
SUMMARY	1	1/A5
INTRODUCTION	2	1/A6
DESCRIPTION OF THE EXPERIMENT	5	1/A9
Wind Tunnel	5	1/A9
Test Section	7	1/A11
Test Conditions	8	1/A12
Measurements Obtained	9	1/A13
Instrumentation	10	1/A14
RESULTS AND DISCUSSION	17	1/B7
Flow Condition "A"	17	1/B7
Flow Condition "C"	23	1/B13
Flow Conditions "B"	25	1/C1
CONCLUSIONS	27	1/C3
FIGURES	28	1/C4
APPENDIX A - Mean-Velocity Data	90	2/A3
APPENDIX B - Additional Inlet-Flow Measurements	110	2/B9
APPENDIX C - List of Symbols	115	2/B14
REFERENCES	116	2/C1

NAS 1.26:3067
COMPLETED
FEB 1 0 1979

NASA Contractor Report 3067

Study of Mean- and Turbulent-Velocity Fields in a Large-Scale Turbine-Vane Passage

Douglas A. Bailey

CONTRACT NAS3-19752
FEBRUARY 1979

NASA

123

NASA Contractor Report 3067

Study of Mean- and Turbulent-Velocity Fields in a Large-Scale Turbine-Vane Passage

Douglas A. Bailey
United Technologies Research Center
East Hartford, Connecticut

Prepared for
Lewis Research Center
under Contract NAS3-19752

National Aeronautics
and Space Administration

Scientific and Technical
Information Office

1979

TABLE OF CONTENTS

	Page
SUMMARY	1
INTRODUCTION	2
DESCRIPTION OF THE EXPERIMENT	5
Wind Tunnel	5
Test Section	7
Test Conditions	8
Measurements Obtained	9
Instrumentation	10
RESULTS AND DISCUSSION	
Flow Condition "A"	17
Flow Condition "C"	23
Flow Conditions "B"	25
CONCLUSIONS	27
FIGURES	28
APPENDIX A - Mean-Velocity Data	90
APPENDIX B - Additional Inlet-Flow Measurements	110
APPENDIX C - List of Symbols	115
REFERENCES	116

Study of Mean- and Turbulent- Velocity Fields In A Large-Scale Turbire-Vane Passage

by

Douglas A. Bailey

SUMMARY

An experimental investigation was conducted on the mean- and turbulent-velocity fields in a large-scale turbine inlet-guide-vane passage. The experiment was performed in a 210-mm pitch, 272-mm axial chord model in the United Technologies Research Center (UTRC) Low-Speed Wind Tunnel at an inlet Mach number of 0.07. The Reynolds number, based on the axial chord and the inlet velocity, matched seal-level, take-off conditions for modern gas-turbine engines. Laser-doppler velocimetry, and to a lesser extent hot-wire anemometry, was employed to measure three components of the mean velocity and the six turbulent stresses at four planes within the passage. One variation in the turbulent inlet boundary-layer thickness and one variation in the blade aspect ratio (span/axial chord) were studied. A longitudinal vortex (passage vortex) was clearly identified in the exit plane of the passage for the three test cases.

The maximum turbulence intensities within the longitudinal vortex were found to be on the order of 2 to 4 percent, with large regions appearing non-turbulent. Since a turbulent wall boundary layer was the source of vorticity that produced the passage vortex, these low turbulence levels were not anticipated.

For the three test cases studied, the lateral velocity field extended significantly beyond the region of the longitudinal velocity defect. Changing the inlet boundary-layer thickness produced a difference in the location, the strength and the extent of the passage vortex. Changing the aspect ratio of the blade passage had a measurable but less significant effect.

INTRODUCTION

It has been recognized for some time that an important portion of turbine loss and heat transfer is associated with the passage secondary flow in the endwall region. This secondary flow is related to the curvature of the inviscid streamlines, which produces a lateral pressure gradient. In response to this pressure gradient, the low-momentum flow in the endwall boundary layer develops a lateral velocity component, which convects low-momentum fluid toward the convex surface of the passage, developing a three-dimensional separation line from an upstream position on the concave surface to a downstream position on the convex surface. The flow upstream of this separation line is a three-dimensional boundary layer; however, downstream of the separation line the boundary-layer assumptions are no longer valid because of the large velocities normal to the endwall. This is especially so near the convex surface, where a longitudinal vortex develops. This vortex has a significant influence on the flow in that region, since it convects high-momentum freestream fluid to the near-wall region, thereby increasing viscous losses and heat transfer.

Since endwall losses are significant to overall gas turbine performance (ref. 1) efforts have been underway to understand these flows, to predict their behavior, and to eventually minimize passage losses through optimally-designed passage contours. A number of these investigations of three-dimensional flows have provided some elucidation of the features of the flow. Rohlik and others (ref. 2) measured a concentration of passage losses near the suction surface-endwall junction. Herzig and others (ref. 3) used smoke traces to visualize the cross-passage flow, and also observed the roll-up of the flow near the suction surface and the formation of a passage vortex. An indirect measure of the influence of the vortex has been provided by Blair (ref. 4), who observed high heat-transfer rates on a passage endwall near the suction surface. Pressure-loss measurements within a passage were recently obtained by Sjolander (ref. 5) and a detailed picture of the passage vortex has been provided by Langston, Nice and Hooper (ref. 6). The development of the passage vortex, as well as the total pressure defect within the vortex, was well documented in both of these experiments. Aside from these fundamental studies, many tests have been conducted on cascades where only the inlet and exit conditions were measured and the losses determined for the specific test case. Examples of these tests are mentioned by Dunham (ref 7) and Ainley (ref. 1).

In addition to the experimental effort, there have also been several analytical studies of this phenomenon. The original analytical efforts were directed toward laminar passage flow, even though the flow in a turbine passage is turbulent. This direction proved fruitful, since, as Hansen and Herzig (ref. 8) concluded after comparing turbulent and laminar flows, the

turbulent effects are not qualitatively dominant in curved channel flows. Upstream of the separation line, the flow is a three-dimensional boundary layer and several analytical solutions exist for flow in this region. Sowerby (ref. 9) and Loos (ref. 10) obtained similarity solutions for parabolic streamlines; Mager and Hansen (ref. 11) for circular streamlines. For general streamlines through a thin-blade turbine-type passage, Hansen and Herzig (ref. 8) obtained excellent agreement between a series solution and their experimental results. In addition, they noted a stronger cross flow for thicker inlet boundary layers. Except for the region of the passage vortex, this type of solution is rather complete for laminar endwall flow through a lightly loaded thin-blade passage. Although laminar boundary-layer theory has provided insight into the nature of flows through an idealized passage, it is not applicable to the important region of the passage vortex.

Another method of considering the generation of secondary flow in curved channels has been extensively developed by Hawthorne (ref. 12). He neglected viscous effects within the curved section of the channel and considered the convection of vortex lines in the channel. Many analytical and experimental investigations have been conducted on inviscid secondary flows, and these are summarized by Hawthorne (ref. 13). However, those methods require the secondary flow to be a small perturbation on the longitudinal velocity (this is not the case for thin endwall boundary layers) and they give no information about viscous losses. Recently, Denton (ref. 14 and 15) and Stuart and Hetherington (ref. 16) have developed computational procedures for predicting three-dimensional, inviscid flows. These methods are used to estimate the exit flow angles from compressor and turbine stages. This is a valuable tool for the design of the next stage; however, their applicability to endwall boundary layers has not been established, since inviscid solutions will not predict local skin-friction and heat-transfer rates. Therefore, to attack the important questions of loss and heat transfer, computational procedures for predicting three-dimensional, viscous flows have been initiated.

Computational procedures have been developed for the prediction of viscous secondary flows by Briley (ref. 17), Patankar and Spalding (ref. 18) and Ghia and others (ref. 19). In fact, both Dodge (ref. 20) and Briley (ref. 21) have attempted to solve the endwall flow through a typical turbine vane. The evaluation of these studies has been limited, however, due to the lack of data for turbine endwall flows. This is especially so for the turbulence within a developing passage vortex.

The goals of this experimental program were, therefore, two-fold. The primary goal was the acquisition of precise mean-velocity measurements of the secondary flow through a turbine-vane passage. These results could be used in the evaluation of analytical and computational procedures, which have or may be developed for the prediction of such secondary flows.

The other goal of this program was documentation of the turbulence of the flow, as it developed into a passage vortex, in sufficient detail so that turbulence models could be evaluated.

The experimental approach used to satisfy the above goals was to simulate a turbine-passage flow in a large-scale test section, thus permitting high spatial resolution for velocity measurements. An additional feature of the test section was the suppression of the horseshoe vortex, which, therefore, resulted in an isolated passage vortex. Within the test section, mean velocities and turbulent stresses were measured, documenting the development of a passage vortex from a turbulent inlet boundary layer. Most of the measurements were obtained with a laser-Doppler velocimeter, thus eliminating the uncertainty associated with intrusive sensors. Three different test conditions, consisting of variations in inlet boundary-layer thickness and test-section aspect ratio (span/axial chord), were studied.

The results showed that the maximum turbulence level within the passage vortex was low in comparison with maximum levels obtained in turbulent boundary layers. Some regions of the vortex were non-turbulent. When the thickness of the inlet boundary layer was varied, the size and location of the passage vortex was significantly altered. Changing the test-section span had a measurable, but less significant, effect on the passage vortex.

DESCRIPTION OF THE EXPERIMENT

Wind Tunnel

The experiment was conducted in a low-speed, general-purpose wind tunnel. The tunnel, as illustrated in figure 1, consisted of a fan, a large area straight duct (which included a honeycomb section and four damping screens), a contraction, a test-section approach duct, a test section, a diffuser and recirculating lines. The twelve-bladed centrifugal fan, operating at 1770 RPM, produced a static pressure increase of 2300 pascals (230 mm of H_2O) at a flow rate of 280 m^3/min. The fan was equipped with adjustable inlet guide vanes (vortex valve) which allowed steady, stall-free operation, as well as fine adjustment of the tunnel speed.

The fan discharged into the straight duct with jet flow; no effort was made to diffuse the flow. Although this is unconventional, the resulting flow is steady and avoids the instability that is associated with transitional stall in a diffuser. The alternative, a completely unstalled diffuser, would have been prohibitively long (ref. 22) for the required area ratio of 2.45. When the fan is of such capacity that the exit-flow dynamic head does not have to be recovered, this method is advantageous for obtaining steady flow. The small-scale turbulence from the fan-exit jet quickly decays in the honeycomb and damping screens, whereas transitional stall in a diffuser could produce large-scale oscillations which would not be attenuated by the screens.

The straight section was 1.83 m long, 0.71 m high and 0.56 m wide; it contained the honeycomb section and the damping screens. The honeycomb had hexagonal cells 140 mm long and 6.35 mm in diameter (flat surface to flat surface) and was located 0.33 m from the fan. The screens were made of 0.46 mm wire, with 2.1 mm wire spacings, which resulted in a near optimum (ref. 23) open area ratio of 60.8 percent. At a local velocity of 8 m/s the pressure-loss coefficient ($K = \Delta p/1/2\rho U^2$) for the four screens was measured at 4.3 and calculated at 3.9 (ref. 24). The screens were located 1.17, 1.42, 1.70 and 1.83 m from the fan.

Schubauer and others (ref. 23) have shown that damping screens have a greater attenuation of turbulence when the flow past the wires is laminar, rather than turbulent. This transition occurs at wire-diameter Reynolds numbers between 40 and 60. For low Reynolds-number flow past wires there is the additional advantage that the wire wakes remain laminar and, therefore, do not produce additional turbulence. High turbulence levels exist immediately downstream of damping screens when the flow past the wires is unstable. However, the turbulence produced by damping screens has a small length scale, of the order of the wire spacings, which rapidly decays to

turbulence levels near one percent. After one-percent turbulence levels are reached, the decay rate drastically decreases. However, a disadvantage of fine-wire laminar screens is that dust collecting on the wires will produce adverse effects, i.e., flow distortion. The finer the wire the more significant this effect. After considering the above mentioned behavior of damping screens, coarse-grid turbulent screens were selected to minimize the dust effects, realizing that the turbulence levels upstream of the contraction would be near one percent. The principal reason for this decision was that artificial seeding was to be used for the laser-Doppler velocimeter, and the seeding particles would be injected upstream of the screens to minimize the influence the injection would have on the uniformity of the test-section flow. In fact, to eliminate that adverse influence, the seeding particles were injected upstream of the honeycomb with the seeding jet normal to the wind-tunnel wall.

The contraction nozzle was 1.22 m long, with an exit height and width of 210 and 508 mm, respectively. The contraction ratio was 3.7 and the ratio of the length to exit height was 5.81, a gradual contraction. The curved surfaces of the contraction were cubic surfaces, which permitted a long radius of curvature at the regions of tangency with the inlet and exit surfaces. This minimized the adverse pressure gradients and insured a well-behaved boundary-layer flow. As a check on the design, tufts of yarn were used to visualize the exit flow and assured that no unsteadiness existed, as might be associated with local separation of the boundary layer.

The test-section approach duct connected the contraction exit to the test section. This duct served three purposes: (1) the skewed boundary layer that would develop in the two-dimensional contraction (ref. 25) was bled off at the entrance to the duct; (2) two-dimensional boundary layers of various thicknesses were developed along the 0.61-m length of the duct; and (3) the potential flow was permitted to develop upstream of the test section without being influenced by the pressure field at the exit of the contraction.

The boundary-layer thickness at the test-section inlet was varied by adjusting the openings of the bleed slots. These slots were 9.5 mm wide and inclined 30° from the tunnel surface. They were located on all four surfaces at distances of 0.025, 0.432 and 0.546 m from the contraction exit. Adjustable covers, on the outside of the tunnel, permitted control of the bleed rates. In addition to these bleed slots, additional slots were located on the surfaces between the test-section leading edge and the approach duct. The purpose of these latter slots was to bleed off the boundary layer that would have developed downstream of the last slot and could have caused a recirculation region at the leading edges of the test section. These slots also minimized the leading-edge horseshoe vortices at the junction of the test-section leading edge and the endwall. This important point will be discussed in greater detail in the description of the test section.

The flow from the test-section approach duct passed through the test section and was decelerated in a 2-m long diffuser. The exhaust from the diffuser was recirculated to the fan inlet through flexible hoses. This was done to minimize the amount of LDV seeding particles in the air surrounding the wind tunnel.

The test-section inlet flow was measured in the planes of the test section pitch (vertical) and span (horizontal) 0.46 m downstream of the contraction. Both the total pressure and the velocity were measured using Kiel probes and cylindrical hot-film sensors. These results, shown in figure 2, indicate that the core flow was uniform to within one percent of the centerline value for both the velocity and the pressure coefficient. The slight variation of the velocity in the vertical plane was caused by the influence of the test section. At the same location, the turbulent characteristics were measured with a hot-wire sensor (4 μm in diameter and 1.25 mm in length). The intensity of the longitudinal component of turbulence, $\sqrt{\bar{u}'^2}/U_\infty$, was 0.005 ±0.0015. One of the lateral components of turbulence was measured, and assuming the two lateral components were equal, the total turbulence, $\sqrt{1/3\ (\bar{u}'^2 + \bar{v}'^2 + \bar{w}'^2)}/U_\infty$, was 0.007. The possible attenuation of high-frequency energy due to the finite length of the sensor and the effect of the filters used (20-10,000 Hz) were both investigated and found to be negligible (refs. 26 and 27). The power-spectral density of the longitudinal component of turbulence was measured (fig. 3) with a one-third octave analyzer and was found to be in good agreement with the Liepmann spectrum (ref. 28), indicating that the turbulence was in a normal state of decay, that the wakes from the fan blades had been completely attenuated and that the measurements were not influenced by vibrations of the hot-wire support prongs. Using Taylor's hypothesis (ref. 28) the longitudinal integral length scale was calculated from the auto-correlation of the signal and found to be 52 mm.

Test Section

The turning-passage test section was approximately ten times larger than typical first-stage turbine inlet-guide vanes for modern gas turbines. The surface coordinates of the actual test section are listed in table 1 and the surface shapes shown in figure 4. The test section was two-dimensional, with a 508 mm span and a 210 mm pitch. The mid-span, wall, static-pressure distribution was measured and compared to the pressure distribution for an equivalent cascade potential flow. After adjusting the exit tail-boards and the inlet bleed slot, excellent agreement was obtained between the measured and calculated flow, as shown in figure 5.

The test section was a channel passage, rather than a cascade passage. This permitted the boundary layers, which would impinge on the leading edges of the test section, to be bled off, thus eliminating the intense vorticity normally observed in this area (refs. 5 and 6). These vortices, sometimes called horseshoe vortices, have an extreme effect on the endwall flow near the leading edge, as can be inferred from the heat-transfer measurements of Burbank and others (ref. 29). The vortices are then convected into the passage, and, consequently, disturb the inlet flow uniformity (refs. 5 and 6). Some specific studies have been conducted of these leading edge vortices (refs. 30-35), but there is no method to predict the effect they would have on the inlet flow; therefore, detailed measurements of the vortices would be required as a starting condition for any calculation with leading-edge vortices. To eliminate this problem and, also to study the isolated effect of a passage vortex, the horseshoe vortex was suppressed in this experiment. This was accomplished by bleeding off the boundary layers that would normally impinge on the blade leading edges at the junction with the endwall.

Test Conditions

The experiment was conducted at a test-section Reynolds number, based on the axial chord and the inlet velocity, of 4.6×10^5, which is typical of sea-level, take-off conditions for modern gas-turbine engines. No attempt was made to simulate compressibility effects; the maximum Mach number in the test section was equal to 0.3. Standard air was used for the test fluid.

The experiment consisted of three different test conditions: "A", a thick inlet boundary layer with a blade aspect ratio of 0.617; "B", a thin inlet boundary layer with a blade aspect ratio of 0.617; and "C", a thin inlet boundary layer with a blade aspect ratio of 1.866. Comparison between flow conditions "A" and "B" shows the effect of inlet boundary-layer thickness variation; while comparison between flow conditions "B" and "C" shows the effect of blade aspect ratio variation on the secondary flow.

The lower aspect ratio geometries were obtained by using splitter plates. For condition "B", the plate extended just upstream of the test section, while for condition "A", the plate extended the full length of the test-section approach duct, so that a thick boundary layer would be present on both endwalls of the test section. The leading edge of the splitter plates was approximately a four-to-one ellipse. Boundary-layer trip wires were used to insure that the inlet boundary layers were fully turbulent.

The thin inlet boundary layers were generated using all three of the bleed slots in the approach duct to remove the boundary layer that developed in the duct. The last bleed slot was 64 mm upstream of the test section inlet. Just downstream of this bleed slot, 50 mm from the test section, a 0.51-mm diameter wire was used to start a turbulent boundary layer. The

Reynolds number, based on the wire diameter, was 900, which more than satisfied Preston's recommendation (ref. 36) that the Reynolds number exceeds 600 for a fully turbulent boundary layer. The distance from the wire to the test section was more than the approximate 100 wire diameters needed for the flow distortions, caused by the wire, to be completely diffused (ref. 37). The thick inlet boundary layer was generated with the last two bleed slots sealed and a 2.38-mm trip wire 530 mm upstream of the test section. Identical trip wires were used at the same locations on the splitter plates, so that the boundary layers at the test section inlet would be symmetrical about the mid-span.

Measurements Obtained

The mean and fluctuation velocities were measured with hot-wire/hot-film anemometers and laser-Doppler velocimetry (LDV) at a variety of locations in the test section. Velocity profiles were measured normal to the test-section endwall at twelve locations, defined by the intersections of four equi-potential planes with three streamlines, based on the equivalent cascade potential flow. The streamlines represented the 20, 50 and 80 percent mass-flow lines; the equi-potential planes extended from just inside the passage to the passage throat. These positions are shown in figure 6 and also given in table 2. Aside from referring to the measurement positions by numbers, it is helpful to number the measurement planes as is shown in figure 6.

Before discussing the particular measurements that were acquired, it is appropriate to define the coordinate system and the associated velocity components. The x-axis and the velocity component U were in the direction of the undisturbed core flow. The y-axis and the velocity component V were parallel to the plane of the endwall, from the pressure to the suction surface, and perpendicular to the x-axis. The z-axis and the velocity component W were perpendicular to the endwall in the direction from the endwall to the mid-span.

Of the three flow conditions to be tested, flow condition "A" with its thick inlet boundary layer was expected to produce the most clearly defined passage vortex. It was therefore chosen to be the most completely documented flow condition. At three locations along the inlet plane, the mean velocity components parallel to the endwall and the longitudinal turbulence were measured. Inside the blade passage, positions 4 through 12 in figure 6, measurements were made of the three components of mean velocity and the six turbulent stresses. Flow condition "B" differed from condition "A" in that the inlet boundary layer was thinner. For case "B" inlet mean velocities parallel to the endwall were measured, and farther inside the passage, at two locations near the blade suction surface, detailed mean-flow and turbulence

data were taken. Flow condition "C" was a thin inlet boundary-layer and a high aspect-ratio case. Data taken for this case consisted of inlet-flow mean-velocity measurements, limited mean-velocity and turbulence information away from the blade suction surface, and detailed flow measurements at two locations near the blade suction surface. Details of the overall test-data matrix, for the three flow conditions, are given in table 3.

Other measurements obtained included those of the inlet core flow and the passage pressure distribution. Two boundary-layer measurements were also obtained for flow condition "A" at the intersection of the first equi-potential plane and the mid-span vane surfaces.

Instrumentation

General

The usefulness of laser-Doppler velocimetry (LDV) for the measurement of secondary and recirculating flows has been recognized for some time. One important feature of this method is the elimination of an intrusive sensor which can be critical in these types of flows (ref. 38). An additional advantage of LDV is the precision that is possible with an instrument that requires no calibration. Since cross flows that deviate only a few degrees from an inviscid flow can result in significant secondary-flow effects, this precision may well be necessary for secondary-flow measurements.

The actual measurement made in an LDV system is the measurement of the period of a Doppler signal. The measurement of time is one of the easiest and most precise measurements that can be made in a general laboratory. The challenge in using an LDV is, therefore, in designing a system free from biasing effects due to seeding or signal processing. There has been intense research on these topics, and methods to eliminate biasing, as well as general applications of LDV, have been presented at symposia (refs. 39-43), and more recently, published in book form (refs. 44-45). Because of these numerous publications no general discussion of LDV systems will be included in this report; the systems used will only be defined to the extent that the reader could reproduce the results.

The mean and fluctuating velocity components, in the x-y plane, parallel to the endwall (U, V, $\overline{u'^2}$, $\overline{v'^2}$ and $\overline{u'v'}$) were measured with a backscatter system. This optical system is schematically illustrated in figure 7. A 245-mm focal length lens was used to focus the beams that were originally 50 mm apart. The total angle between the beams was, therefore, 11.67°. This resulted in a focal volume 1.26 mm long and 0.13 mm in diameter, based

on the locations at which the light intensity is equal to e^{-2} times the intensity on the beam centerline. The laser was operated at the 0.5145-μm wavelength and at power levels near one watt for the entire experiment.

Off-axis collection was used for the measurement of velocity components normal to the endwall (W, $\overline{w'^2}$ and $\overline{u'w'}$), as is shown schematically in figure 8. For these measurements the transmitting and collecting lenses had focal lengths of 752 and 245 mm. The focal volume was considerably smaller for this arrangement that for the backscatter system, because the collecting optics only focused on a small section of the volume defined by the transmitting beams. The approximate dimensions were 0.32 mm length and 0.39 mm diameter. A Bragg cell was used to increase the frequency of one of the transmitting beams by 40 MHz. This was done to eliminate directional ambiguity, as well as to increase the number of cycles of the Doppler signal.

One additional optical arrangement was required to measure $\overline{v'w'}$. This arrangement was similar to that shown in figure 8, except that the transmitting optics were at 45° to the pressure surface. This permitted the measurement of $\overline{v'^2} + \overline{v'w'} + \overline{w'^2}$, from which $\overline{v'w'}$ could be derived.

The general system, including the data processing equipment, is shown schematically in figure 9. When the Bragg cell was used, the Doppler signals were shifted to a lower frequency, which was more practical for signal processing. Whether or not the signal had been shifted, the Doppler signal was filtered and amplified in the processor. This removed both the pedestal and noise. The filtered signal was then viewed on an oscilloscope, with the trigger level adjusted to select the Doppler signals that would be analyzed. When a Doppler signal triggered the oscilloscope, the Schmitt trigger output from the oscilloscope was used to start the digital processing of the current signal. This processing consisted of digitizing the Doppler signal and then using a 100 MHz and a 125 MHz clock to count the periods of four, five and eight zero crossings. For validation of the signal the ratios of these periods had to be within a prescribed fraction, typically 0.8 percent, of the expected value. An additional requirement was that the peak voltages between zero crossings must have exceeded a certain value for the next zero crossing to be counted. This voltage was adjusted while viewing the clipped digital signal, which operated the clocks, on another oscilloscope. These requirements for validation of the data eliminated essentially all of the spurious signals such as those that would be generated by multiple particles in the focal volume.

A peripheral system transferred valid data from the processor to the computer and then reset the processor. After a thousand velocity samples had been collected by the computer, a probability distribution of the velocity was plotted on the CRT display terminal. Before calculating the mean

and the variance of the velocity, data that were inconsistent with the overall probability distribution were rejected. Although this editing seldom resulted in the rejection of more than twenty or thirty samples, it was necessary since the anomalous data could be in the opposite end of the data bandwidth from the actual data. This could result in significant biasing of the velocity variance.

LDV Seeding

When LDV measurements are obtained in air, artificial seeding particles are normally required to obtain a high data rate. If these particles are sufficiently small and of low density their velocities will closely match the fluid velocity. However, as the particle size or density increases, the tendency of the particles to follow the flow decreases. Therefore, careful attention must be directed to the seeding problem. This is especially true in turbulent flows where the particles must follow the individual eddies, as well as the mean flow.

Several theoretical studies have been conducted on the response of a seeding particle to a turbulent eddy. These studies are summarized in reference 46 along with many practical suggestions for LDV applications. Based on those results, it was determined that sub-micron particles were required for this experiment. Merely obtaining small particles, however, is by no means the complete solution to the seeding problem. A further difficulty arises because the bonding forces of sub-micron particles are such that they are rarely found as single particles. Hence, de-agglomeration of the particles is of major importance. Particles are usually dispersed by passing compressed air through a fluidized bed containing the seeding material, but Marteney (ref. 47) has pointed out that this method seldom has the necessary energy to overcome the agglomeration forces. Marteney found that the shearing stresses in a capillary tube with a large pressure drop would provide the required energy to de-agglomerate sub-micron particles. It was also mentioned in this study that one of the forces of agglomeration is the capillary junctions between liquids absorbed on the surface of the particles; therefore, dry air should be used for the particle seeding.

A seeding system was therefore designed incorporating the above information. Titanium dioxide particles were used because of their small diameter, 0.22 μm, and the uniformity of their size. Dry compressed air was used in a fluidized bed to obtain a suspension of the particles. The air-particle mixture was then passed through a capillary tube 0.5 mm in diameter and 25 mm in length. The pressure drop through the tube was approximately 1.4×10^5 pascals. The flow from the capillary tube entered the wind tunnel upstream of the honeycomb with the jet normal to the wind tunnel wall. No direct measurements of de-agglomerated particle size were obtained, but there were several facts that indicate that the particles followed the flow. For flow condition "A", measurements of the longitudinal turbulence were obtained for the boundary-layer inlet profiles using both hot wire and LDV. The

similarity of these measurements indicated that the seeding particles followed the turbulent eddies. Before the seeding system was completely developed, and large seeding particles were present, they would appear at the pressure surface and cause the velocity probability distribution to skew toward the low velocity direction. This was the result of the larger particles not accelerating through the passage. This effect was eliminated when the final seeding system was developed.

From Marteney's results the seeding particles should have been single particles, approximately 0.2-μm. Melling and Whitelaw (ref. 46) have shown that the general equation for the response of a particle in a fluctuating flow can be greatly simplified if $\rho_p/\rho_f \gtrsim 10^3$ and the Stokes Number ($N_s = \sqrt{\nu/f d_p^2}$) is greater than 8. These assumptions are satisfied for the titanium dioxide particles, since $\rho_p/\rho_f = 3.5 \times 10^3$ and $N_s > 8$ implies $f < 6$ MHz. Therefore the following simplified equation governs the particle response

$$\frac{dU_p}{dt} + 18 \frac{\nu\rho_f}{d^2\rho_p} (U_p - U_f) = 0$$

the solution of the above equation is

$$\frac{U_p}{U_f} = (1 + 1/X)^{-1/2}$$

where

$$X = \left(\frac{18N_s^2}{\rho_p/\rho_f} \right)^2$$

For a frequency of 10,000 Hz, which is adequate for the inlet boundary layers, $x = 32700$ and $U_p/U_f = 0.99998$.

Precision

This experiment required the measurement of all the individual turbulent stresses, both shearing and normal. These quantities could be obtained from six orthogonal measurements, but this technique would require that all of the six measurements for a particular location would have to be obtained before one could analyze the results. Since it was felt to be more desirable to completely analyze data as soon as possible, it was decided to measure an additional mean and turbulence measurement in the plane of the endwall. This uncoupled the term $\overline{u'^2} + \overline{v'^2}$; it also provided a redundant mean measurement that could be used for comparison with the other mean measurements.

For one test case, flow condition "C", position 10, an extensive amount of data were obtained to determine the precision of the system and to establish the user's confidence. This was at the beginning of the program, flow condition "C" being the first measured. Velocity components were measured in three directions, horizontal, U_1, vertical, U_2, and 45^o from the vertical and horizontal, U_3. To insure the steadiness of the wind tunnel operation, the following procedure was carried out. Traverses were initiated at a location 25 mm from the endwall and traversed toward the wall. When the limiting location near the wall was reached the direction of the traverse was reversed and data were obtained to 70-mm from the endwall. Finally, the last data point would be obtained at the 25-mm location. The results of all these measurements are shown in figure 10. The exceptionally low scatter is worth noting.

To obtain insight into the flow, it is most useful to resolve these velocity components into longitudinal (streamwise) and lateral velocities. The first step in doing this is to define the longitudinal direction. The most useful definition is to choose the direction of the core-flow streamlines. This ensures that the lateral velocities (V and W) do indeed represent secondary circulation resulting from the presence of longitudinal vorticity. Requiring the core flow to have no lateral velocity, measurements of velocities U_1, U_2 and U_3 can be resolved into longitudinal (U) and lateral (V) velocities using the following equations and the related sketch:

$$U = U_1 \cos \theta + U_2 \sin \theta$$

$$V = -U_1 \sin \theta + U_2 \cos \theta$$

$$U = U_1 (\cos \theta - \sin \theta) + U_3 \sin \theta / \sin 45^o$$

$$V = -U_1 (\cos \theta + \sin \theta) + U_3 \cos \theta / \sin 45^o$$

$$U = U_2 (\sin \theta - \cos \theta) + U_3 \cos \theta / \cos 45^o$$

$$V = U_2 (\cos \theta - \sin \theta) - U_3 \sin \theta / \cos 45^o$$

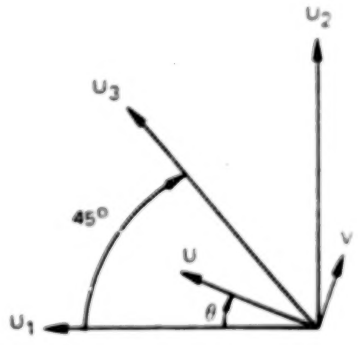

The angle θ was determined by the condition of zero lateral velocity in the core flow.

The resulting longitudinal and lateral velocities are shown in figure 11, where the circles indicate velocities obtained from U_1 and U_2, the squares from U_1 and U_3 and the triangles from U_2 and U_3. The U_1, U_2 and U_3 velocities that were used, were based on the smooth curves drawn through the data points in figure 10. The small variation in these measurements showed that there

was no biasing effect such as that observed by Seashultz (ref. 48) and Whiffen (ref. 49). With the exception of the measurement closest to the wall, where the reflected beam interfered with the scattered light to produce a poor signal-to-noise ratio, the variation in the measurement was generally less than one percent. The core-flow total velocities measured by the three different methods were 92.01, 92.10 and 92.06 m/s, and the velocity angles were 60.60°, 60.63° and 60.54°.

It is instructive to compare the precision of the LDV measurements with that of a hot-wire anemometer. A typical hot-wire calibration curve is shown in figure 12, where a least-mean-square curve has been fitted to the data. Although this appears to be an excellent fit, the maximum deviation of the data from the calibration curve corresponded to an error of 0.9 percent in velocity. This by itself is somewhat larger than the LDV scatter, and, in addition, it should be emphasized that this would be expected to be only a small portion of the total hot-wire error since it is well known that calibration curves continually change with time (ref. 50). It is, therefore, unlikely that the lateral velocities shown in figure 11 could be measured with hot-wire anemometry.

LDV Background Turbulence Levels

During the preliminary LDV measurements in the test section, it was noted that the turbulence levels were somewhat higher than those obtained with hot-wire anemometers. An investigation of this effect was conducted in an extremely low-turbulence one-inch diameter jet. It was learned that the LDV system had a background noise level whose variance was approximately one percent of the mean velocity being measured. When only a component of the total velocity was measured, the noise level was approximately one percent of the measured component. This result was found to be relatively independent of the jet velocity, the seeding rate and the trigger level of the oscilloscope. An attempt was made to isolate and reduce this noise level but it was unsuccessful. When a continuous sine wave was used as input to the processor the noise levels were near 0.1 percent. Apparently the noise was in the photo-multiplier, which was interchanged without an effect, or a result of the seeding, noise in the scattered light or laser noise.

Although this noise level was high in comparison with hot-wire anemometry, it was not felt to be detrimental to the experiment, since turbulence levels in the secondary flow were considerably higher than the LDV noise level.

While testing the noise level of the LDV a comparison was made of the mean-velocity measurements obtained with the LDV and a total pressure probe. These tests were conducted in air with jet velocities equivalent to dynamic heads of 25 mm, or less, of water. Within the precision of the micro-manometer,

which could resolve 0.025 mm of water, no difference in the velocity measurements could be detected.

Hot-Wire and Hot-Film Anemometry

Although hot-wire/hot-film anemometry has the limitations in measurement accuracy mentioned previously, it also has several advantages relative to LDV. The most important of these advantages is their high spatial resolution in comparison with conventional LDV systems. In two-dimensional flows a hot wire's spatial resolution is dependent on the wire diameter, which can be as low as 4 μm. In general, conventional LDV systems have focal volumes with dimensions in millimeters. Other advantages of hot-wire anemometry are low noise levels and rapid data acquisition.

Hot-wire/hot-film anemometry was used to measure the inlet boundary layers to the test section because of their high spatial resolution. For the thin inlet boundary-layer cases hot-film sensors, 152 μm in diameter and 2.0 mm long, were used. The sensors were aligned perpendicular to the core flow and were also rotated $\pm$ 45° to determine the lateral velocity within the boundary layers. No lateral velocity could be detected using this method. For the thick inlet boundary layer case a combination of LDV and hot wires were used to exploit the best features of each instrument. Since the boundary layer was large compared to the LDV focal volume, the LDV was used to measure the longitudinal and lateral velocity and the longitudinal turbulence at the outer portion of the boundary layer. Hot-wires were used to measure the longitudinal velocity and turbulence to positions much closer to the wall. Excellent agreement was obtained between these measurements (see section on results). During these last hot-wire measurements the auto-correlation of the signal was obtained at several locations through the boundary layer to ensure that spurious signals had been eliminated.

RESULTS AND DISCUSSION

Flow Condition "A"

Mean Measurements

As shown in figure 13, the endwall shear layer was somewhat thicker at the center of the passage than near the vane surfaces. For example, at the first equi-potential plane of measurements the center portion of the shear layer (position 2) was approximately 15 mm thick at the location where the velocity was equal to 0.95 of the core-flow velocity. Near the suction and pressure surfaces (positions 1 and 3) the shear-layer thicknesses were approximately 9 and 7 mm. These velocity profiles, as well as the fluctuating longitudinal velocities, were measured with both hot-wire anemometry and laser-Doppler velocimetry. At positions 1 and 2 the velocity profiles resembled a two-dimensional accelerating boundary layer, but at position 3 there was some distortion of the flow, with a local maximum and minimum in the fluctuating velocities.

Some insight to the flow at this plane can be obtained from the lateral velocity distribution within the endwall shear layer, shown in the upper portion of figure 14. These measurements of the lateral velocity, V, parallel to the plane of the endwall were obtained with the LDV. Positive lateral velocity indicates flow from the pressure toward the suction surface. These results indicate the possible presence of local vortices near positions 1 and 3 and a strong cross flow, from the pressure toward the suction surface, at position 2. The lateral velocities at positions 1 and 3 were weak in comparison with the secondary flow that developed downstream in the passage. They could, however, have a local influence on the shear layers, convecting low-velocity, highly-turbulent fluid from the near-wall region to locations far from the wall and vice versa.

This distortion of the shear layer at the first measurement plane may have been due to the contraction of the flow that has taken place between the test-section approach duct and the first measurement plane. Such a contraction could have distorted the boundary layer (ref. 25) causing secondary flow.

The individual velocity component measurements for positions 4 through 12 are shown in figures A1 through A9 of Appendix A. From these individual measurements, plots of the longitudinal and lateral velocities were made for each plane of measurements. The longitudinal velocities, shown as contour plots in figure 15, were nondimensionalized using the local core-flow velocity. This was done so that the core-flow velocity variations across the passage, from the pressure to the suction surface, would not dominate the figure.

Hence, only the local velocity defect of the longitudinal component is shown in figure 15. The four planes of measurements, progressing from the top to the bottom of the figure correspond to the measurement planes through the passage, as shown in figure 6. The vertical scale of the individual plots in figure 15 represents the distance from the pressure to the suction surface. The lateral velocities for the same locations were treated in a similar fashion and are shown in figure 16. These lateral velocities were non-dimensionalized by the test-section inlet velocity. Note that the scales are different for each of the four portions of this figure.

In combination, figures 15 and 16 show the inlet boundary layer as it developed into a passage vortex. At equi-potential plane 1, the variation of the boundary layer thickness across the pitch is shown in figure 15, while figure 16 shows a lateral velocity toward the suction surface near the mid-pitch location. Closer to the vane surfaces, the lateral velocity was weaker. At the downstream locations, planes 2, 3 and 4, figure 15 shows a trend of low-velocity fluid accumulating near the suction surface-endwall corner (the upper left-hand corner of the plots). It should also be noted that the over-all extent of the low-velocity region decreased with downstream location. This effect may have been due to the acceleration of the core flow through the passage, which would have had a greater influence on the low-velocity fluid.

In figure 16, the lateral velocities show that the passage vortex gradually developed as the flow was turned through the passage (the flow angles of the core flow are included in Appendix B). At the first equi-potential plane only a weak cross-passage flow existed. In the second plane of figure 16 a passage vortex has started to form. The flow at the near mid-pitch location was generally toward the suction surface, as in plane 1, but farther from the endwall the flow has developed lateral velocities in the sense of a clockwise passage vortex. Near the pressure surface the lateral velocity was toward the endwall; near the pressure surface it was toward mid-span. At planes 3 and 4 the lateral velocity continued to develop into a longitudinal vortex. The measurements at plane 4 show that the passage vortex extended from one vane surface to the other and was centered approximately halfway between the surfaces, 12 to 15 mm from the endwall.

In the suction surface-endwall corner of planes 3 and 4 there appeared to be a complicated flow pattern that may have been due to a counter-rotating vortex. Additional evidence of this is shown in figures A4 and A7 of Appendix A, where the lateral velocity V had an unusual distribution in comparison to the measurements at the other locations. Aside from this corner region, the general lateral flow field was of a relatively simple nature, appearing similar to a concentrated vortex. This was in contrast to the measurements obtained by Langston, Nice and Hooper (ref. 6) of the secondary flow in a rotor cascade. They observed a longitudinal vortex that was considerably smaller than the

passage width. In their passage, the vortex developed on the endwall and was convected toward the suction surface. As it approached the suction surface, it was convected toward the center of the span. This type of vortex motion is somewhat similar to that of a potential vortex near a corner (ref. 51).

The reason for the smaller, localized vortex, observed in ref. 6, is not completely clear. For both experiments the ratio of the inlet boundary-layer thickness to the passage pitch was near 0.12. However, the degree of turning and the acceleration are quite different in the two experiments and these two parameters should have a strong influence on the extent of the longitudinal vortex within the passage. The difference in the size of the vortices in the two experiments may, therefore, be related to differences in the turning angle and the acceleration of the flow. Langston, Nice and Hooper's rotor cascade turned the flow 107°, while accelerating it to 1.6 times the inlet velocity. In this study the flow was turned only 72°, but accelerated to 3.24 times the inlet velocity.

It could be hypothesized that this difference is due to the presence of horseshoe vortices in Langston, Nice and Hooper's experiment and the absences of them in this experiment. However, in a test section similar to this one, except for a lower Reynolds number and the presence of horseshoe vortices, Marchal and Sieverding (ref. 52) observed a concentration of lateral velocities similar to that found in this study. These results, in comparison with Langston, Nice and Hooper's, are shown in figure 17. This figure shows a passage vortex centered halfway between the suction and pressure surface in a turbine inlet-guide vane, but concentrated near the suction surface-endwall region in a turbine rotor blade. These results indicate that the region of the pressure surface, near the endwall, may not be a two-dimensional flow for a turbine inlet-guide vane, with thick endwall boundary layers, even though this may be the case for a turbine rotor blade.

Another observation that can be drawn from figures 15 through 17 is that the secondary flow extends further from the endwall than the region of longitudinal low-velocity fluid.

In addition to the above mentioned measurements, the boundary layers were measured at the intersections of the first equi-potential plane and the mid-span vane surfaces. These locations are shown as positions 13 and 14 in figure 6. The measurements of figure 18 show that this region of the inlet flow was free from abnormal effects. Additional measurements were also made of the endwall boundary layer at the first equi-potential plane. These measurements were intended to provide a refined initial condition for computational procedures and were therefore more closely spaced near the vane surfaces where the flow was more complicated. These results are included in Appendix B.

Turbulence Measurements

Measurements of the turbulence within the passage vortex was one of the principal problems this experiment was intended to address. No information exists concerning the turbulent stresses within a passage vortex. Since the turbulent stresses at a particular location are dependent on the upstream flow history, as well as local diffusion, production and dissipation, it is difficult to estimate the qualitative nature of the turbulence in the vane-passage exit plane, let alone infer the quantitative distribution of the turbulent stresses. A turbulence model that includes these effects will have empirical constants as a result of the scaling law arguments used to simplify the turbulence model. The only practical method by which these simplifications can be tested and the empirical constants evaluated is through comparisons with experimental results.

To address the above problem, for the flow in a turbine inlet-guide vane passage, the turbulent stresses were measured at the same locations as the mean velocities (see figure 6). At the first measurement plane of figure 6 only the longitudinal normal stress was measured. These results were shown in figure 13, with the data for the mean measurements. The data indicated there was no abnormal behavior for accelerating boundary layers. The inflection of the turbulent stress distribution near the pressure surface (position 3) was attributed to localized vorticity generated by contracting the flow at the entrance of the test section. At the downstream measurement locations (positions 4 through 12) all six turbulent stresses were measured for this flow condition. The results are shown in figures 19 through 36 as normalized stresses, based on the local core-flow velocity, versus distance from the endwall.

At the second equi-potential plane (positions 4, 5 and 6) the turbulent structure of the outer portion of the boundary layer was still similar to that of a two-dimensional boundary layer. This can be seen by comparing these results to Klebanoff's data (ref. 53) for a flat-plate, zero-pressure gradient boundary layer. At positions 4 and 5 the mean velocities (figures A1 and A2 of Appendix A) and turbulent stresses (figures 19 through 22) were measured to within 5 mm from the endwall. The following table compared these measurements (the notation of Klebanoff has been converted to the notation of this study).

	Klebanoff	Position 4	Position 5
Z/δ	0.62	0.16	0.16
U/U_∞	0.92	0.92	0.92
$\sqrt{\overline{u'^2}}/U_\infty$	0.05	0.035	0.040
$\sqrt{\overline{v'^2}}/U_\infty$	0.04	0.030	0.032
$\sqrt{\overline{w'^2}}/U_\infty$	0.03	0.022	0.022
$-\overline{u'w'}/U_\infty^2$	6×10^{-4}	4×10^{-4}	4×10^{-4}

Except for the non-dimensional distance from the wall, the differences between these measurements are well within the uncertainties associated with turbulence measurements.

A similar comparison can be made of the near-wall data at position 6. The mean velocity of figure A3 (Appendix A) and the turbulent stresses of figures 23 and 24 are shown below.

	Klebanoff	Position 6
Z/δ	0.87	0.25
U/U_∞	0.97	0.97
$\sqrt{\overline{u'^2}}/U_\infty$	0.026	0.025
$\sqrt{\overline{v'^2}}/U_\infty$	0.020	0.020
$\sqrt{\overline{w'^2}}/U_\infty$	0.022	0.037
$-\overline{u'w'}/U_\infty^2$	3×10^{-4}	2×10^{-4}

The variation of the non-dimensional distance from the wall is believed due to the acceleration of the flow. In the present study, this would have the effect of energizing the inner portion of the shear layer and causing a particular velocity ratio to occur closer to the wall for an accelerated shear layer than for a zero-pressure gradient boundary layer.

It should be noted that $-\overline{u'v'}/U_\infty^2$ was essentially zero at the above three locations (see figures 19, 21 and 23) as would be expected for a two-dimensional boundary layer. Because the measurement of $\overline{v'w'}/U_\infty^2$ had a high degree of uncertainty it was not analyzed here. This uncertainty was due to the measurement technique required for $\overline{v'w'}/U_\infty^2$ as discussed below.

To measure $\overline{v'w'}/U_\infty^2$ the laser beams were transmitted through the pressure surface at 45° inclination to the endwall surface. This permitted the measurement of $\overline{v'^2} + \overline{v'w'} + \overline{w'^2}$, from which $\overline{v'w'}/U_\infty^2$ was obtained after subtraction of $\overline{v'^2}$ and $\overline{w'^2}$. The measurement of $\overline{v'^2}$ was based on three other measurements and $\overline{w'^2}$ on five other measurements, so that the uncertainty for $\overline{v'w'}/U_\infty^2$ was considerably higher than that for the other turbulent stress measurements. This uncertainty was estimated to be about 2×10^{-3} for $\overline{v'w'}/U_\infty^2$. An example of this uncertainty is shown in figure 20 (position 5), where $\overline{v'w'}/U_\infty^2$ was equal to 2×10^{-3} in the core flow.

At equi-potential plane 3, figures 25 through 30 show that the similarity of the turbulence with two-dimensional boundary layers has ceased. The shearing stress $-\overline{u'w'}/U_\infty^2$ was no longer related to the normal stresses as for a flat-plate boundary layer. In particular, figure 25 shows that, near the suction surface (position 7), the shearing stress $-\overline{u'v'}/U_\infty^2$ had developed a characteristic oscillation that may have been related to the mean velocity distribution of the lateral component V at the same location. This mean velocity distribution is shown in the center portion of figure A4 of Appendix A. It is hypothesized that these results were due to the presence of a counter-rotating vortex near the suction surface-endwall region. Such a vortex could have produced the high velocity gradients of figure A4, which could have produced a high turbulent shearing stress.

Near the pressure surface (position 9) figures 29 and 30 show a decrease in the near-wall turbulence when compared with the suction surface location (figures 25 and 26). This could have been expected from the mean velocity results of figure 15. At equi-potential plane 3, this figure shows that the low-velocity fluid had accumulated near the suction surface, resulting in a thinner shear layer near the pressure surface.

Figures 31 through 36 show that the trends noted in plane 3 continued at plane 4 (positions 10, 11 and 12). The turbulent stresses were significantly higher near the suction surface than at the pressure surface. For example, compare the results near the suction surface (figures 31 and 32) with the results near the pressure surface (figures 35 and 36). Again, this increased level of turbulence near the suction surface could have been anticipated based on the mean velocities of figure 15.

Near the suction surface (position 10) figure 31 shows the presence of a distinctive oscillation of the shearing stress $-\overline{u'v'}$ near the endwall. As noted for position 7, this distribution of the shearing stress seemed to be related to the lateral mean velocity V, as shown in the center portion of figure A7.

It should be noted that the maximum, non-dimensionalized normal stress measured in plane 4 was about 0.04. This value was measured near the suction surface (position 10) and is shown in figure 31.

In summary, although the passage vortex was generated by highly-turbulent, low-velocity fluid from the endwall region, this experiment has shown that this high turbulence did not exist in the passage vortex. In fact, large regions of the passage vortex were shown to be non-turbulent flow.

Flow Condition "C"

Mean Measurements

The test arrangement for flow condition "C" consisted of a thin inlet boundary layer and the high aspect ratio test section. Figure 37 shows that the boundary layers were 2 to 2.5 mm thick, based on the location at which $U/U_\infty = 0.95$, at the first measurement plane (positions 1, 2 and 3). This is considerably thinner than the 10 to 15 mm thick boundary layers measured for flow condition "A" (figure 13). The above measurements were obtained with hot-film sensors, but at position 2 the boundary layer was also measured with a hot-wire sensor, to obtain higher spatial resolution. This measurement, shown in figure 38, included the mean and fluctuating longitudinal velocity. The comparison of the results with Klebanoff's data (ref. 53), also plotted in the figure, shows the expected effect of acceleration on a boundary layer, that is, an increase in the near-wall mean velocity and a decrease in the near-wall turbulence intensity.

Measurements at equi-potential planes 2, 3 and 4 were treated the same as those for flow condition "A", except that only one lateral component, V, of the mean velocity was measured. The individual measurements are included in Appendix A, figs. A10 through A18, while the reduced lateral and longitudinal velocities are shown for each plane in figures 39 and 40.

Figure 39 shows a rapid thickening of the boundary layer between the first and second planes. Figure 40 shows a lateral velocity toward the suction surface at the second plane, except near the suction surface where the lateral velocities indicate the possible presence of a weak counter-rotating vortex. This is similar to the results for flow condition "A", shown in figure 16. Note that the scales are different in figures 16 and 40 for both the velocity vector and distance from the endwall.

At the third equi-potential plane, figure 40 shows a passage vortex in the suction surface-endwall region. There was also an accumulation of low-momentum fluid at this location, as shown in figure 39. At mid-passage and

near the pressure surface locations there was a general cross-channel flow toward the suction surface (figure 40), and a thinning of the low-velocity region (figure 39). At the passage throat, equi-potential plane 4, the low-momentum fluid was concentrated near the suction surface (figure 39), extending approximately 12 mm from the endwall. Near the pressure surface there is only slight evidence of low-momentum fluid. This effect was more noticable in figures A16, A17 and A18 than in figure 39.

As also noted for flow condition A, figures 39 and 40 show that at the exit plane (plane 4) significant lateral velocities existed in regions with no velocity defect.

Due to the difference in the boundary-layer thicknesses at the first equi-potential plane for flow conditions "A" (fig. 13) and "C" (fig. 37) a significant difference in the exit flow was observed (compare figures 15 and 39 and figures 16 and 40). For flow condition "C" the passage vortex was located in the suction surface-endwall region, having little influence near the pressure surface. This is in contrast to flow condition "A" in which the passage vortex appeared to be centered halfway between the pressure and suction surfaces and farther from the endwall.

Since the inlet shear layer for flow condition "C" was produced with a 0.51-mm trip wire located 50 mm upstream of the vane leading edges, one can infer that most of the low-velocity fluid in the passage exit was generated within the test section, rather than being convected through the passage. This would also suggest that an inlet-guide-vane passage with no inlet shear flow would still have a significant amount of secondary flow at the exit of the passage.

Turbulence Measurements

The turbulence data (figures 41 through 51) provide little insight into understanding this flow since the spatial resolution was poor in this case, in comparison with flow condition "A". The most interesting regions of the flow were within 5 mm of the endwall, which was beyond the limits of the LDV. At the second measurement plane (figures 41-43) and near the suction surface at the third and fourth planes (figures 44, 45, 48 and 49) the non-dimensionalized turbulent normal stresses were found to be generally between 0.02 and 0.03 near the endwall with a decrease to core-flow values within 10 or 15 mm of the endwall. Near the pressure surface and at mid-span in planes 3 and 4 (figures 46, 47, 50 and 51) there was little evidence of turbulent flow to within 5 mm of the endwall. This was especially so at positions 11 and 12, as shown in figures 50 and 51. This is in agreement with the mean measurements (fig. 39) which show an accumulation of the low-momentum fluid near the suction surface.

Flow Conditions "B"

Condition "B" was nearly identical to condition "C" except that the span to axial chord ratio was decreased from 1.866 to 0.617, a factor of approximately three. The isolated effect of blade aspect ratio variation can be observed by comparing the results of flow conditions "B" and "C". The inlet boundary layers were essentially identical for the two cases, as can be seen by comparing figure 52 with figure 37. These figures show the mean-velocity profiles of the endwall boundary layers at the first equipotential plane. The locations at which $U/U_\infty = 0.95$ varies from 2.0 to 2.5 mm from the endwall for all cases except position 1, condition "B", where it occurs at 1.0 mm from the endwall. This slight difference in the boundary-layer thickness is not understood, but is not believed to have an important effect on the downstream passage flow. For these thin inlet boundary-layer cases, most of the passage vorticity is believed to be generated within the passage. This results since the boundary layers entering the passage were quite thin, having been initiated by trip wires only 0.51 mm in diameter, 50 mm upstream of the test-section leading edge. Therefore, for thin boundary layers, the passage flow should be independent of small variations in the inlet boundary layers and comparison of the above conditions should show the isolated effect of variable span on the passage secondary flow.

A direct comparison of the three mean-velocity components is possible for downstream, near-suction surface location, positions 7 and 10, as shown in figures 53 and 54. In both of these figures the results for condition "B" are shown on the left side and condition "C" on the right side. At both locations the figures show a stronger secondary flow, lateral component V, and an altered longitudinal flow for condition "B". In fact, the lateral velocity in the plane of the endwall was nearly twice the value for conditions "B" as compared to condition "C". Also, the passage vortex appeared to be closer to the endwall for condition "B", as inferred from the location where V equaled zero. The velocities normal to the endwall, W, were insignificantly small in comparison to the other lateral component, and almost identical for the two cases. The longitudinal component had less of a velocity defect for condition "B", but this may have been a result of the passage vortex being centered at a different location for the two cases.

The turbulent stresses measured at positions 7 and 10 were essentially identical for the two cases, as can be seen by comparing figures 55 through 58 with figures 44, 45, 48 and 49.

Two possible mechanisms exist for altering the secondary flow through a change in the passage aspect ratio. The first is blockage due to the low-velocity shear layer next to the endwall. However, using the more complete measurements for flow condition "C", the blockage effect was estimated and found to

be insignificant for the two aspect ratios considered in this study. This estimate was based on the assumption that the displacement thicknesses of the endwall shear layers were 2.5 mm at plane 1 and 5 mm at plane 4. From the results shown in figure 39 these would be conservative estimates. Since the test-section spans for the two cases were 168 and 508 mm, the acceleration of the core flow, due to viscous blockage, would be approximately 1 and 3 percent. The other possible mechanism, through which a change in the span could alter the secondary flow, is induced vortex motion. Although it is impossible to obtain quantitative estimates of this effect from the data obtained, by modeling the flow as concentrated vortices and mirror images, it can be seen that a change in the value of the induced velocities could result from changes in aspect ratio. Although these velocities may be small, only a small change in the location of the passage vortex would be necessary to cause a significant change in the observed results, especially when the measurements are obtained near the center of the passage vortex.

In summary, the quantitative features of the two flows were similar with variations in the mean velocity. These variations could be the result of a slight relocation of the passage vortex, which would preserve the global features of the flow, but change the measurements obtained at selected locations near the suction surface.

CONCLUSIONS

1. Using laser-Doppler velocimetry techniques, a longitudinal vortex was investigated in a turbine inlet-guide-vane passage for one variation in inlet endwall boundary-layer thickness and one variation in the blade aspect ratio. For all three cases the horsehoe vortex was suppressed in this experiment.

2. Maximum turbulence intensities within the longitudinal vortex were found to be on the order of 2 to 4 percent. Large regions of the vortex were non-turbulent. Since a turbulent wall boundary layer was the source of vorticity that produced the passage vortex, these low turbulence levels were not anticipated.

3. The lateral velocity fields, generated by the passage vortex, extended significantly beyond the region of the longitudinal velocity defect. This is in contrast to previous measurements obtained in a rotor cascade.

4. The primary effects of reducing the inlet endwall boundary-layer thickness, by a factor of approximately five, were to reduce the maximum lateral velocities, by a factor of approximately two, and to change the spatial extent of the vortex. The apparent vortex was located closer to the endwall, by a factor of approximately two.

5. The effect of changing blade aspect ratio by a factor of three was small. Measured turbulent stresses were essentially identical for the two cases. Observed changes in the mean velocity, at selected locations near the suction surface, may have been caused by a difference in the location of the passage vortex for the two cases.

TABLE 1

TEST–SECTION GEOMETRY

Axial chord	=	272.29-mm
Pitch	=	209.55-mm
Throat width	=	61.51-mm
Leading-edge radius	=	19.05-mm
Trailing-edge radius	=	5.56-mm

AIRFOIL COORDINATES

Axial Distance (mm)	Pressure Surface (mm)	Suction Surface (mm)
0.00	0.00	0.00
1.27	6.84	-6.84
2.54	9.50	-9.50
5.08	12.95	-12.95
7.62	15.24	-15.24
10.16	16.85	-16.84
12.70	17.96	-17.96
25.4	21.08	-20.57
38.1	24.38	-21.84
50.8	28.16	-22.75
63.5	32.51	-22.86
76.2	37.34	-22.35
88.9	42.67	-20.32
101.6	49.02	-17.02
114.3	56.64	-12.70
127.0	65.53	-7.11
139.7	75.69	0.00
152.4	88.39	9.40
165.1	102.36	21.84
177.8	111.62	37.34
190.5	136.65	55.88
203.2	156.46	77.72
215.9	177.55	104.39
228.6	199.90	135.89
241.3	223.52	170.18
254.0	248.41	207.01
271.8	263.14	263.14

TABLE 2
MEASUREMENT LOCATIONS

Location	x/C_x	z/s	x(mm)	z(mm)
1	0.106	-0.216	28.96	-45.21
2	0.122	-0.441	33.27	-92.46
3	0.177	-0.676	48.26	-141.73
4	0.367	-0.171	99.82	-35.81
5	0.414	-0.321	112.78	-67.31
6	0.490	-0.474	133.35	-99.34
7	0.605	0.013	164.85	2.79
8	0.663	-0.059	180.59	-12.45
9	0.735	-0.130	200.15	-27.18
10	0.757	0.272	205.99	56.90
11	0.817	0.233	222.50	48.77
12	0.882	0.187	240.28	39.12

x - axial distance from leading edge
z - tangential distance from leading edge
C_x - axial chord
s - pitch

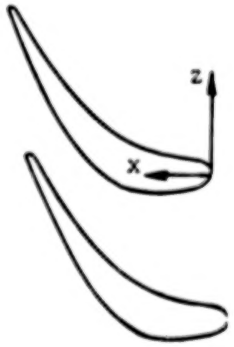

TABLE 3

MEASUREMENTS OBTAINED

	FLOW CONDITIONS								
	A			B			C		
ϕ \ ψ	20%	50%	80%	20%	50%	80%	20%	50%	80%
1	III	III	III	V	V	V	V	IV	V
2	I	I	I				II	II	II
3	I	I	I	I			I	II	II
4	I	I	I	I			I	II	II

ϕ = EQUI-POTENTIAL PLANES, FROM UPSTREAM TO DOWNSTREAM (SEE FIG. 6)

ψ = STREAMLINE PLANES FOR PERCENT MASS FLOW RATE, MEASURED FROM SUCTION TO PRESSURE SURFACE

SYMBOL	QUANTITIES MEASURED, INSTRUMENT USED
I	U,V,W, $\overline{u}'^2$, $\overline{v}'^2$, $\overline{w}'^2$, $\overline{u'v'}$, $\overline{u'w'}$ AND $\overline{v'w'}$ – LDV
II	U,V, $\overline{u}'^2$, $\overline{v}'^2$ AND $\overline{u'v'}$ – LDV
III	U,V, AND $\overline{u}'^2$ – LDV, U AND $\overline{u}'^2$ – HW
IV	U AND $\overline{u}'^2$ – HW (V COULD NOT BE DETECTED)
V	U – HF (V COULD NOT BE DETECTED)

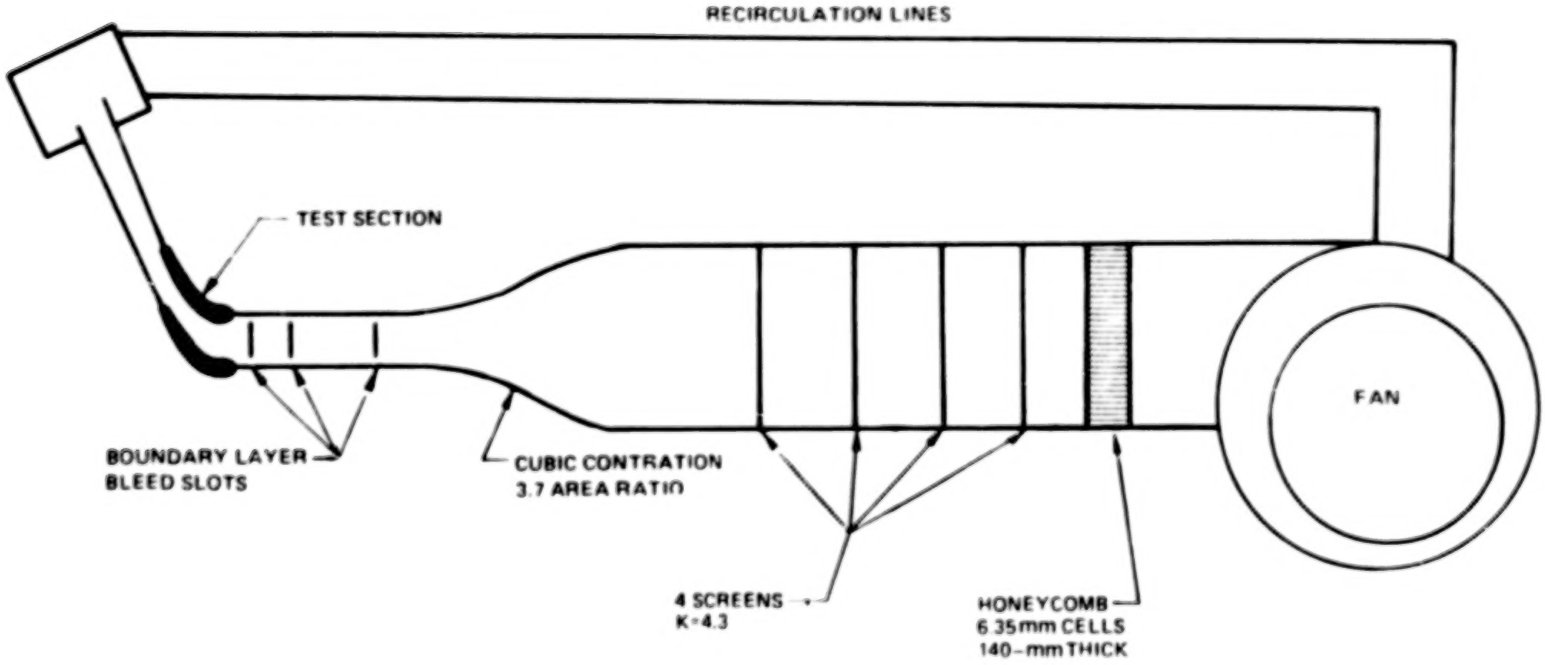

FIGURE 1 – UTRC LOW – SPEED WIND TUNNEL

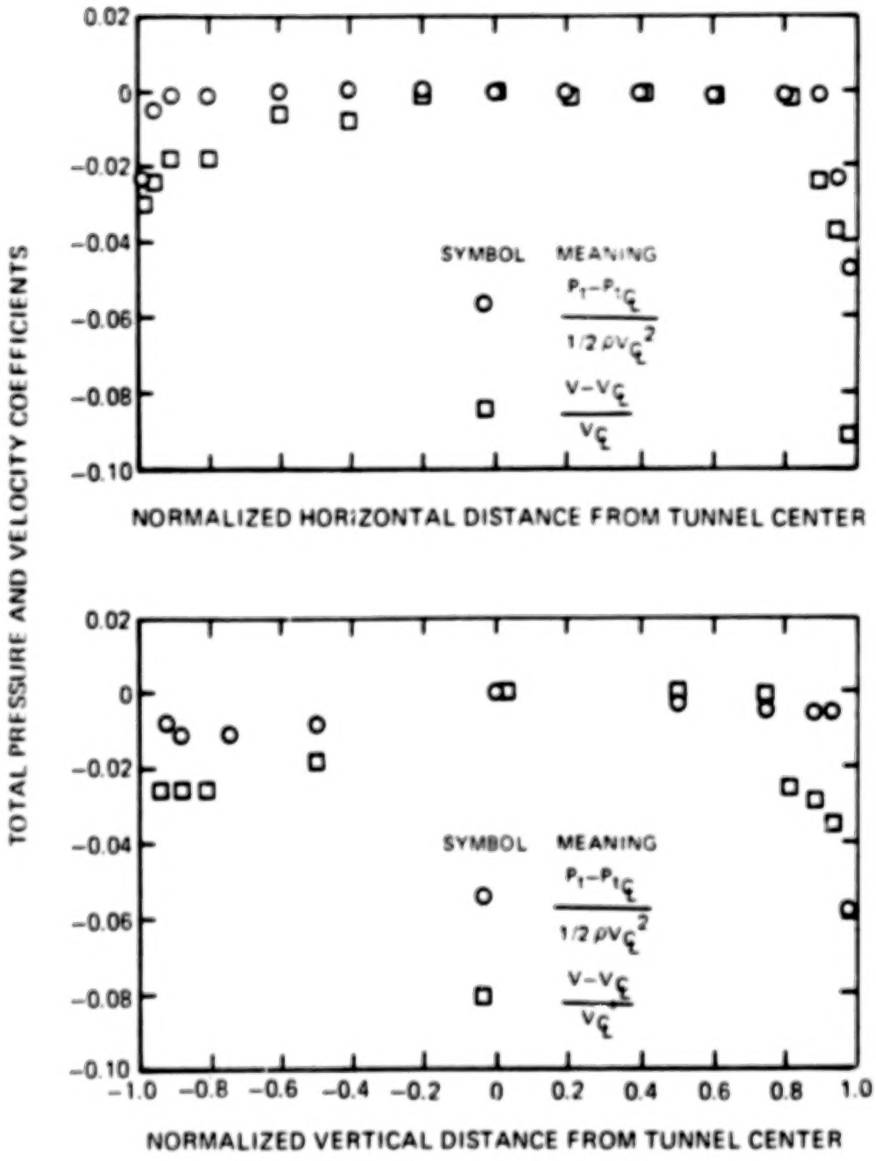

FIGURE 2 – TOTAL PRESSURE AND VELOCITY DISTRIBUTION OF THE INLET FLOW 150mm UPSTREAM OF THE TEST SECTION

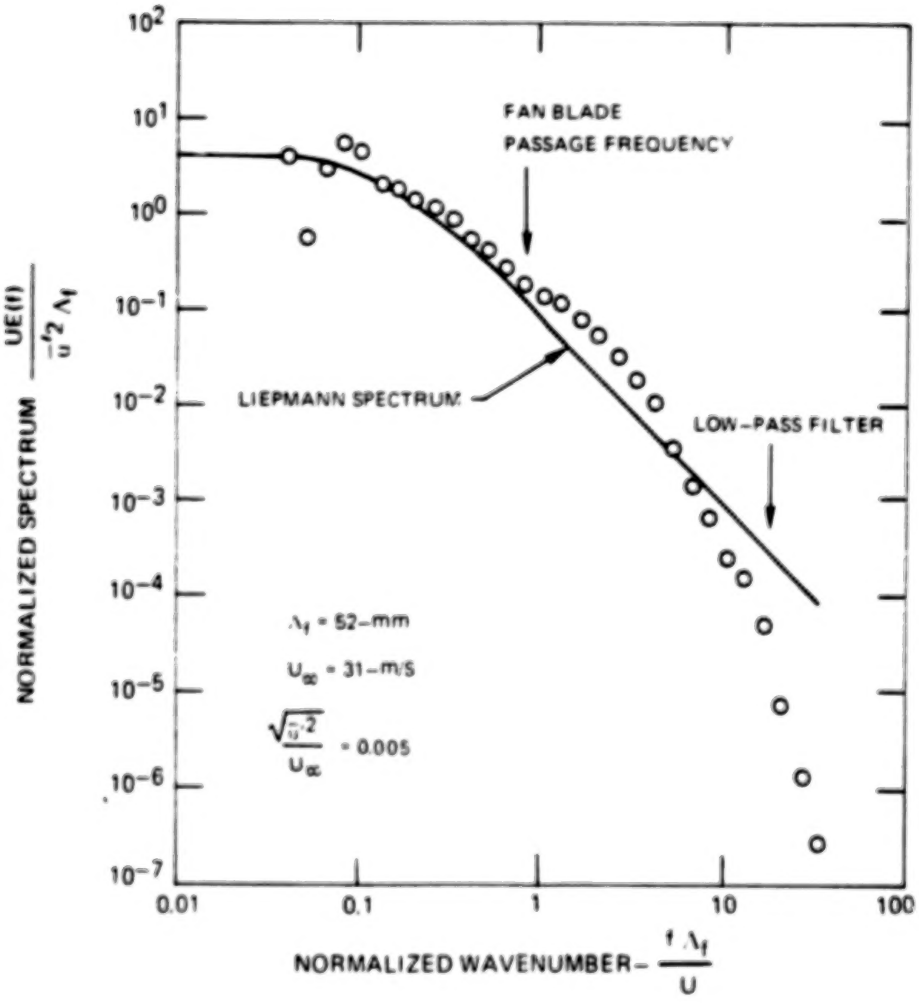

FIGURE 3 – ONE-DIMENSIONAL SPECTRUM OF LONGITUDINAL TURBULENCE OF THE INLET FLOW

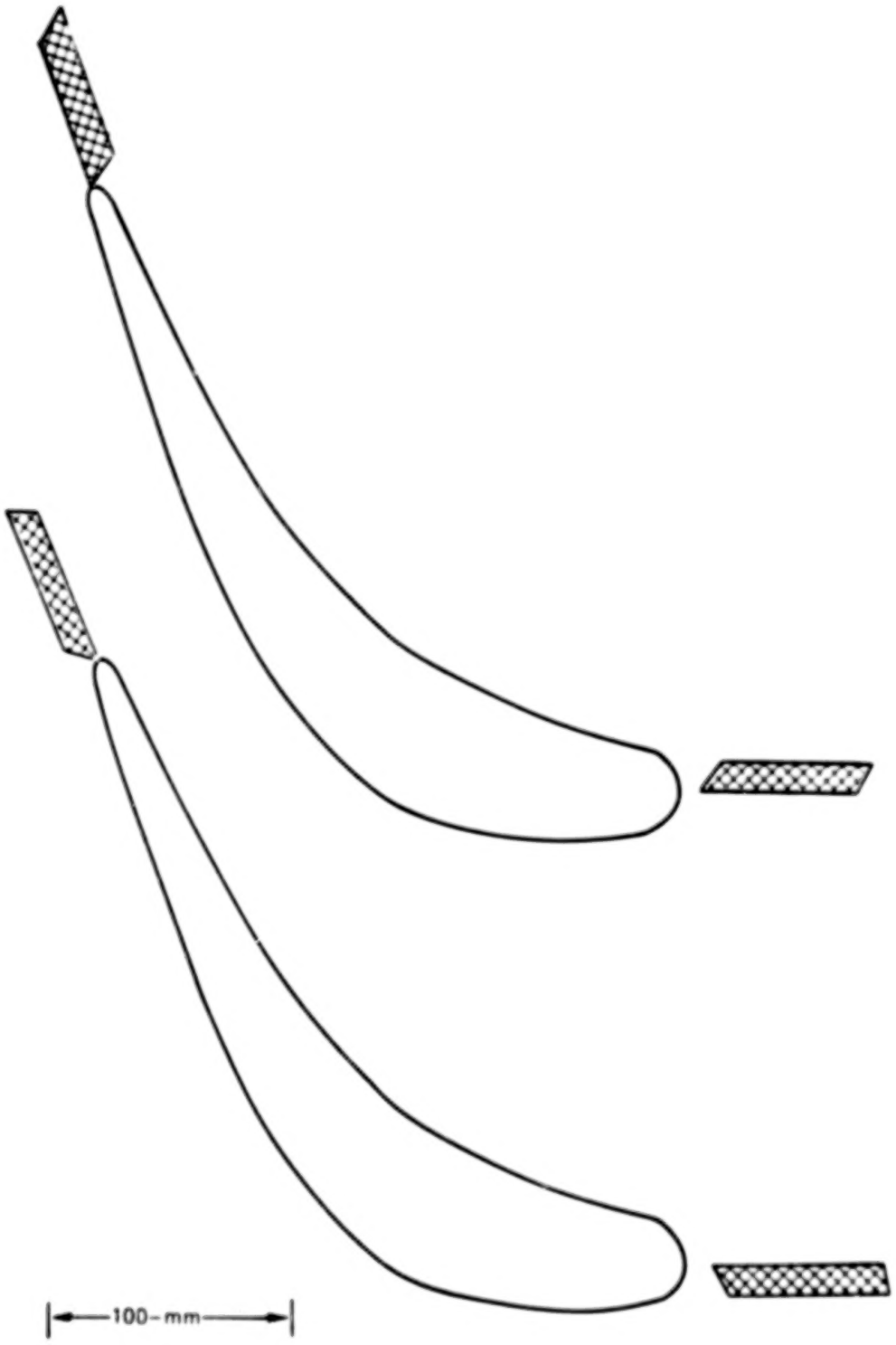

FIGURE 4 – TEST – SECTION GEOMETRY

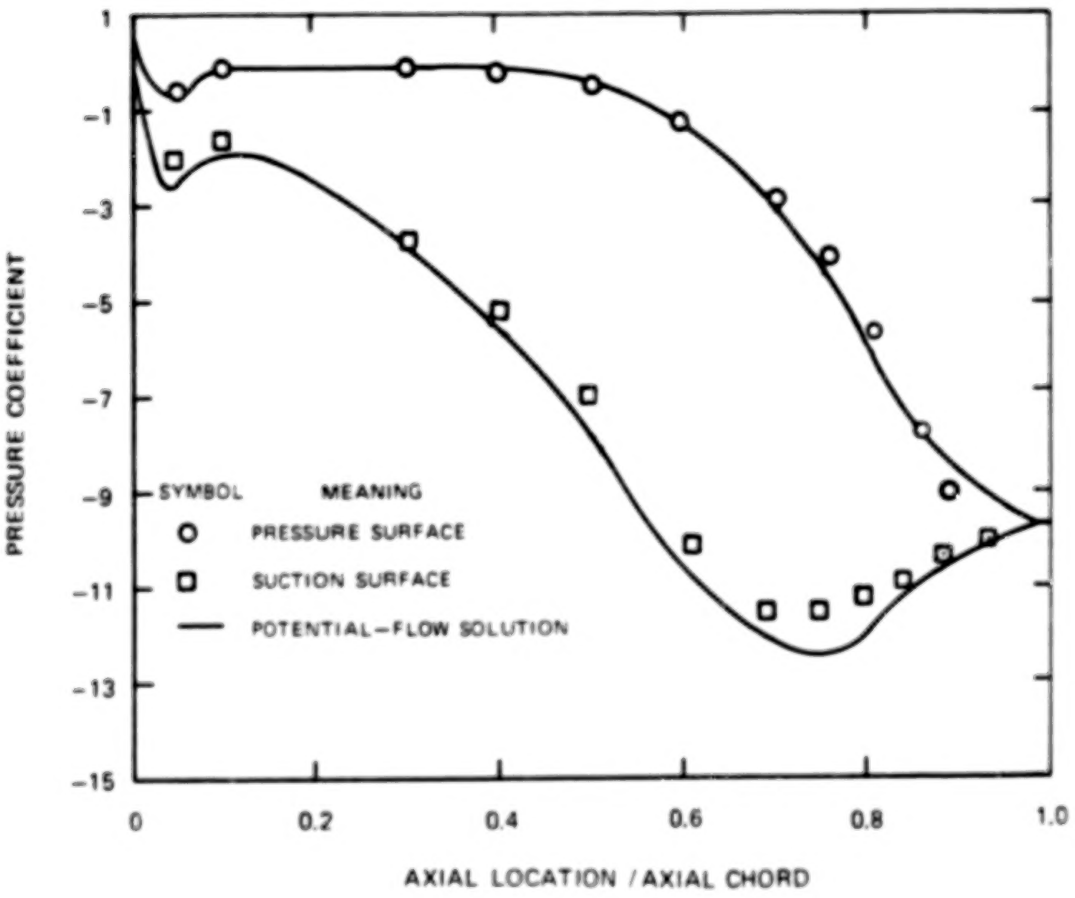

FIGURE 5 — COMPARISON OF TEST-SECTION PRESSURE COEFFICIENT vs POTENTIAL-FLOW SOLUTION FOR AN EQUIVALENT CASCADE

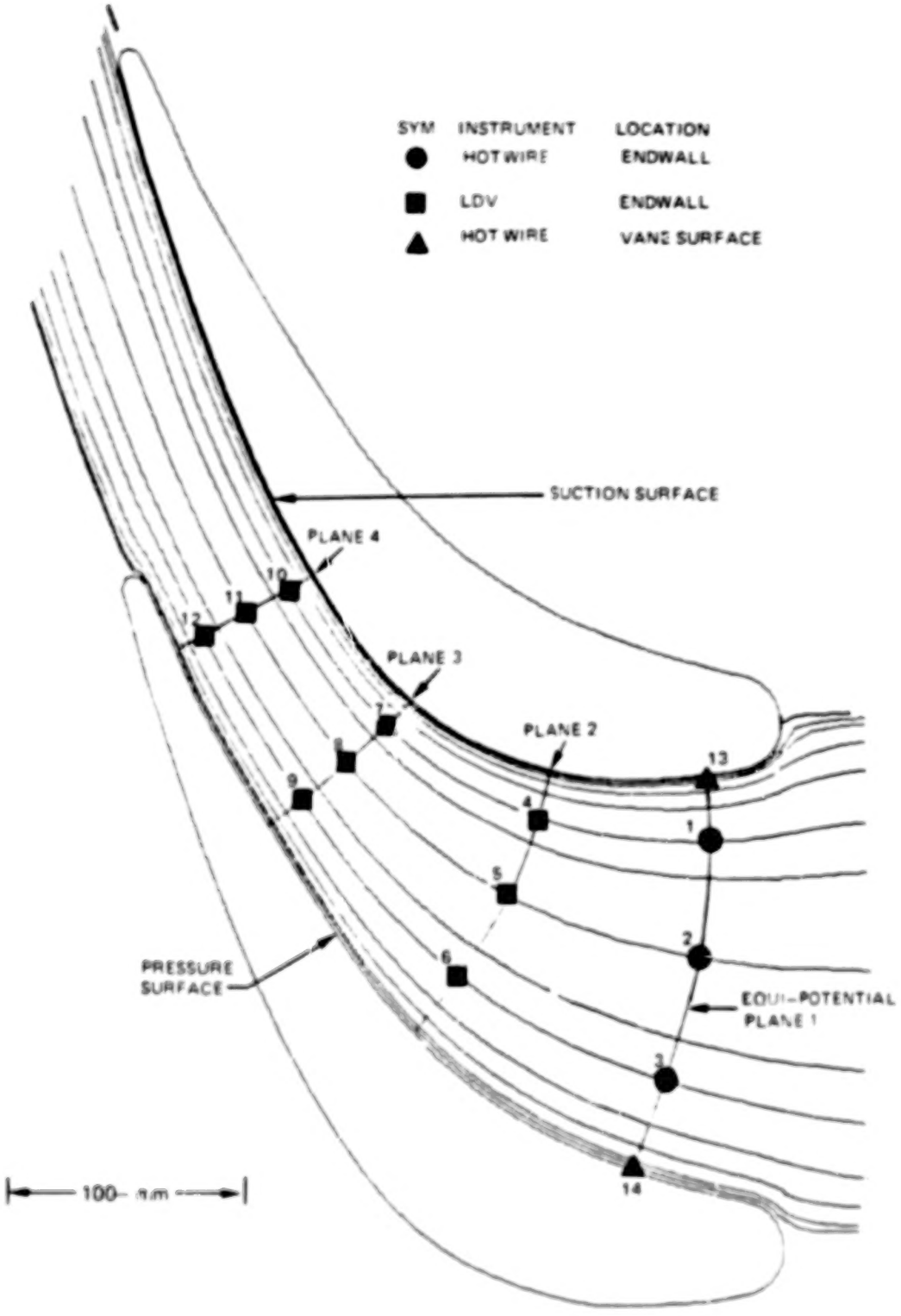

FIGURE 6 – TEST – SECTION MEASUREMENT LOCATIONS

BLANK PAGE

BLANK PAGE

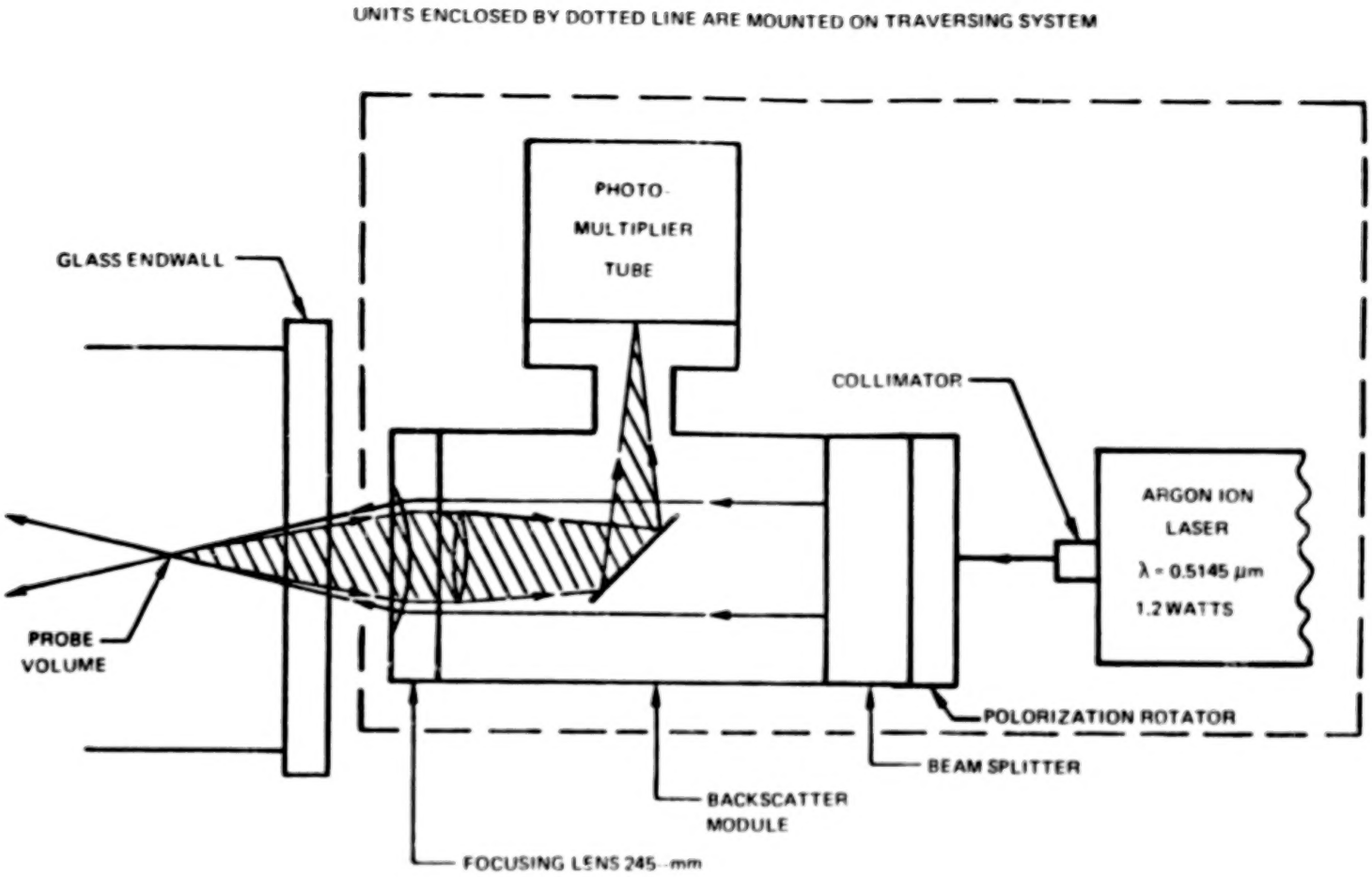

FIGURE 7–OPTICAL ARRANGEMENT FOR MEASUREMENTS IN THE XY PLANE

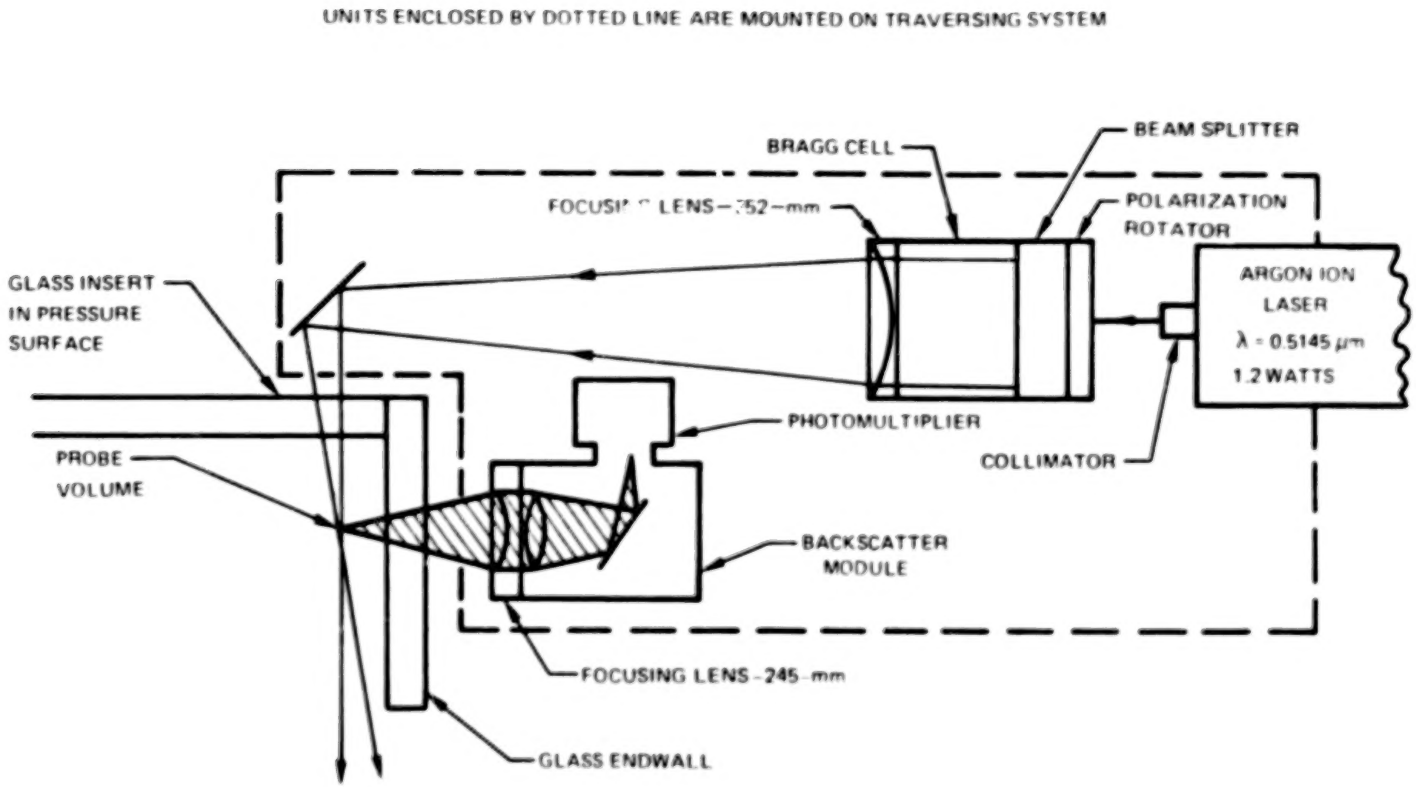

FIGURE 8 – OPTICAL ARRANGEMENT FOR MEASUREMENT IN THE XZ AND YZ PLANES

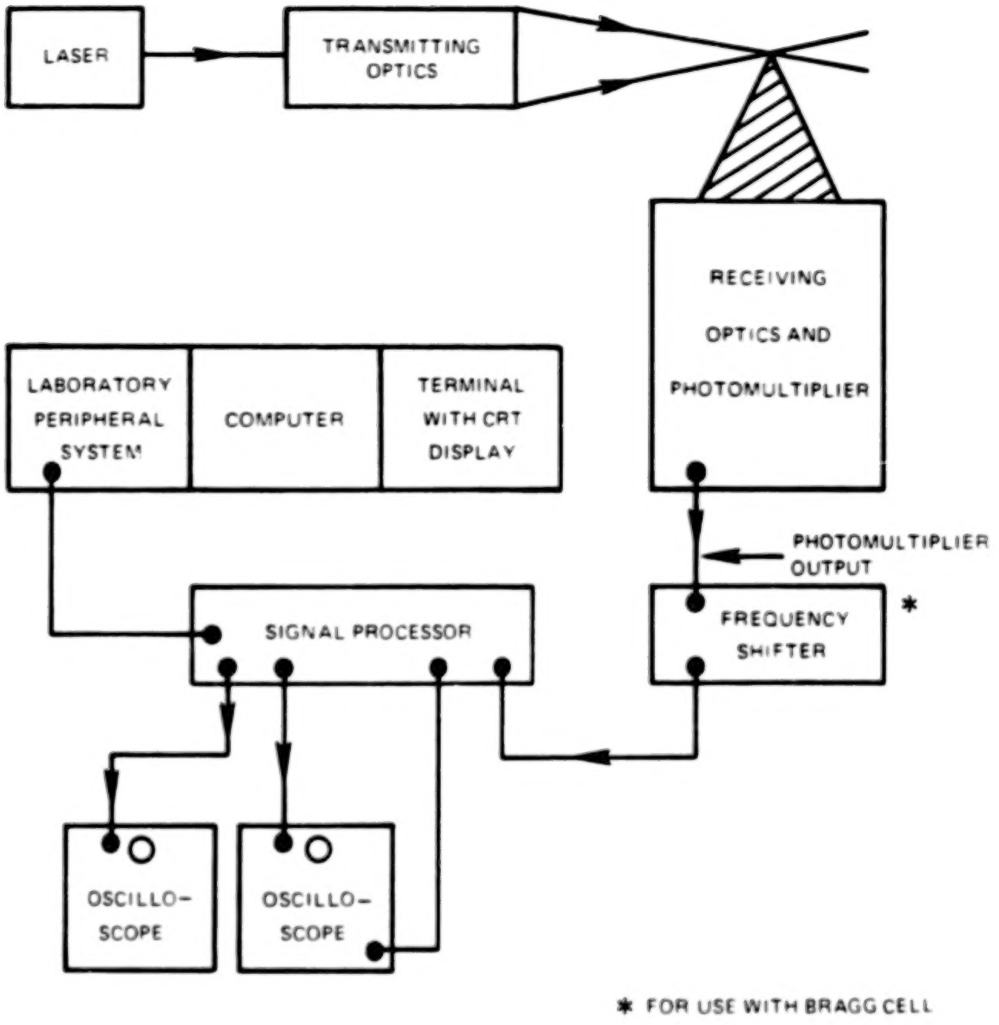

FIGURE 9 –SCHEMATIC OF LASER–DOPPLER VELOCIMETER SYSTEM

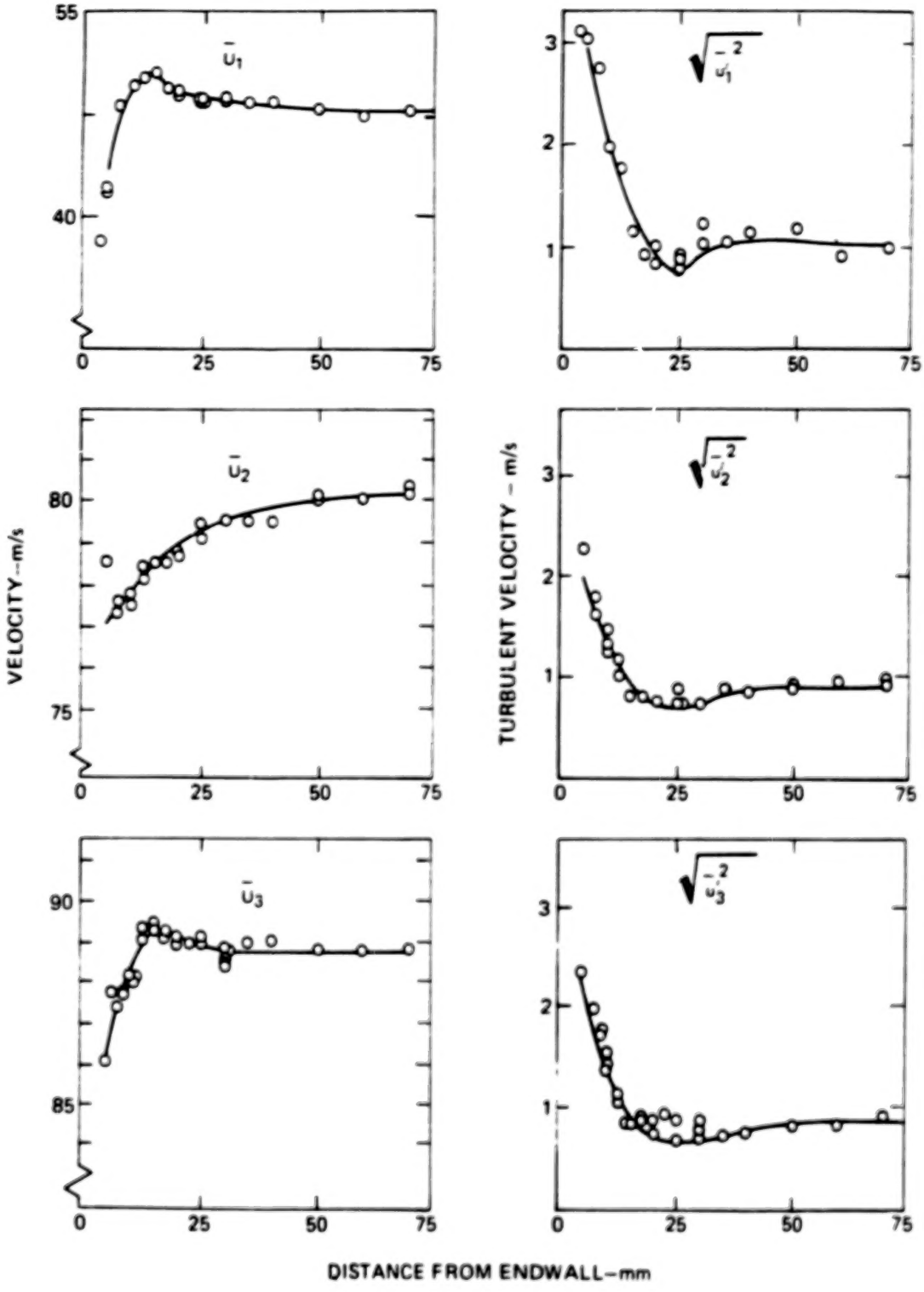

FIGURE 10– VELOCITIES VS DISTANCE FROM THE ENDWALL – TEST CASE

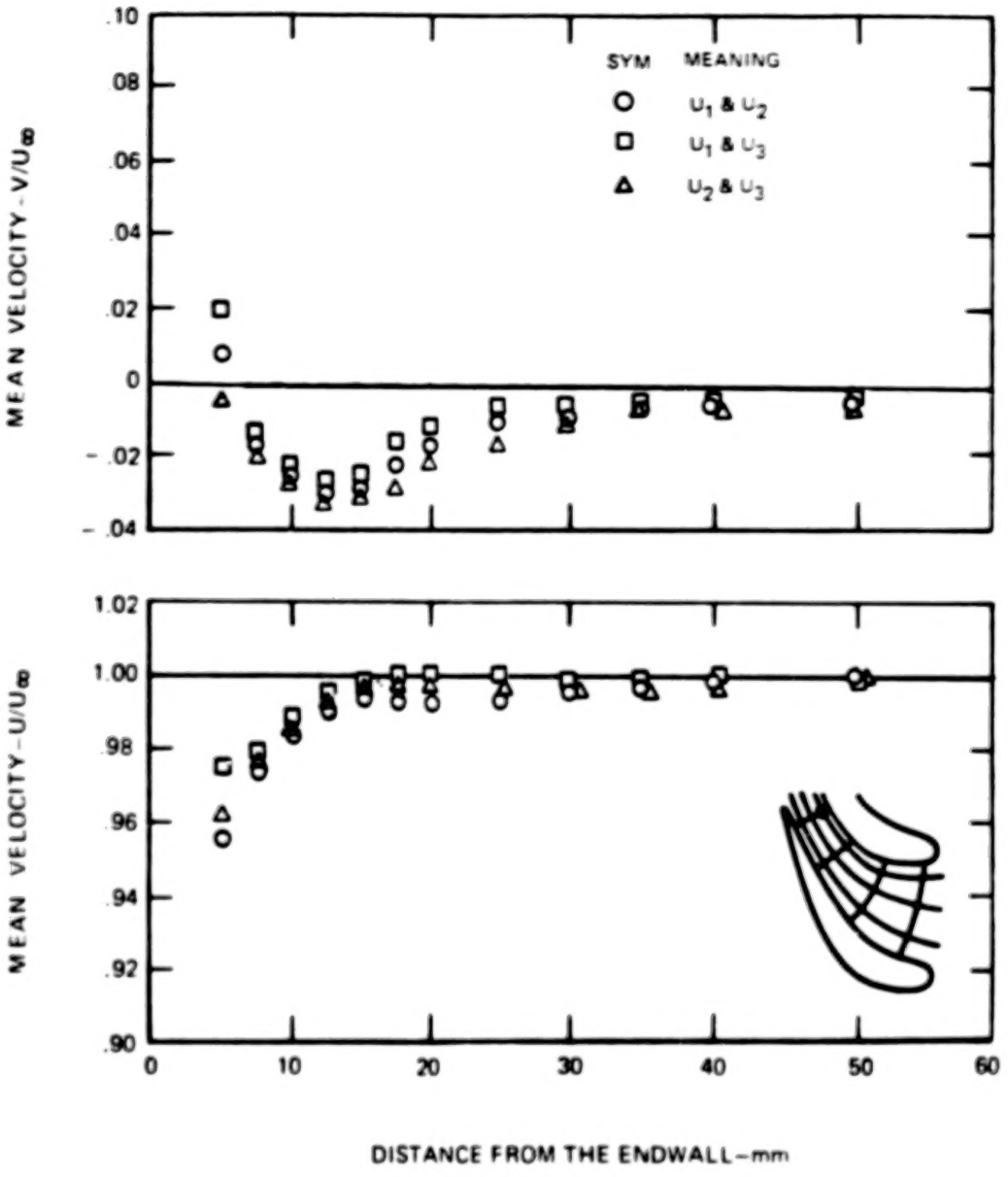

FIGURE 11 – MEAN VELOCITIES VS. DISTANCE FROM THE ENDWALL POSITION 10, FLOW CONDITION C, TEST CASE

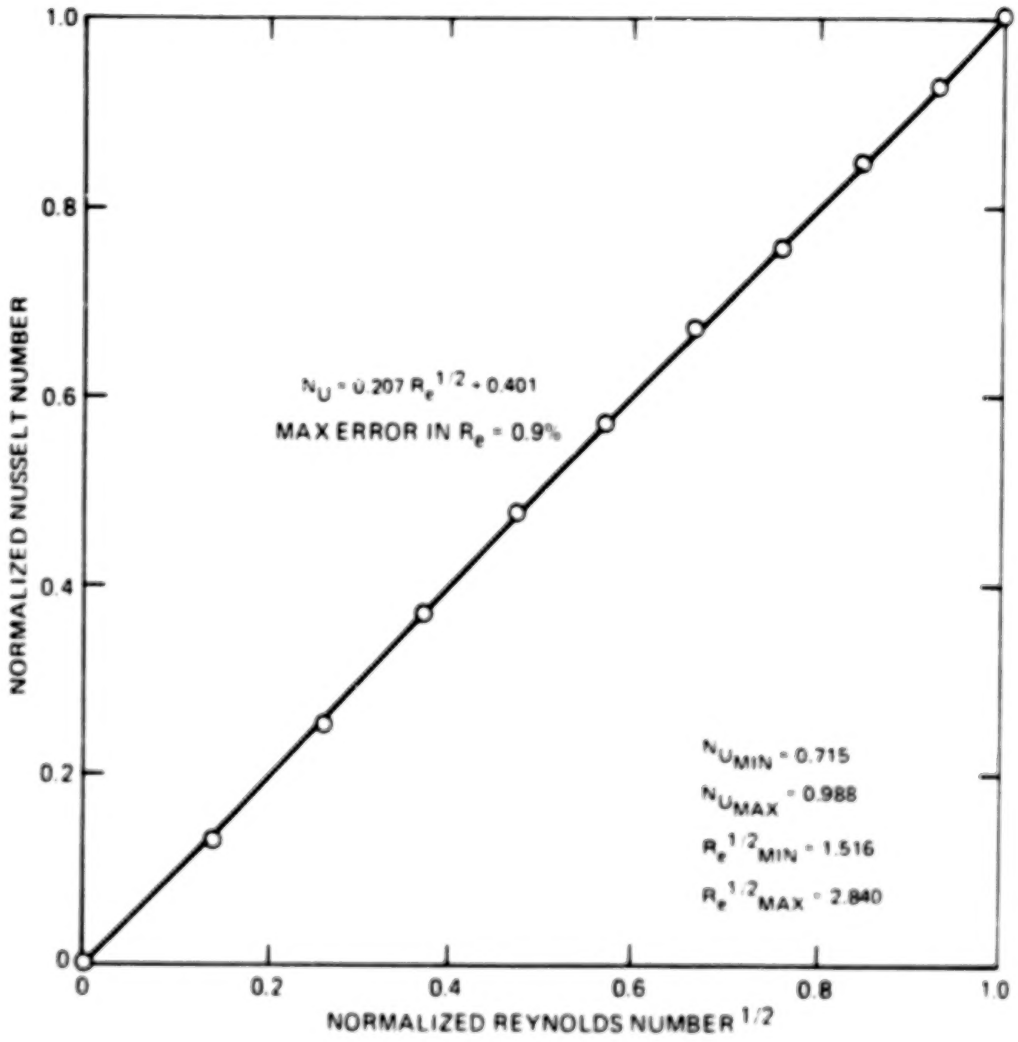

FIGURE 12– TYPICAL HOT WIRE CALIBRATION

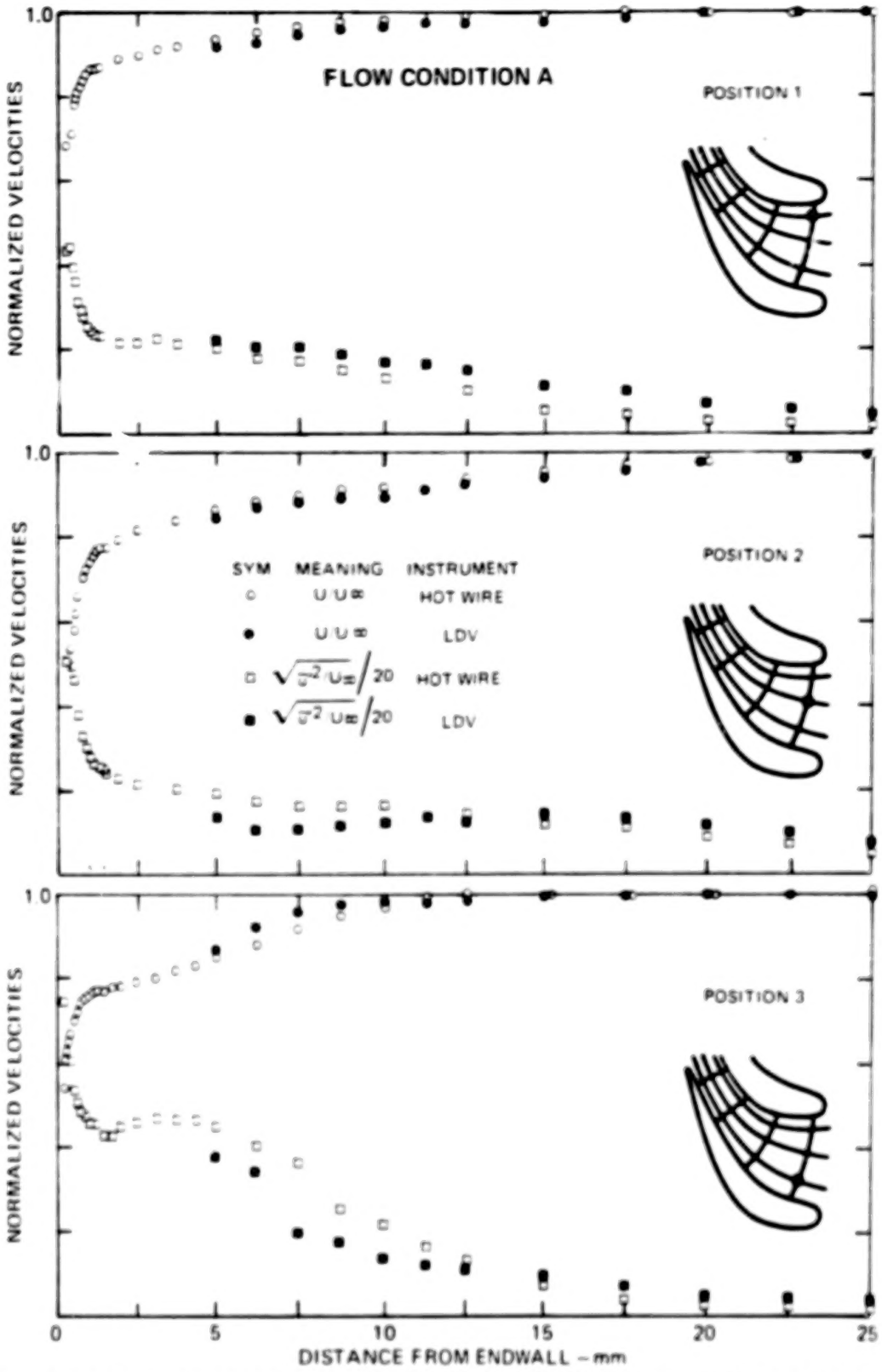

FIGURE 13– NORMALIZED VELOCITIES VS DISTANCE FROM THE END WALL

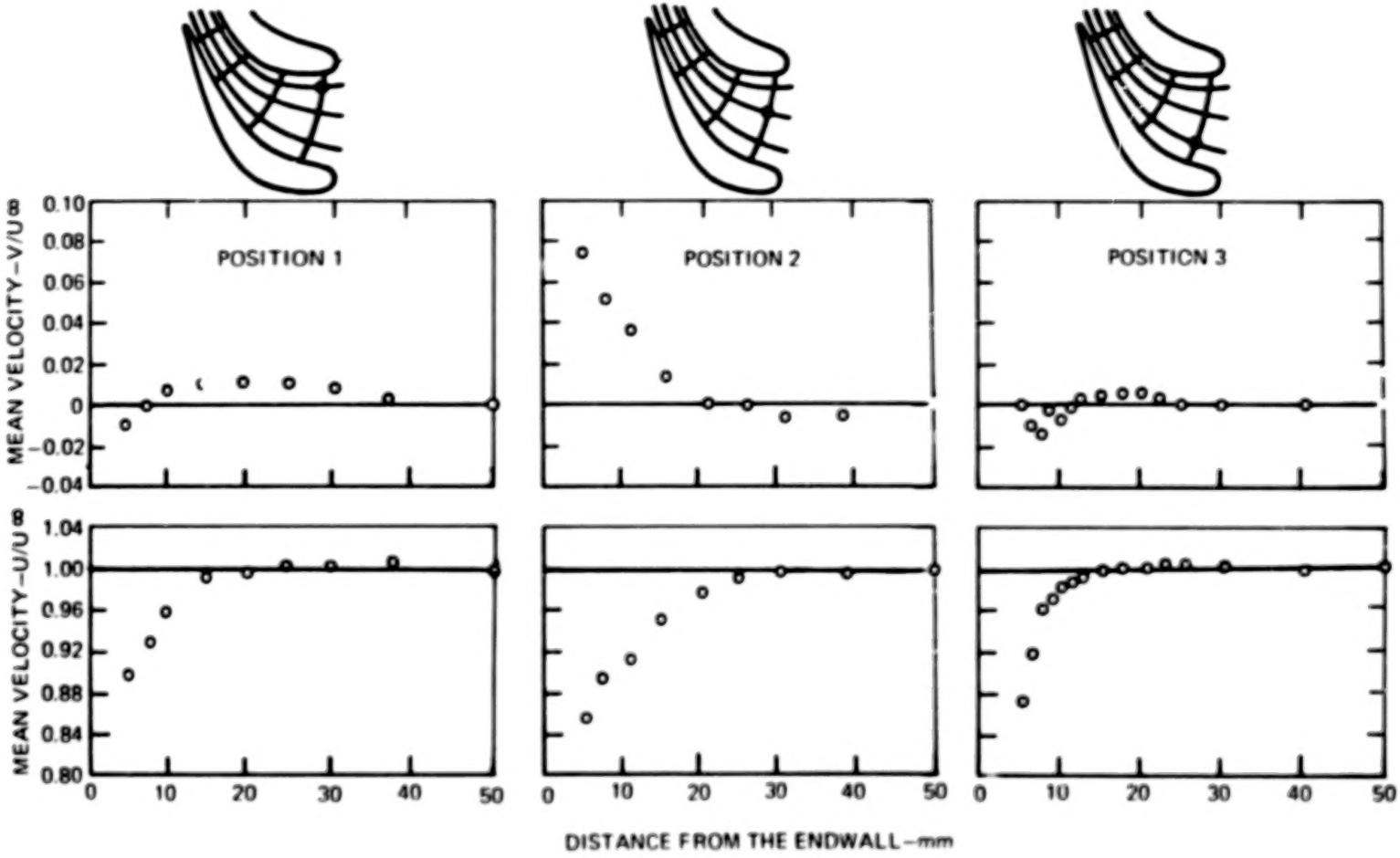

FIGURE 14 – MEAN VELOCITIES VS. DISTANCE FROM THE ENDWALL, FLOW CONDITION A

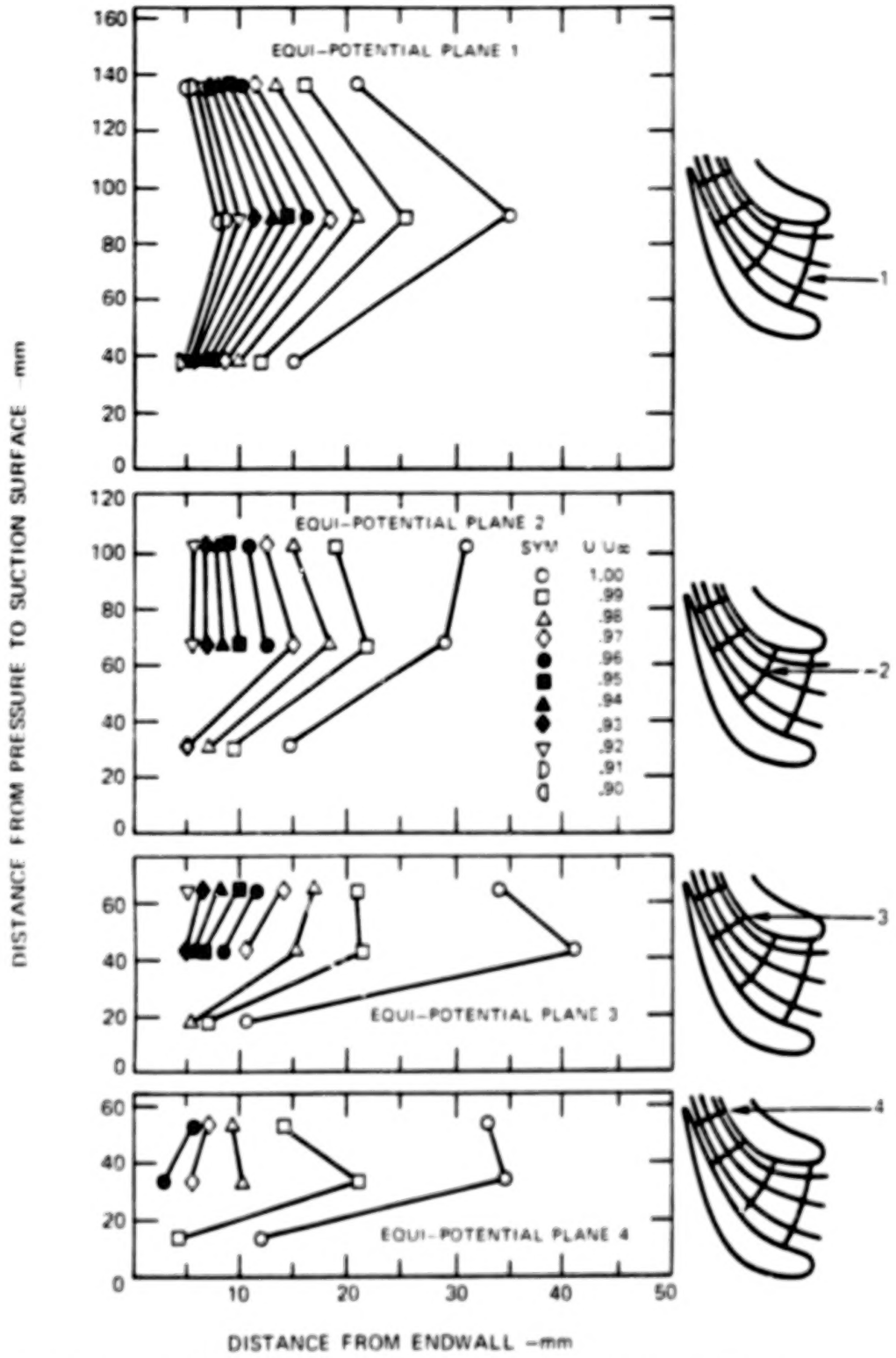

FIGURE 15 – LONGITUDINAL VELOCITY FOR DIFFERENT PLANES FLOW CONDITION A

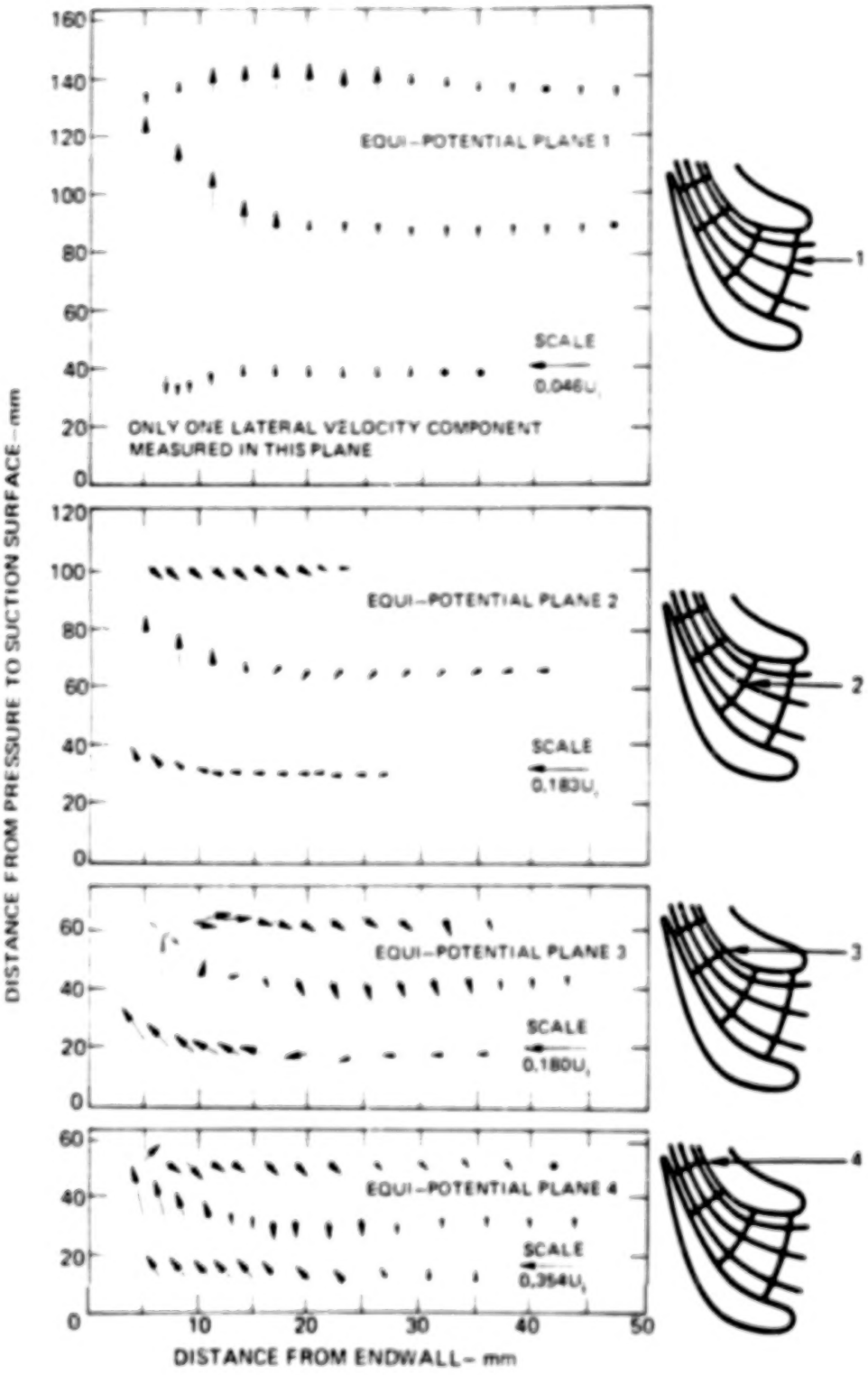

FIGURE 16–LATERAL VELOCITY FOR DIFFERENT PLANES
FLOW CONDITION A

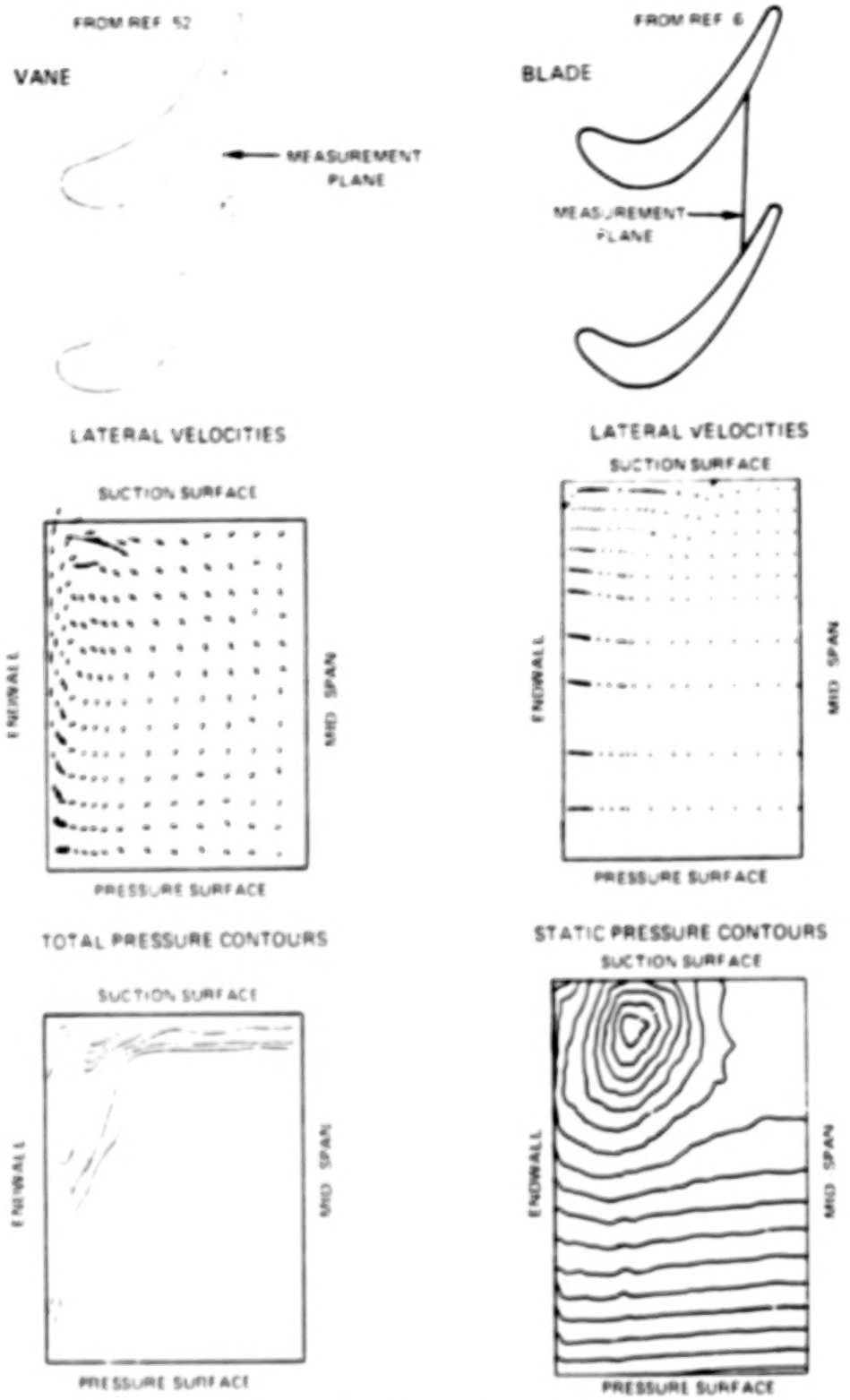

FIGURE 17–COMPARISON OF FLOWS THROUGH TURBINES VANES AND ROTORS

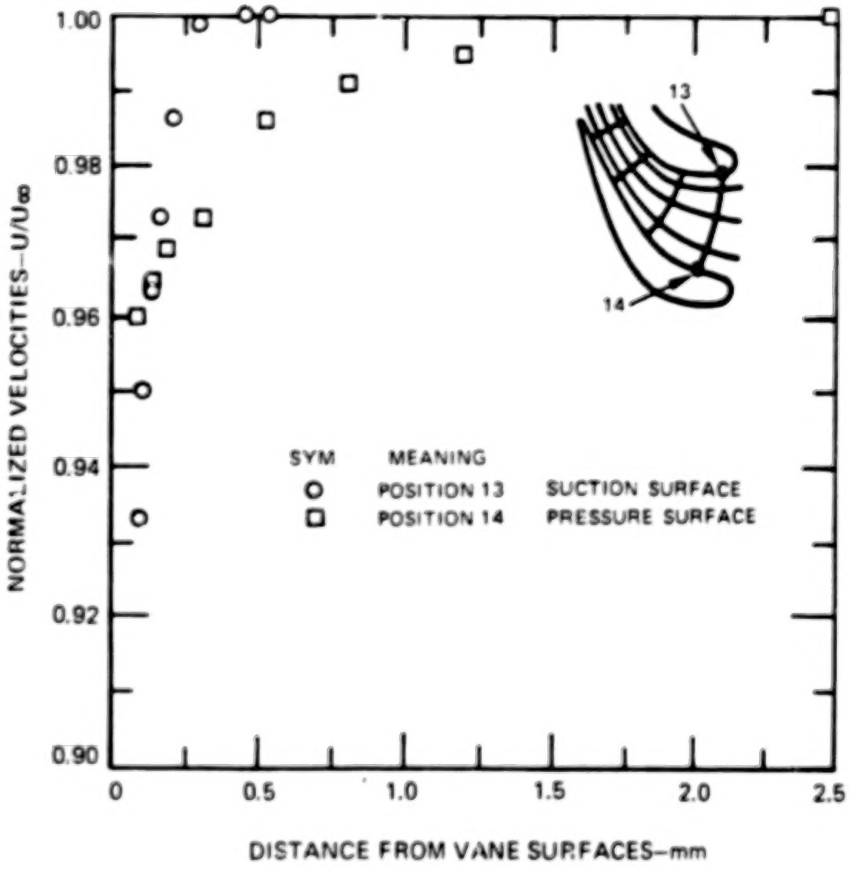

FIGURE 18– MID–SPAN VANE SURFACE BOUNDARY LAYER FLOW CONDITION A

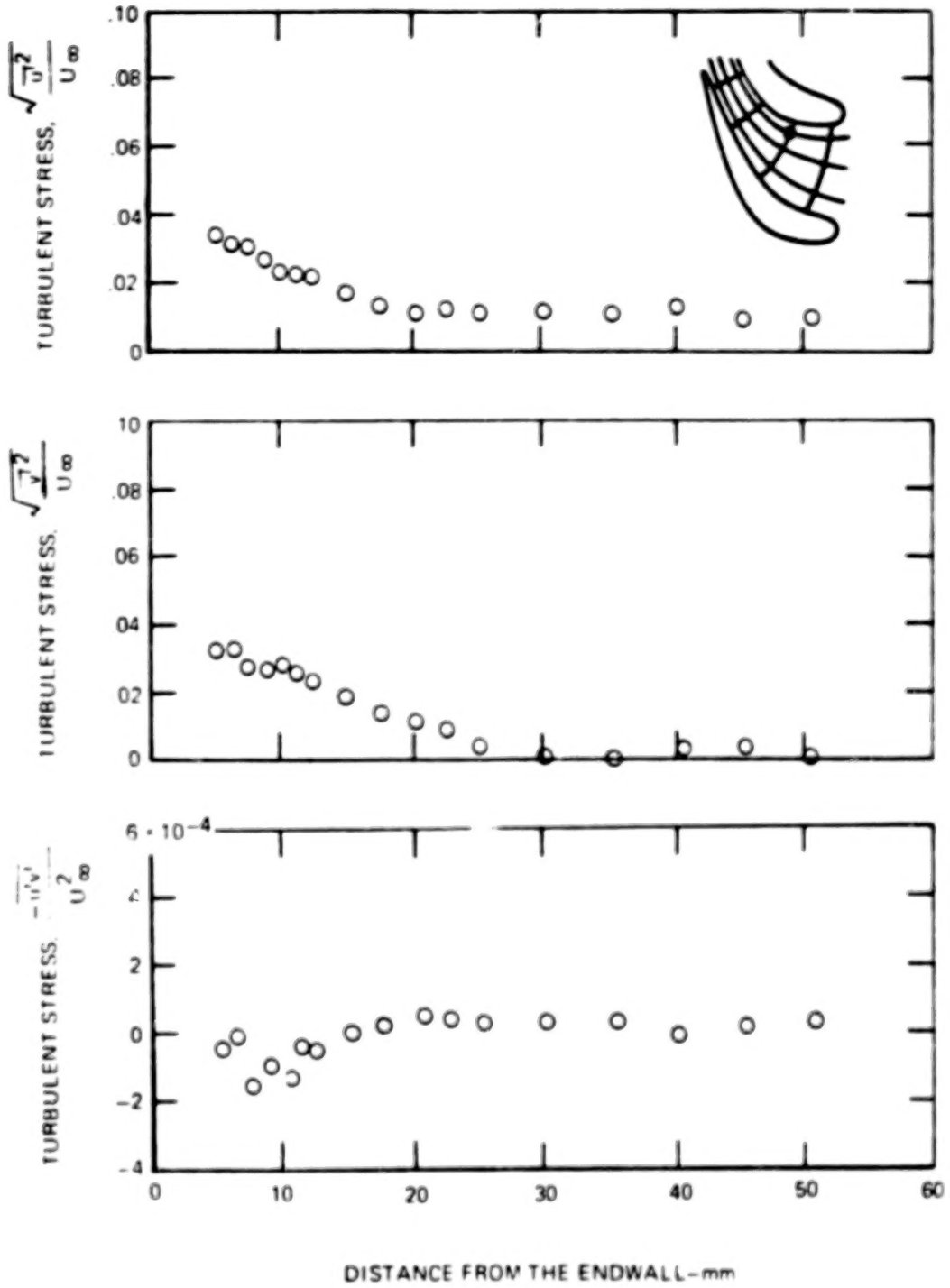

FIGURE 19 – TURBULENT STRESS VS. DISTANCE FROM THE ENDWALL POSITION 4 , FLOW CONDITION A

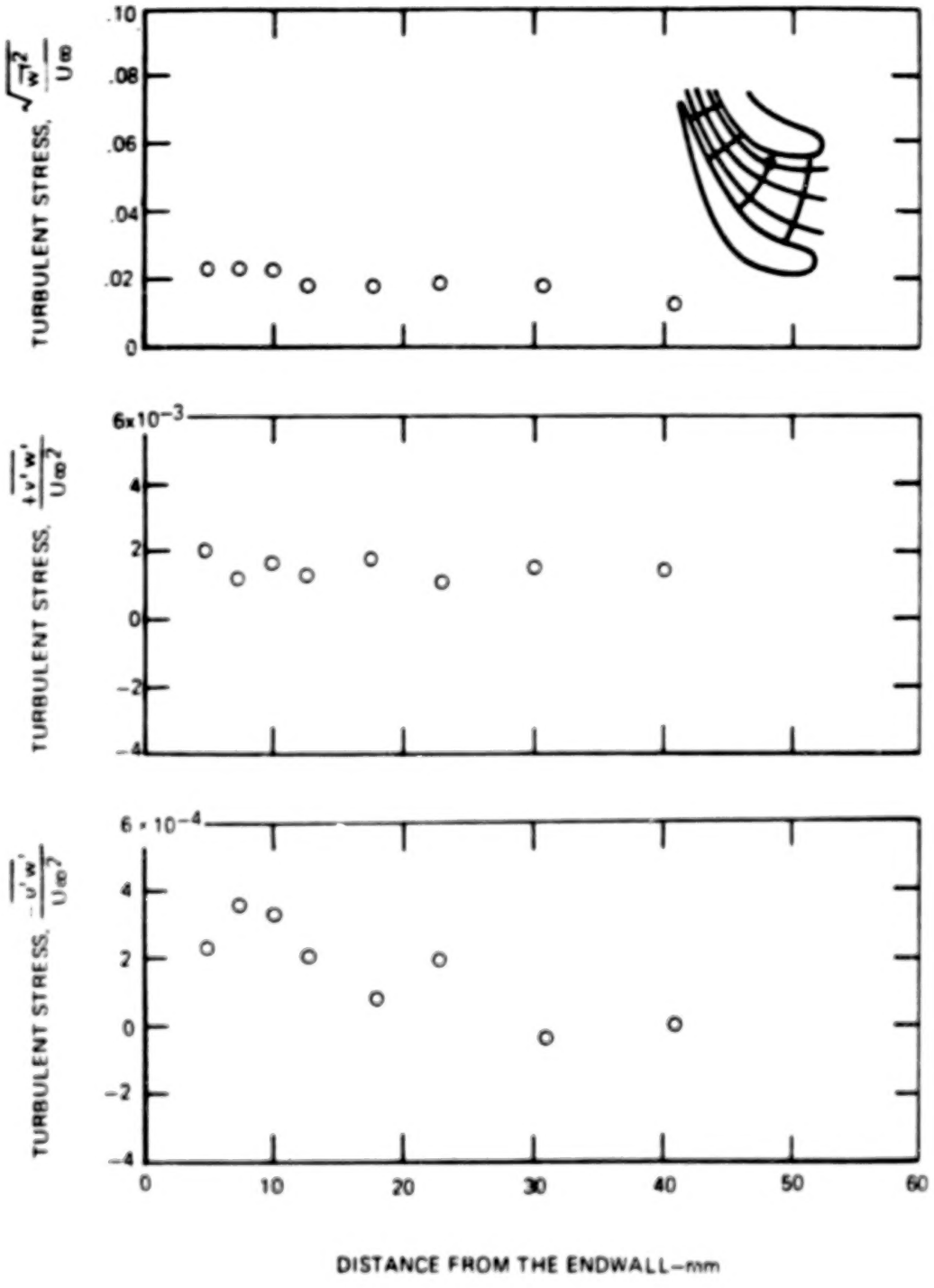

FIGURE 20 – TURBULENT STRESS VS. DISTANCE FROM THE ENDWALL POSITION 4, FLOW CONDITION A

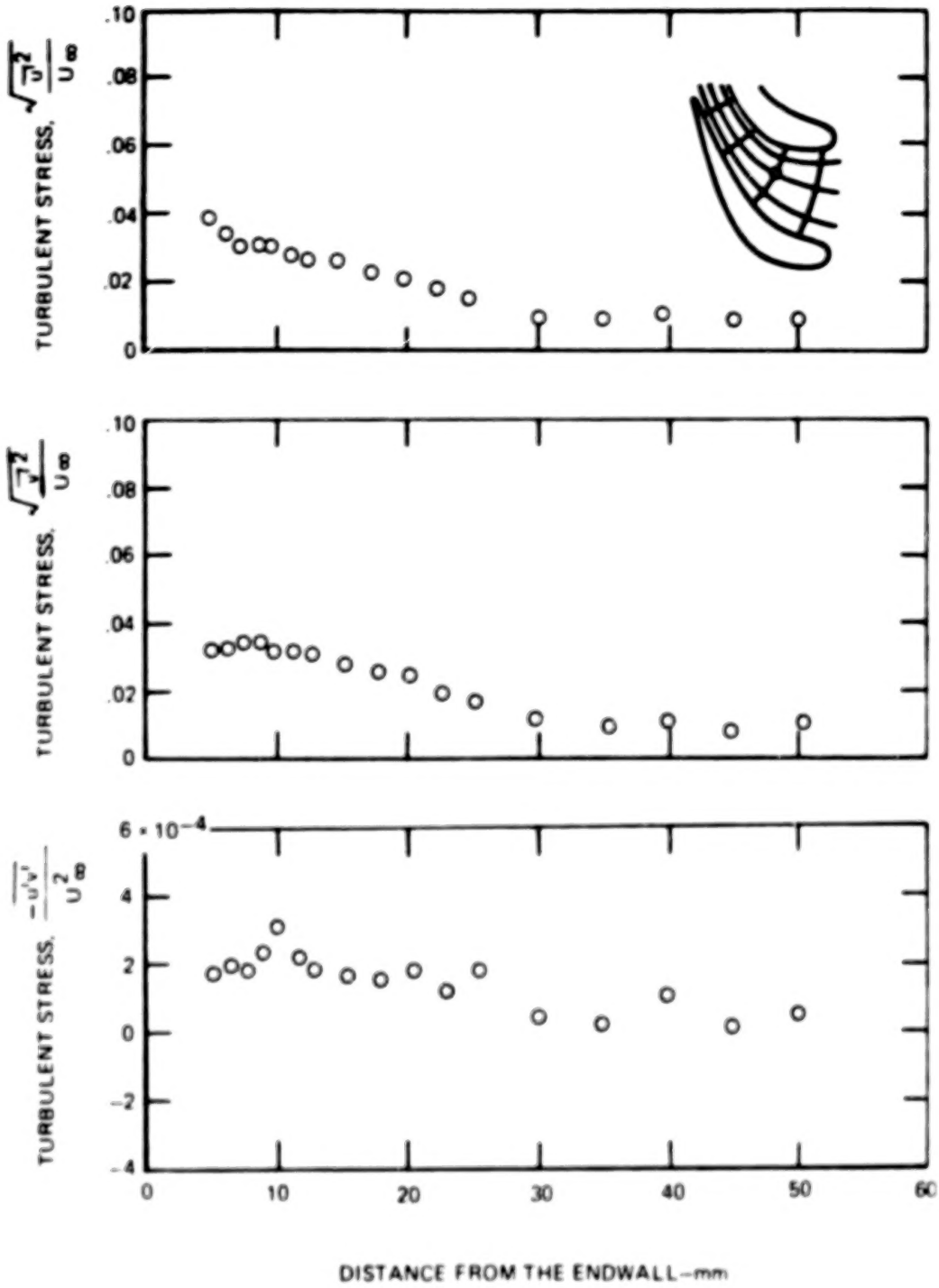

FIGURE 21–TURBULENT STRESS VS. DISTANCE FROM THE ENDWALL
POSITION 5 , FLOW CONDITION A

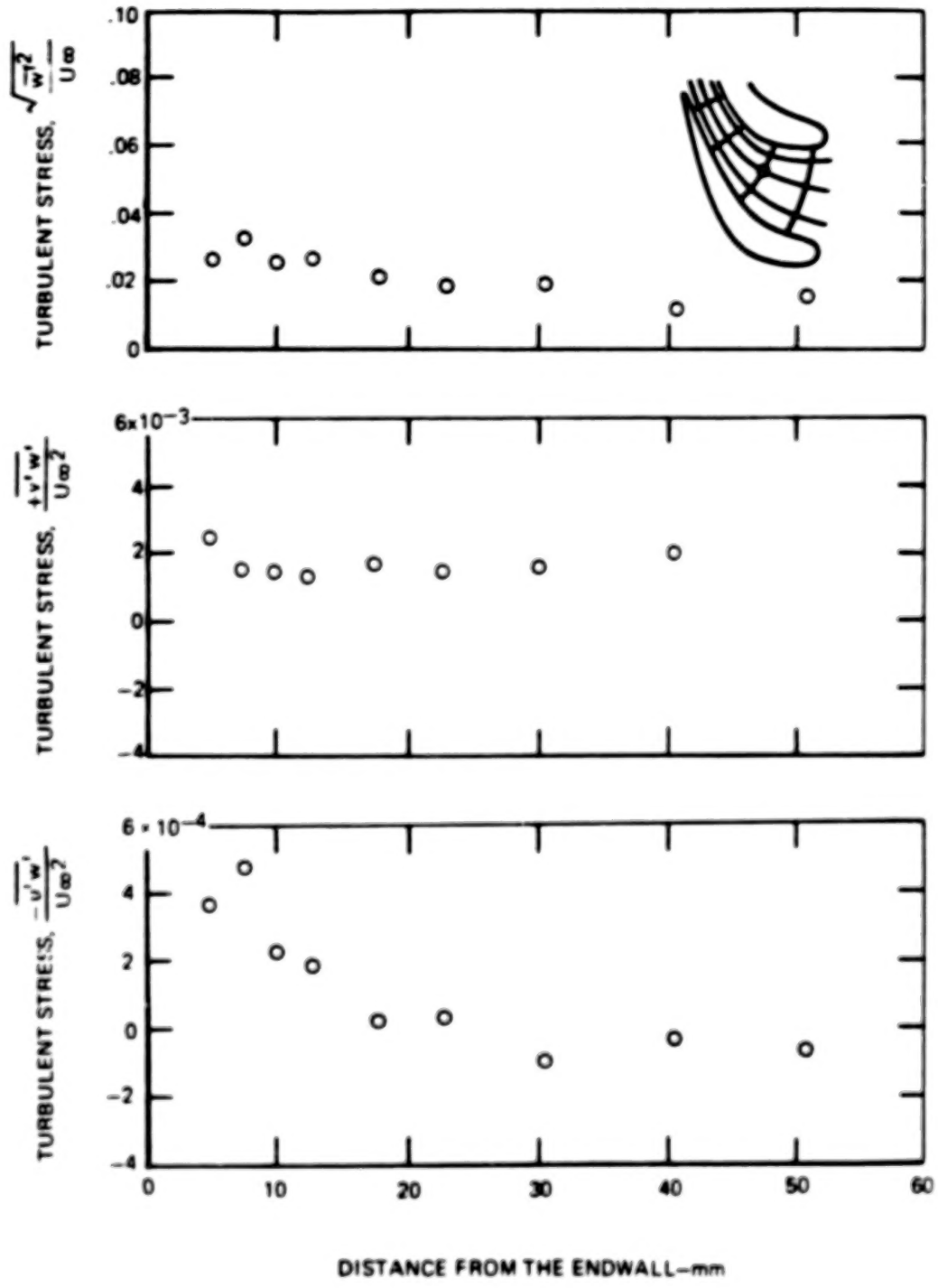

FIGURE 22 – TURBULENT STRESS VS. DISTANCE FROM THE ENDWALL POSITION 5, FLOW CONDITION A

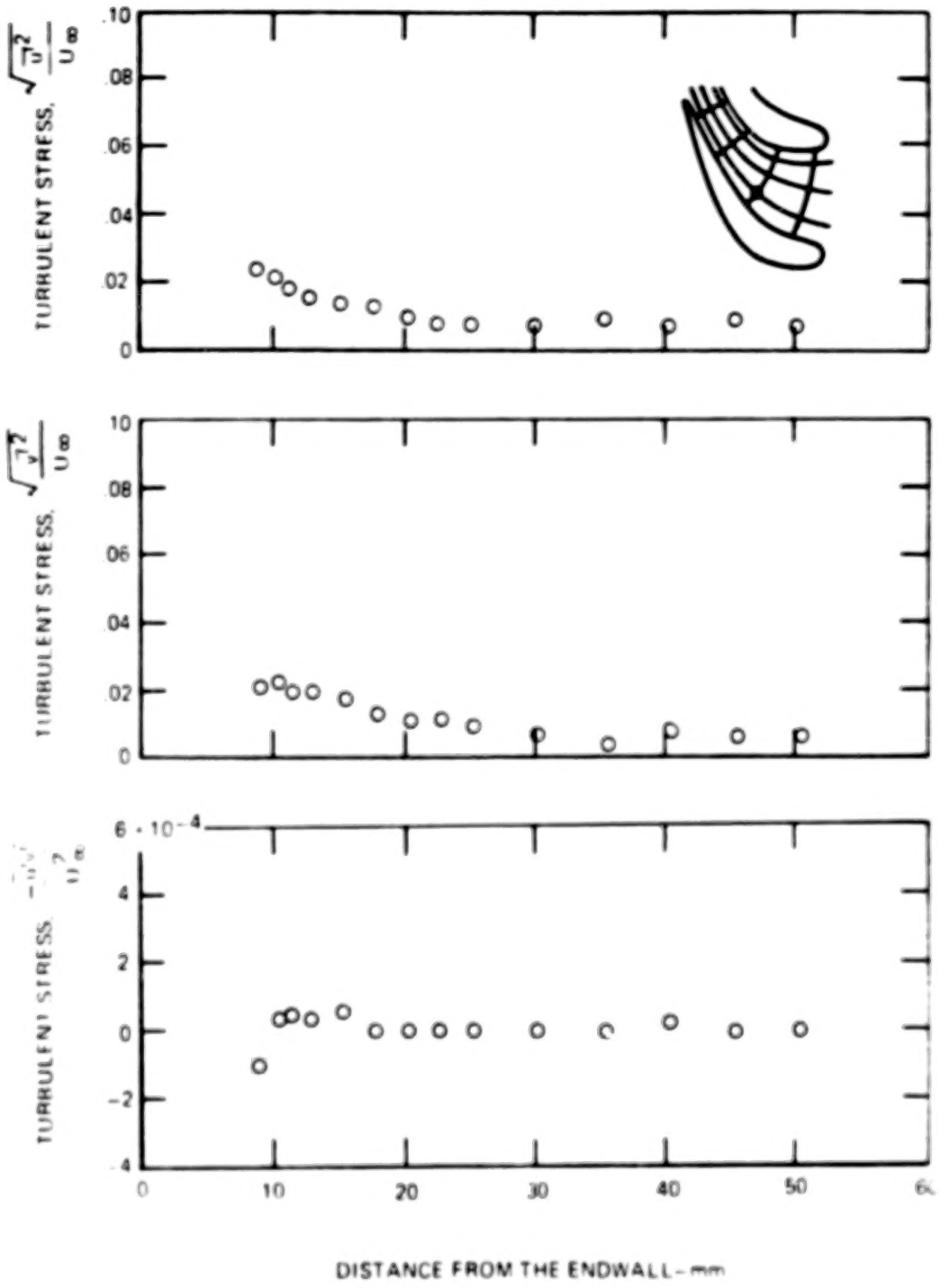

FIGURE 23 – TURBULENT STRESS VS. DISTANCE FROM THE ENDWALL POSITION 6 , FLOW CONDITION A

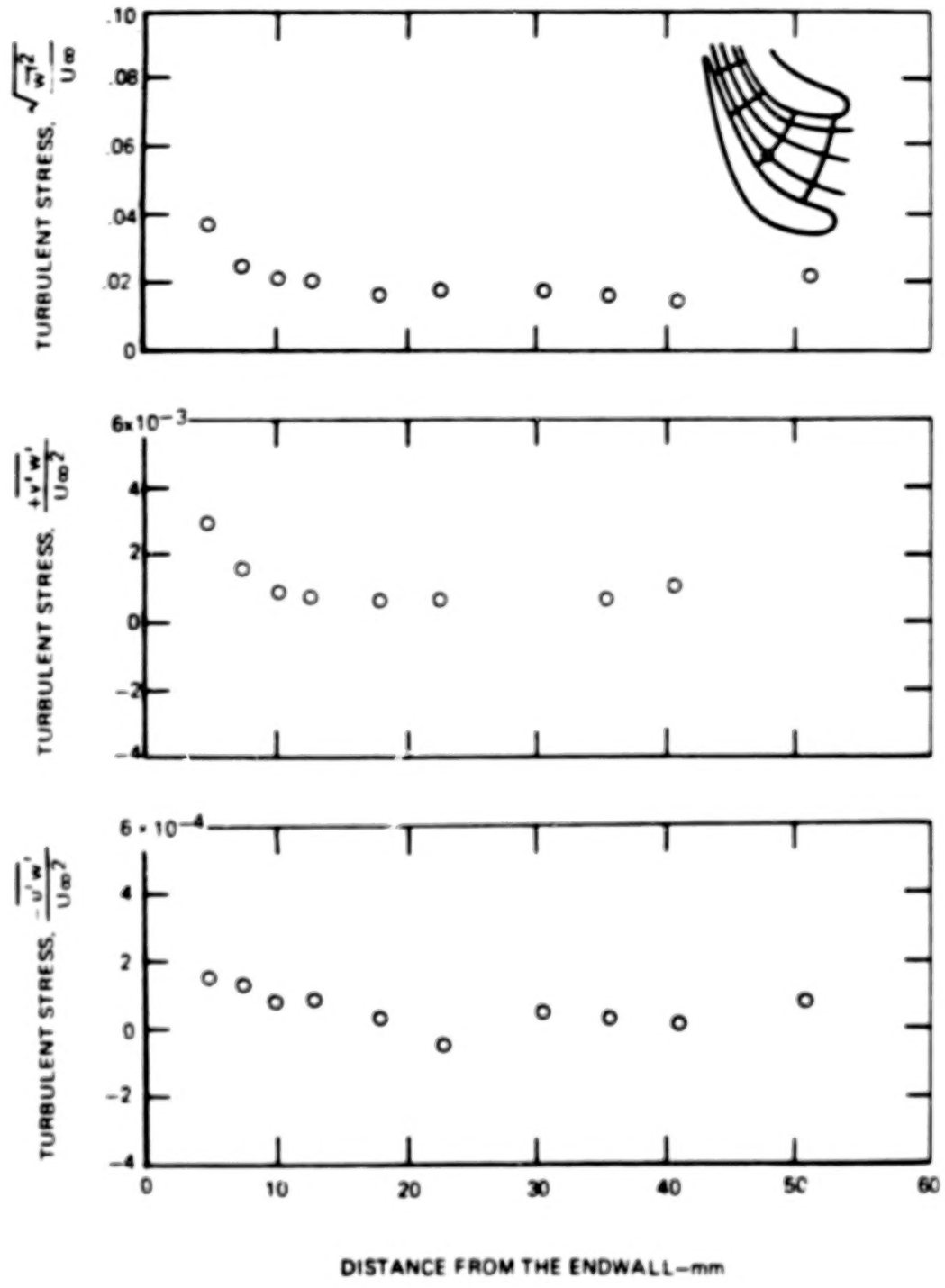

FIGURE 24 – TURBULENT STRESS VS. DISTANCE FROM THE ENDWALL POSITION 6, FLOW CONDITION A

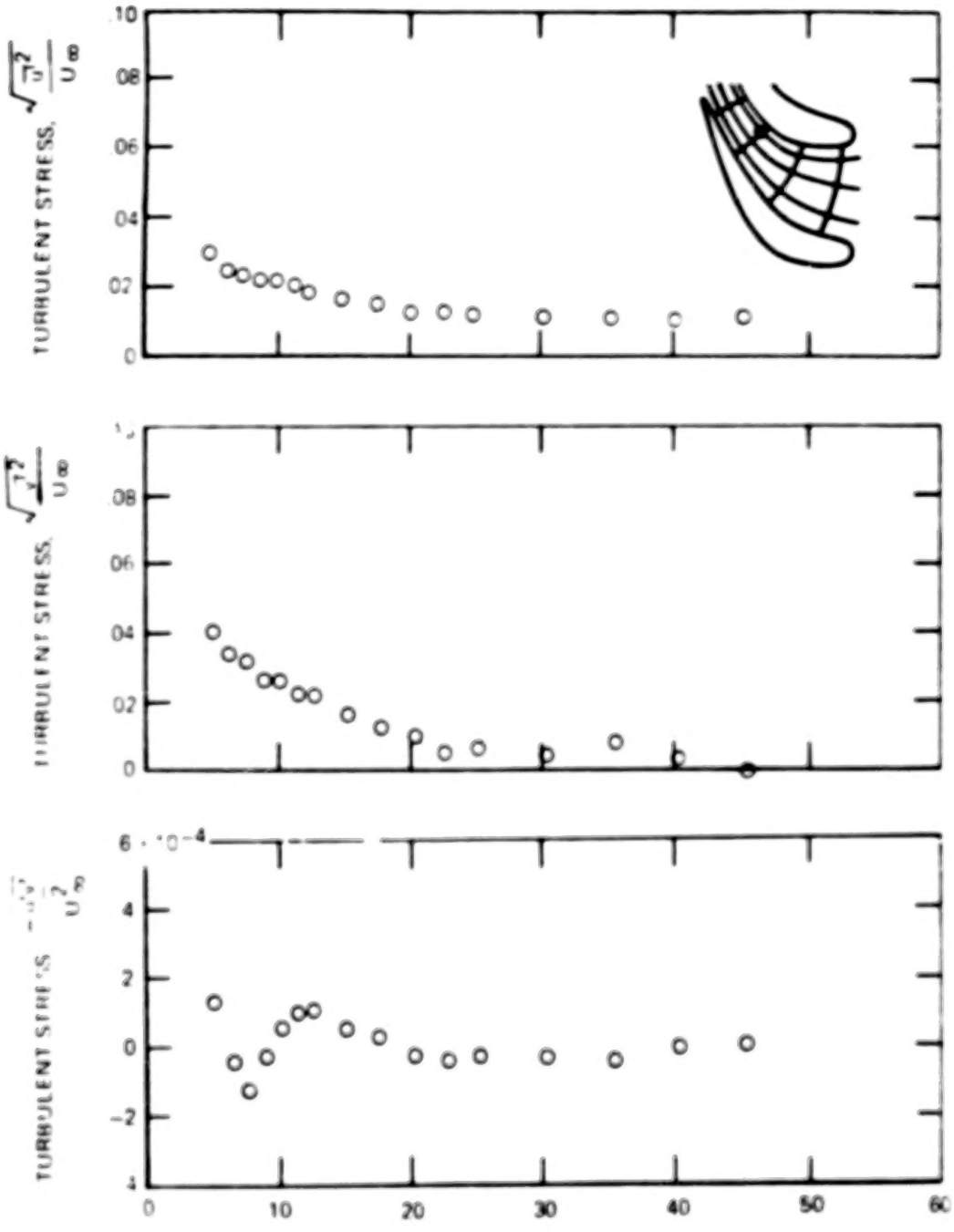

FIGURE 25 - TURBULENT STRESS VS. DISTANCE FROM THE ENDWALL POSITION 7 , FLOW CONDITION A

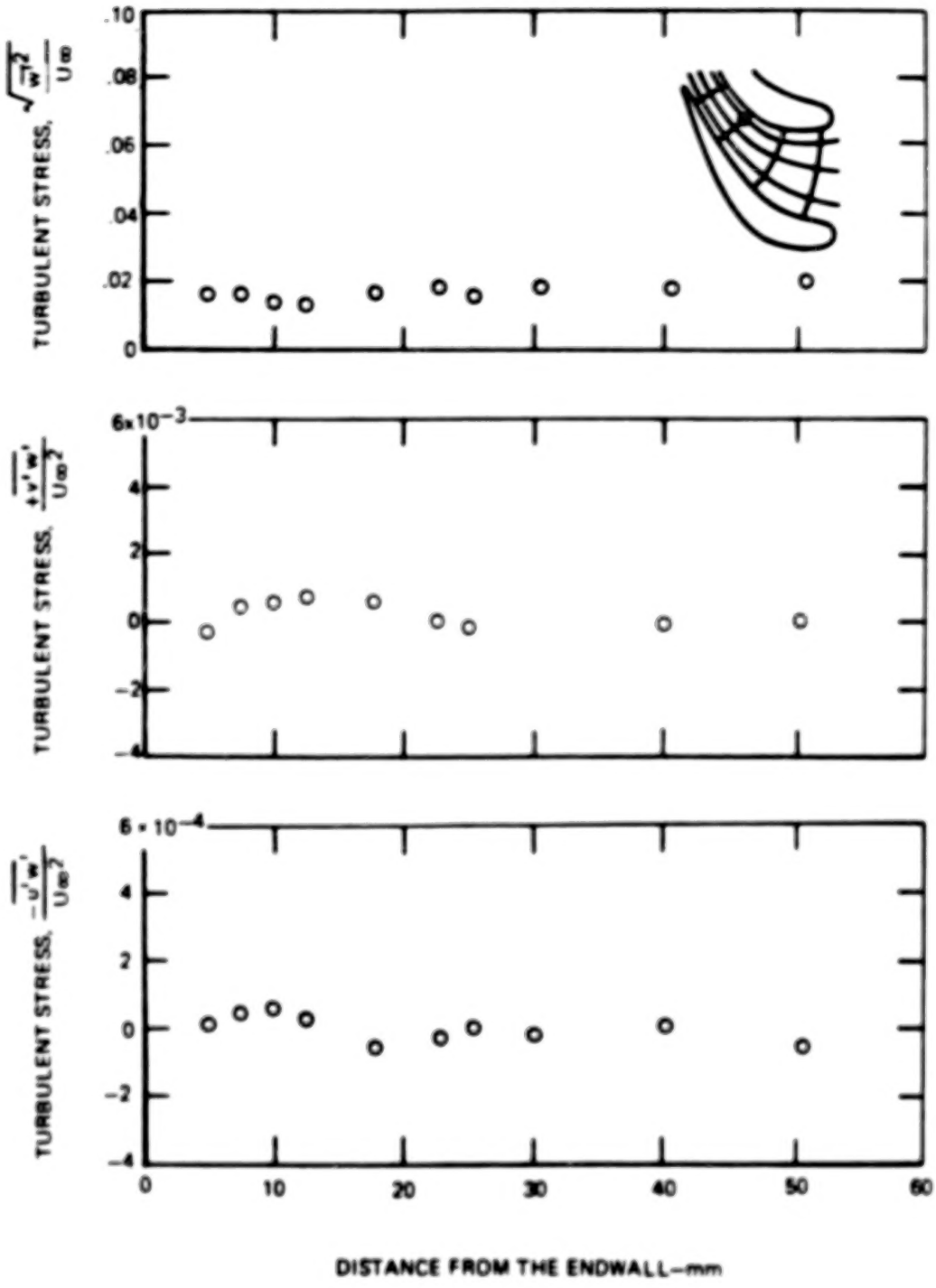

FIGURE 26—TURBULENT STRESS VS. DISTANCE FROM THE ENDWALL POSITION 7, FLOW CONDITION A

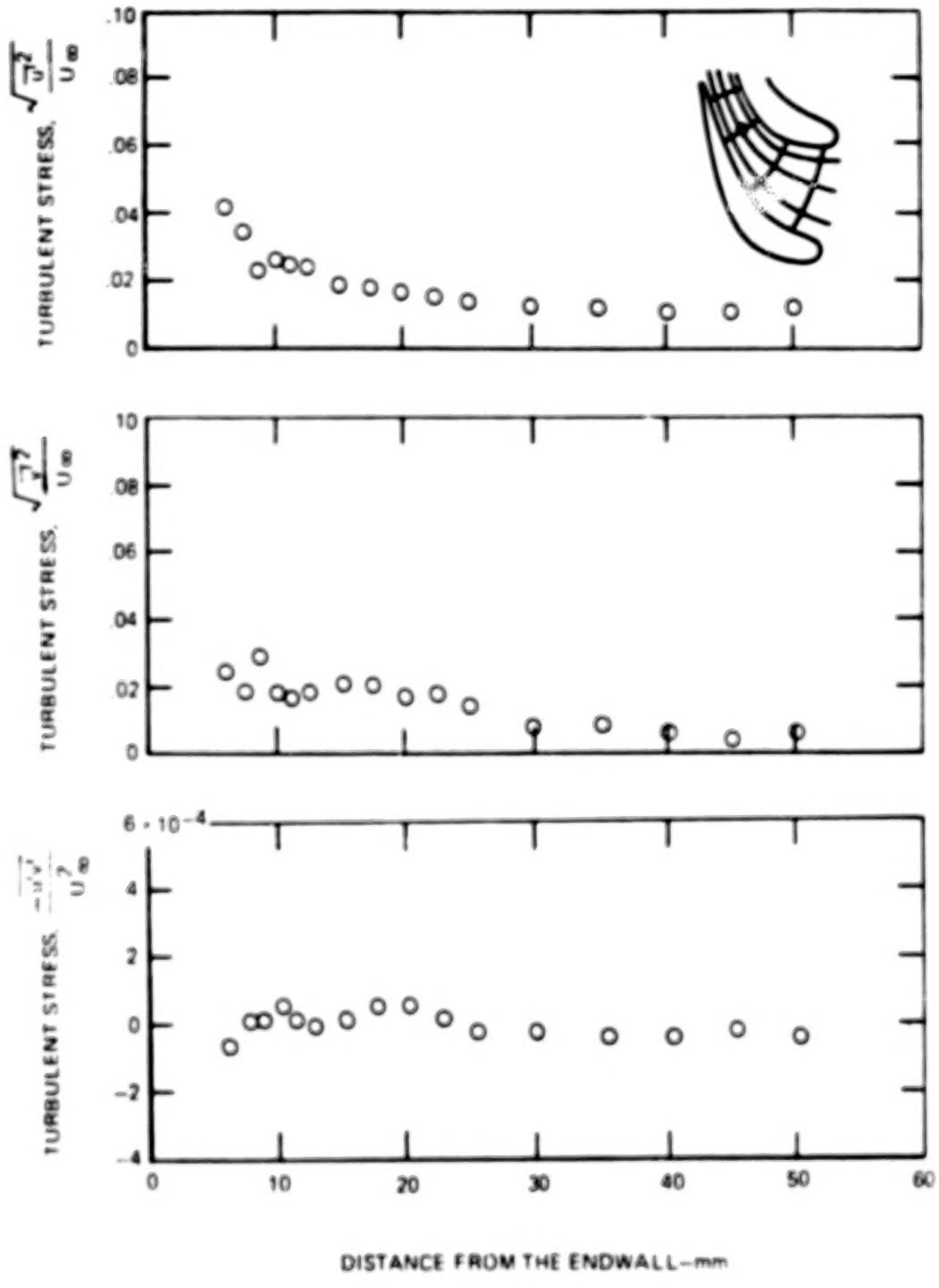

FIGURE 27 – TURBULENT STRESS VS. DISTANCE FROM THE ENDWALL POSITION 8 , FLOW CONDITION A

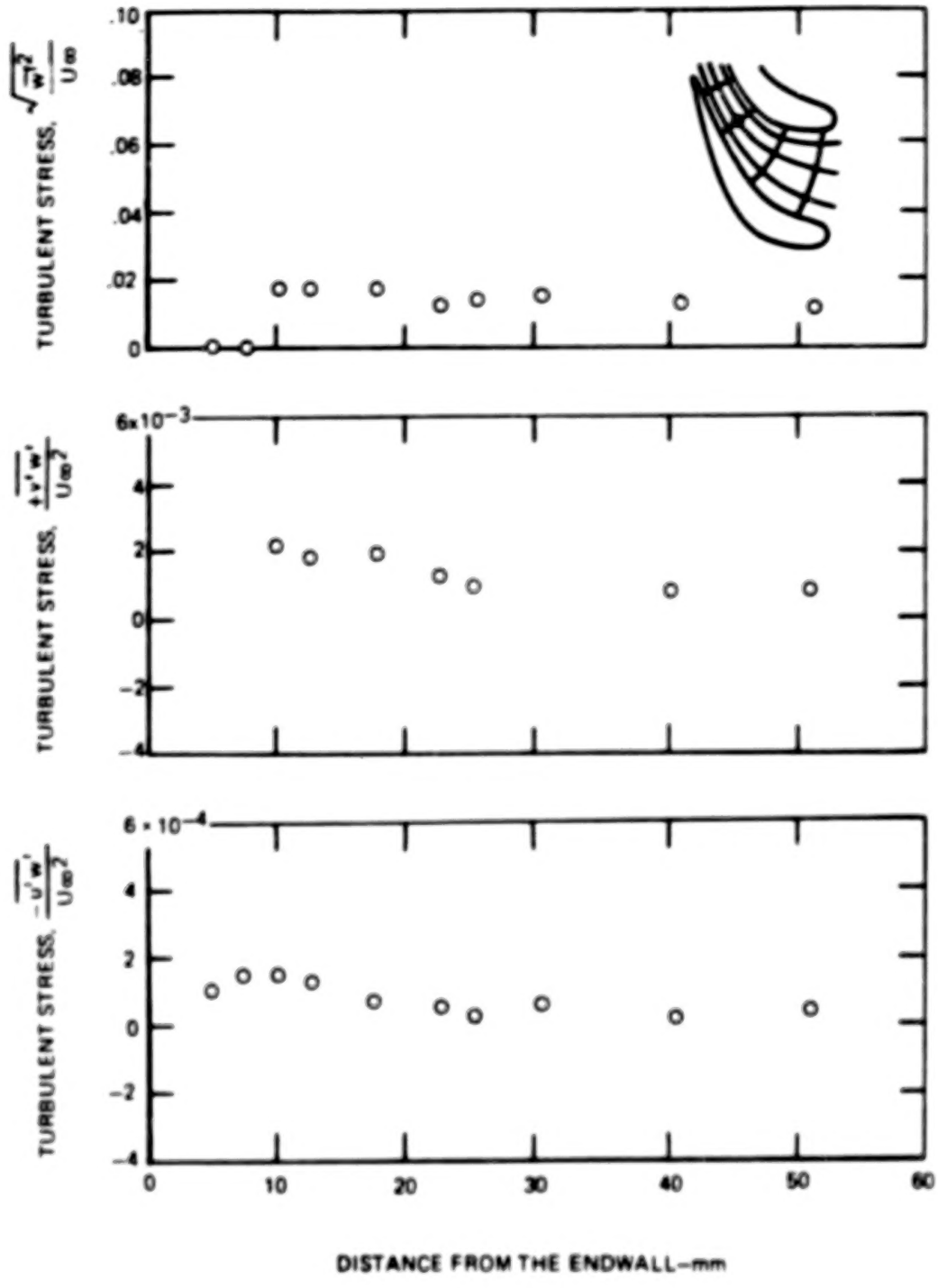

FIGURE 28 – TURBULENT STRESS VS. DISTANCE FROM THE ENDWALL POSITION 8, FLOW CONDITION A

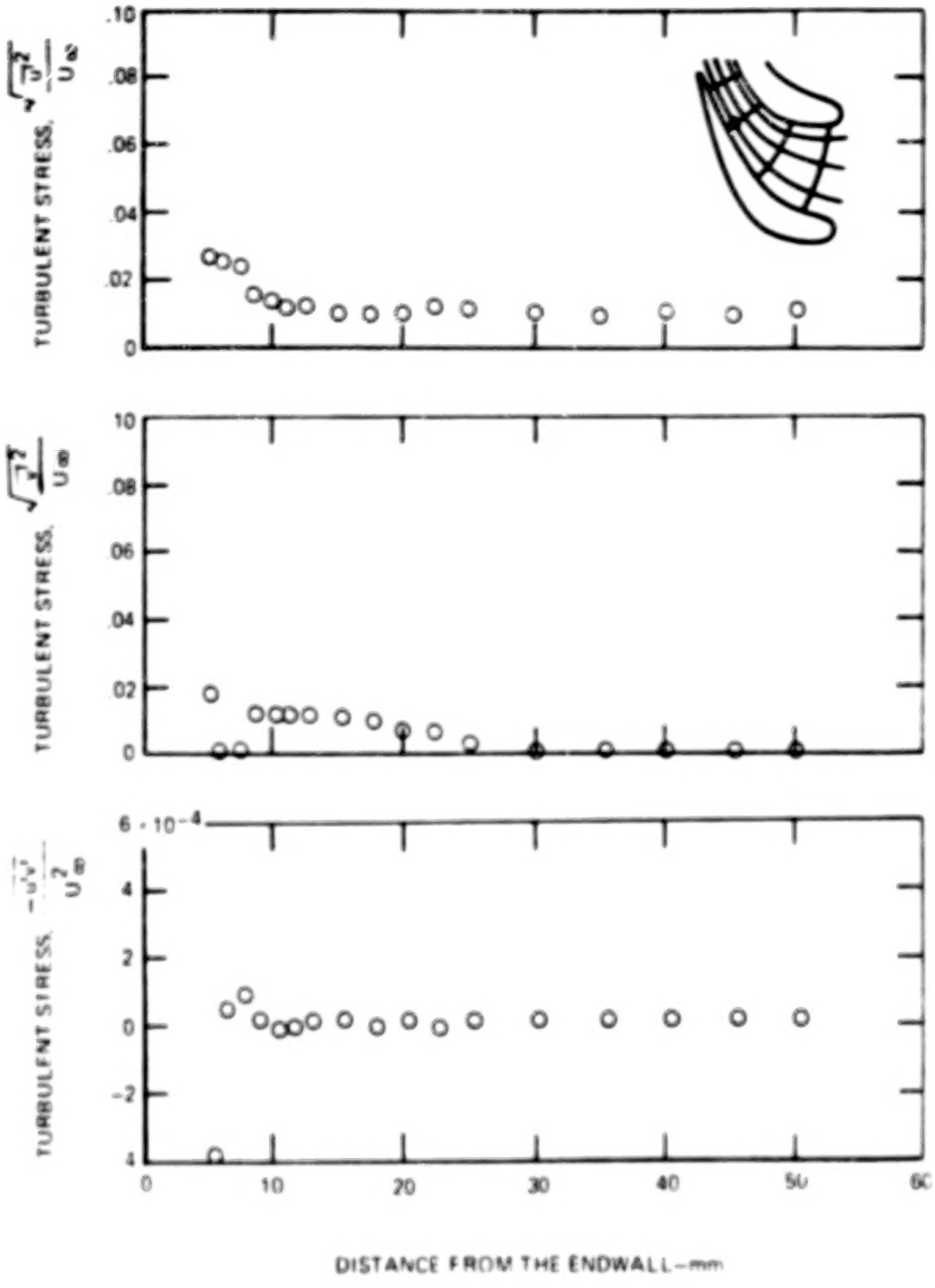

FIGURE 29 – TURBULENT STRESS VS. DISTANCE FROM THE ENDWALL POSITION 9 , FLOW CONDITION A

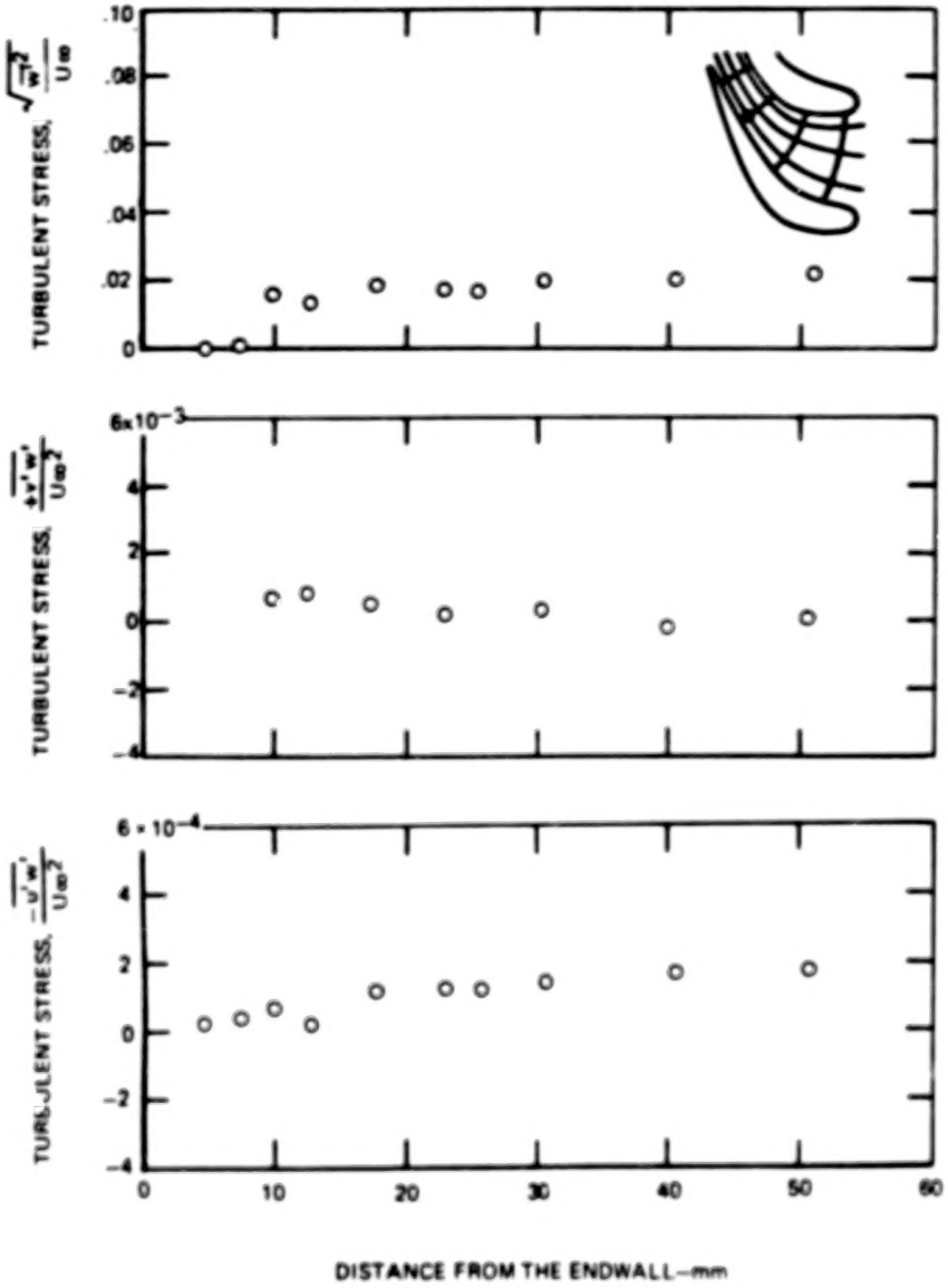

FIGURE 30–TURBULENT STRESS VS. DISTANCE FROM THE ENDWALL POSITION 9, FLOW CONDITION A

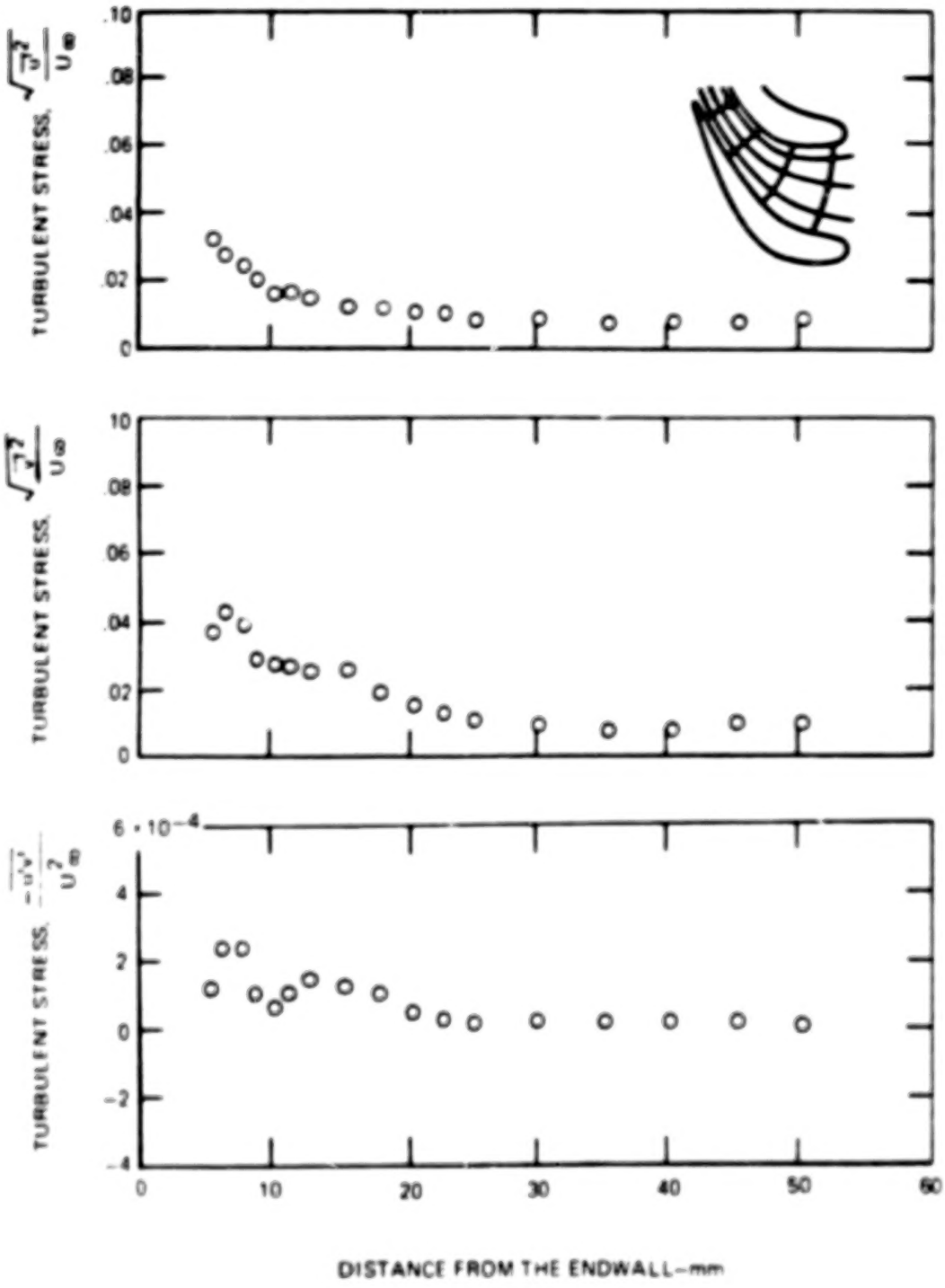

FIGURE 31 – TURBULENT STRESS VS. DISTANCE FROM THE ENDWALL
POSITION 10, FLOW CONDITION A

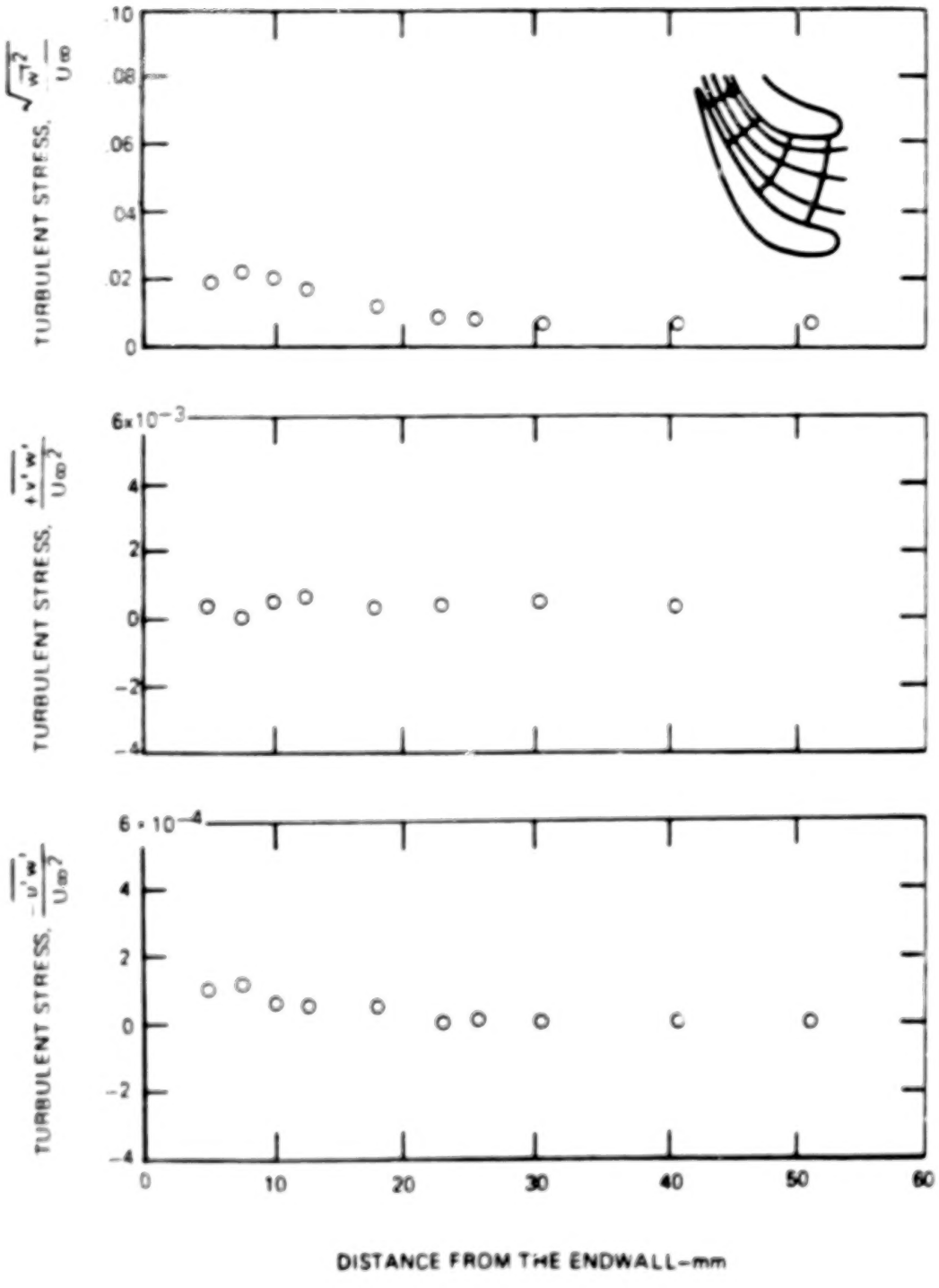

FIGURE 32 – TURBULENT STRESS VS. DISTANCE FROM THE ENDWALL POSITION 10, FLOW CONDITION A

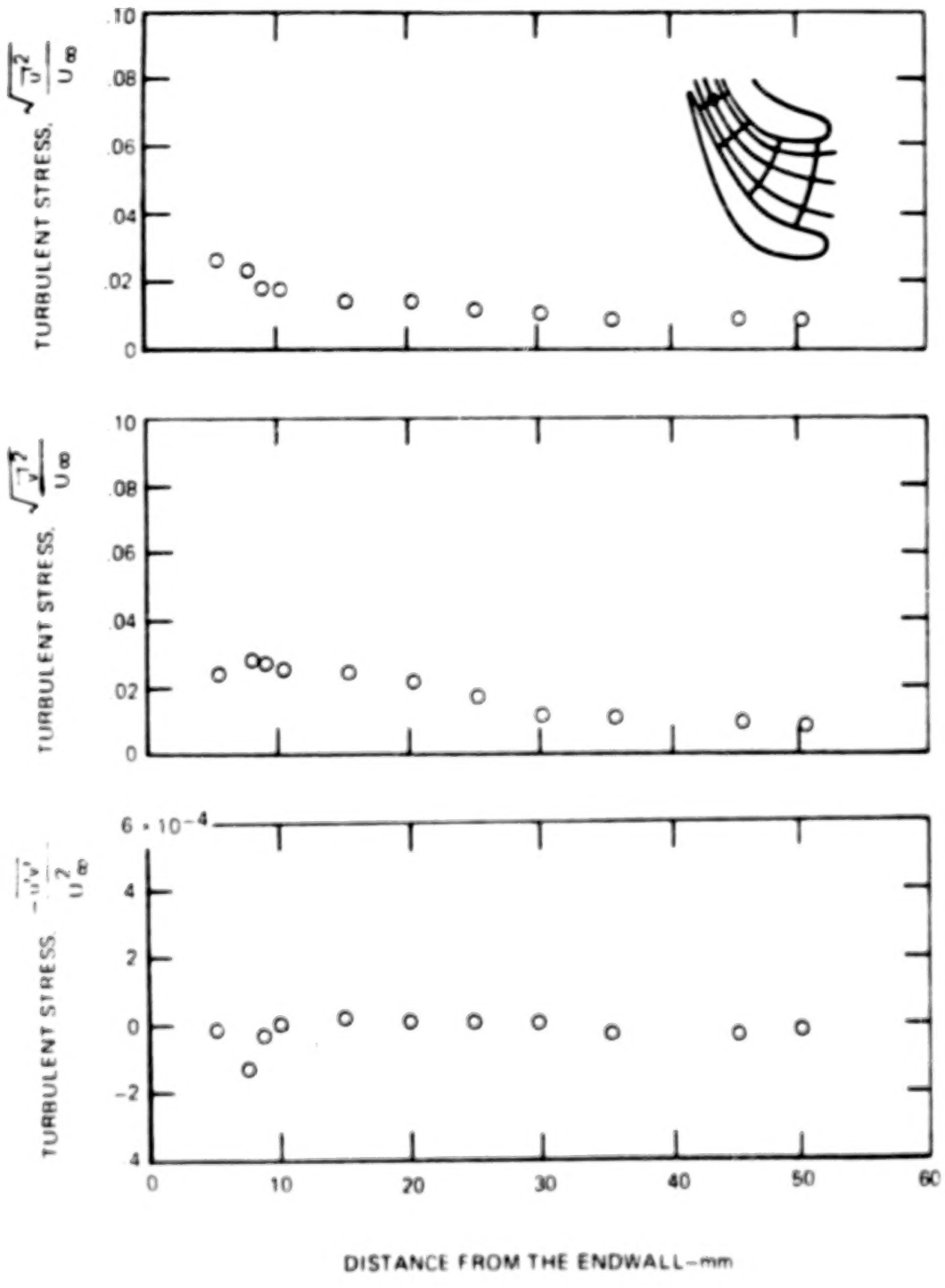

FIGURE 33 – TURBULENT STRESS VS. DISTANCE FROM THE ENDWALL POSITION 11, FLOW CONDITION A

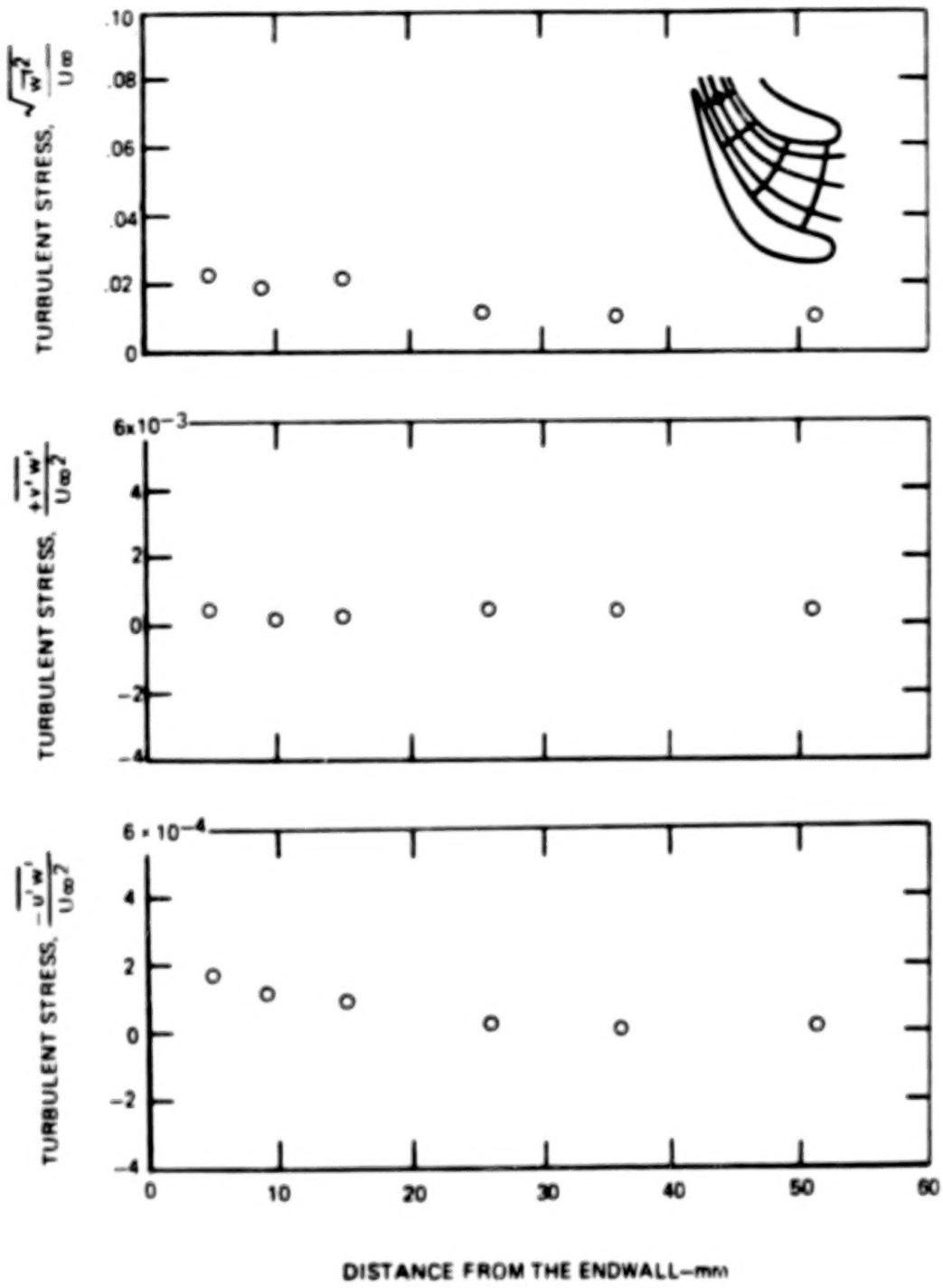

FIGURE 34 – TURBULENT STRESS VS. DISTANCE FROM THE ENDWALL POSITION 11, FLOW CONDITION A

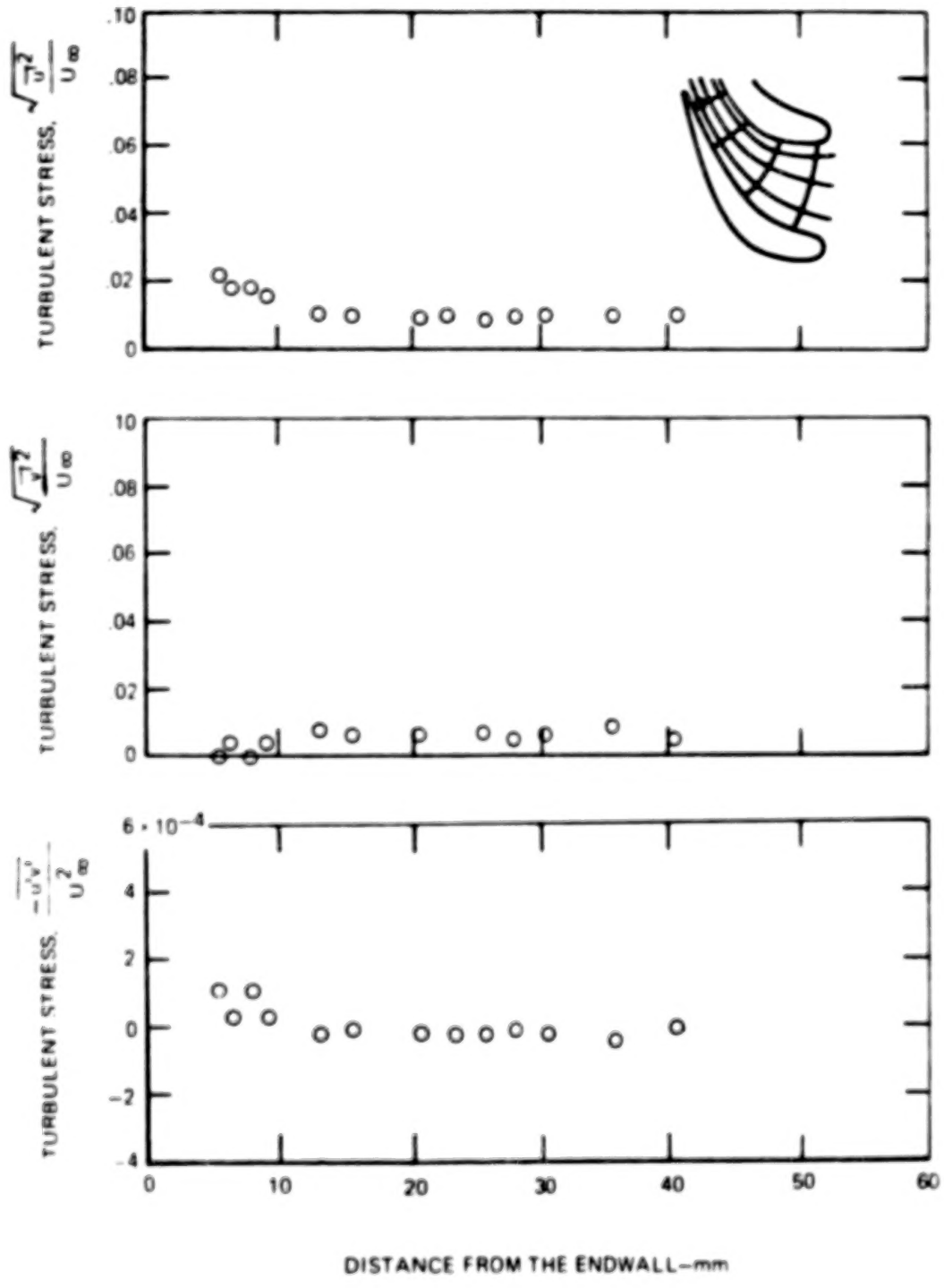

FIGURE 35 – TURBULENT STRESS VS. DISTANCE FROM THE ENDWALL POSITION 12, FLOW CONDITION A

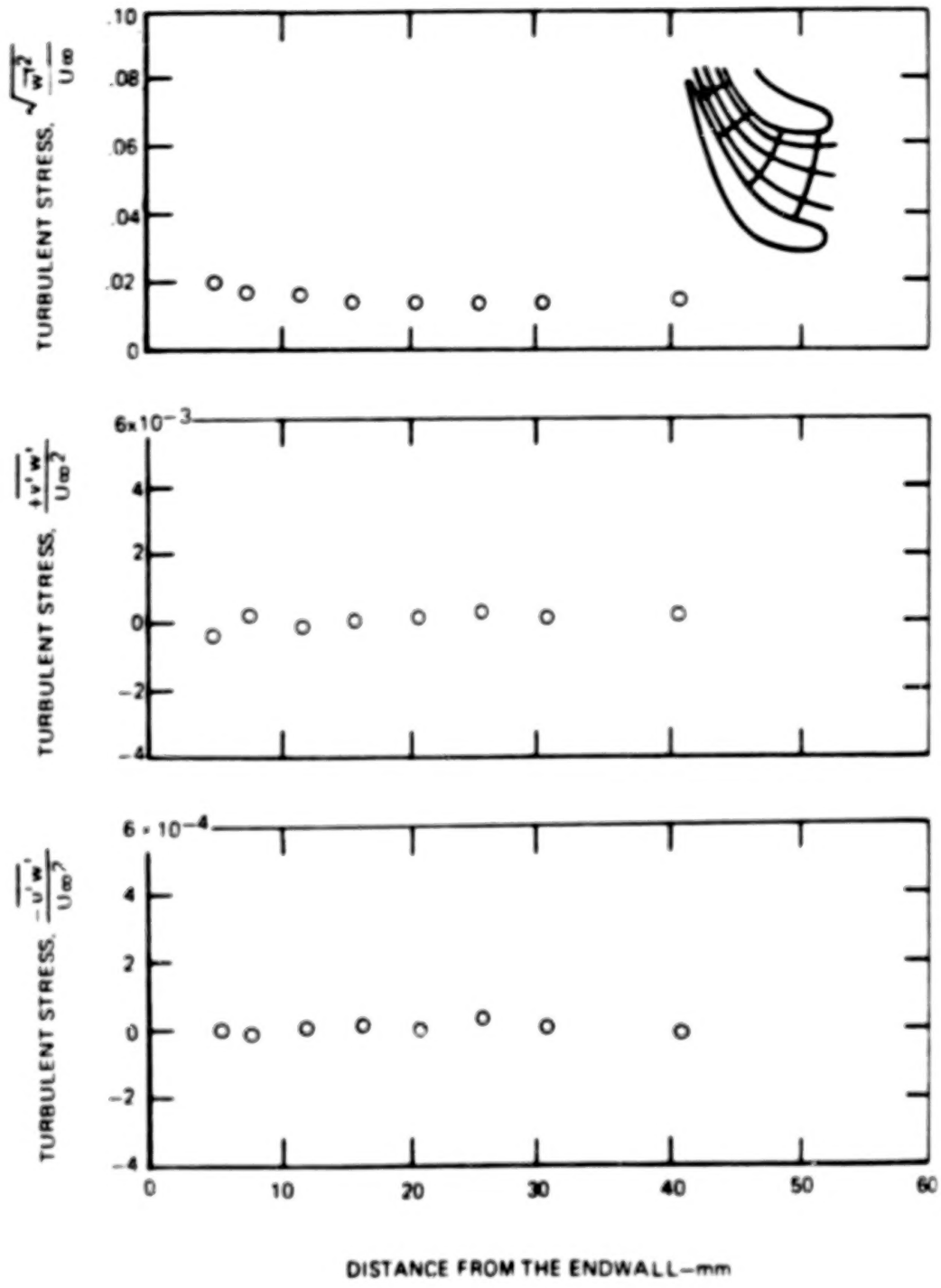

FIGURE 36—TURBULENT STRESS VS. DISTANCE FROM THE ENDWALL POSITION 12, FLOW CONDITION A

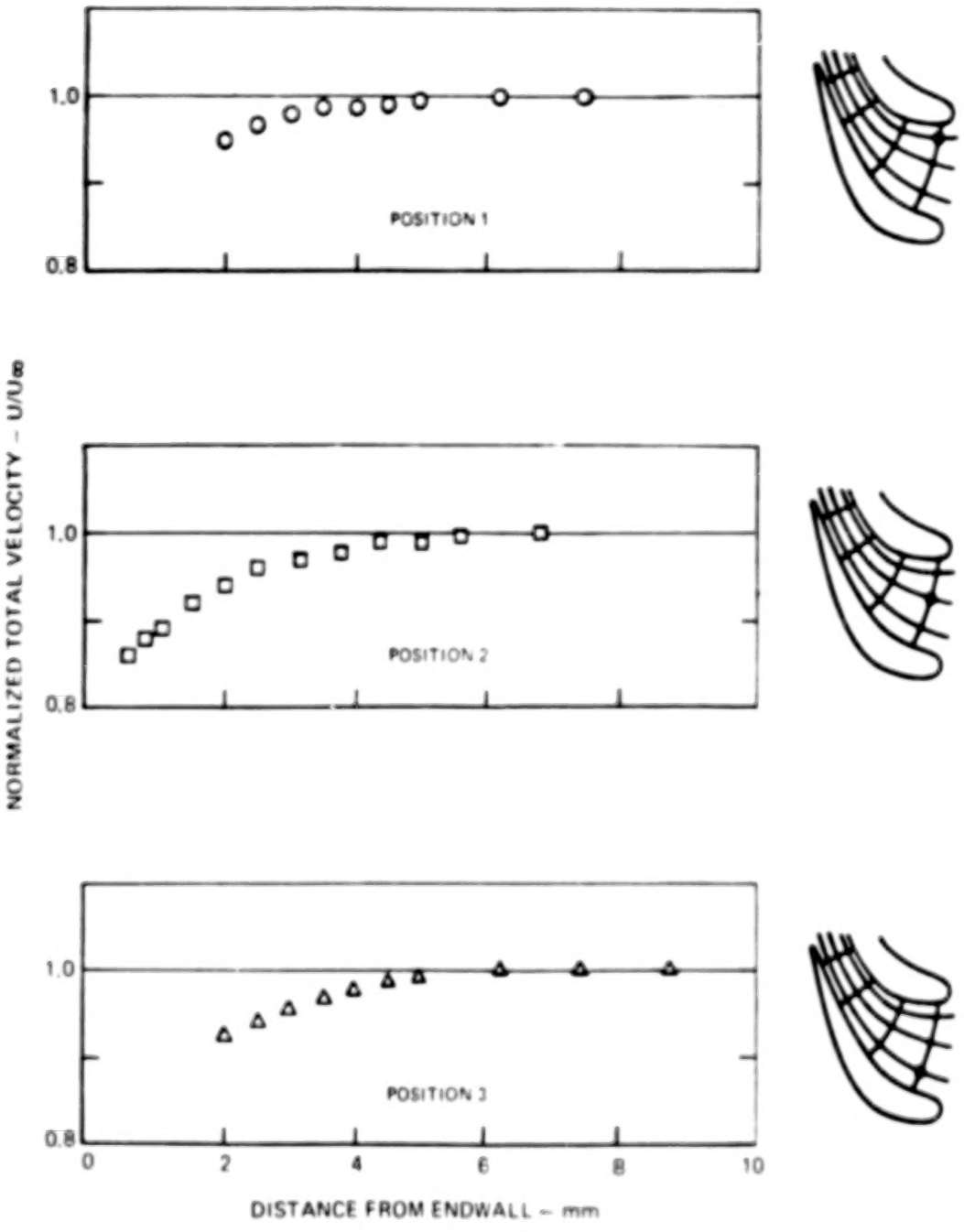

FIGURE 37 – MEAN VELOCITIES VS DISTANCE FROM THE ENDWALL FLOW CONDITION C

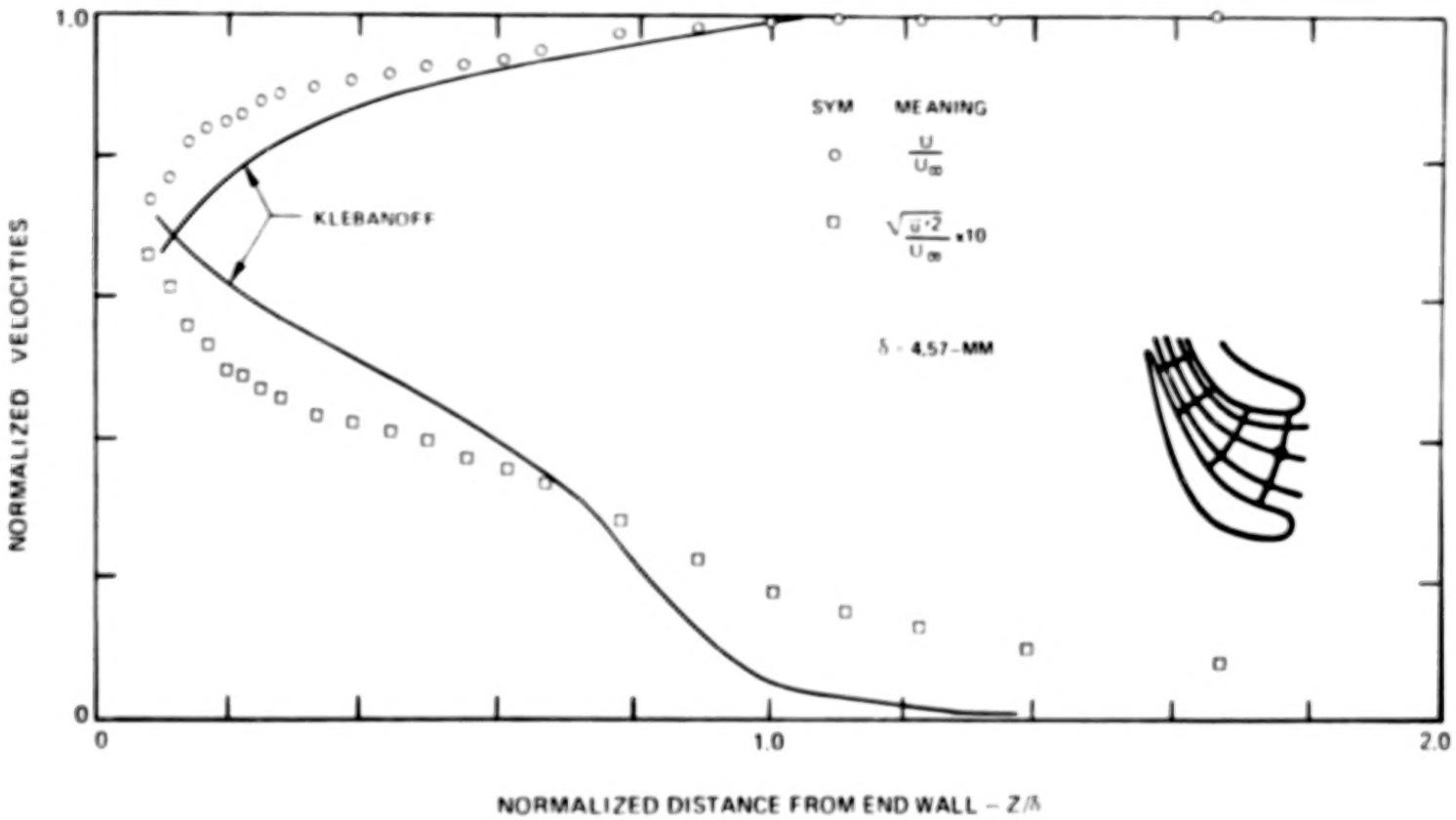

FIGURE 38 – NORMALIZED MEAN AND TURBULENT VELOCITIES VS. DISTANCE FROM THE WALL–POSITION 2, FLOW CONDITION "C".

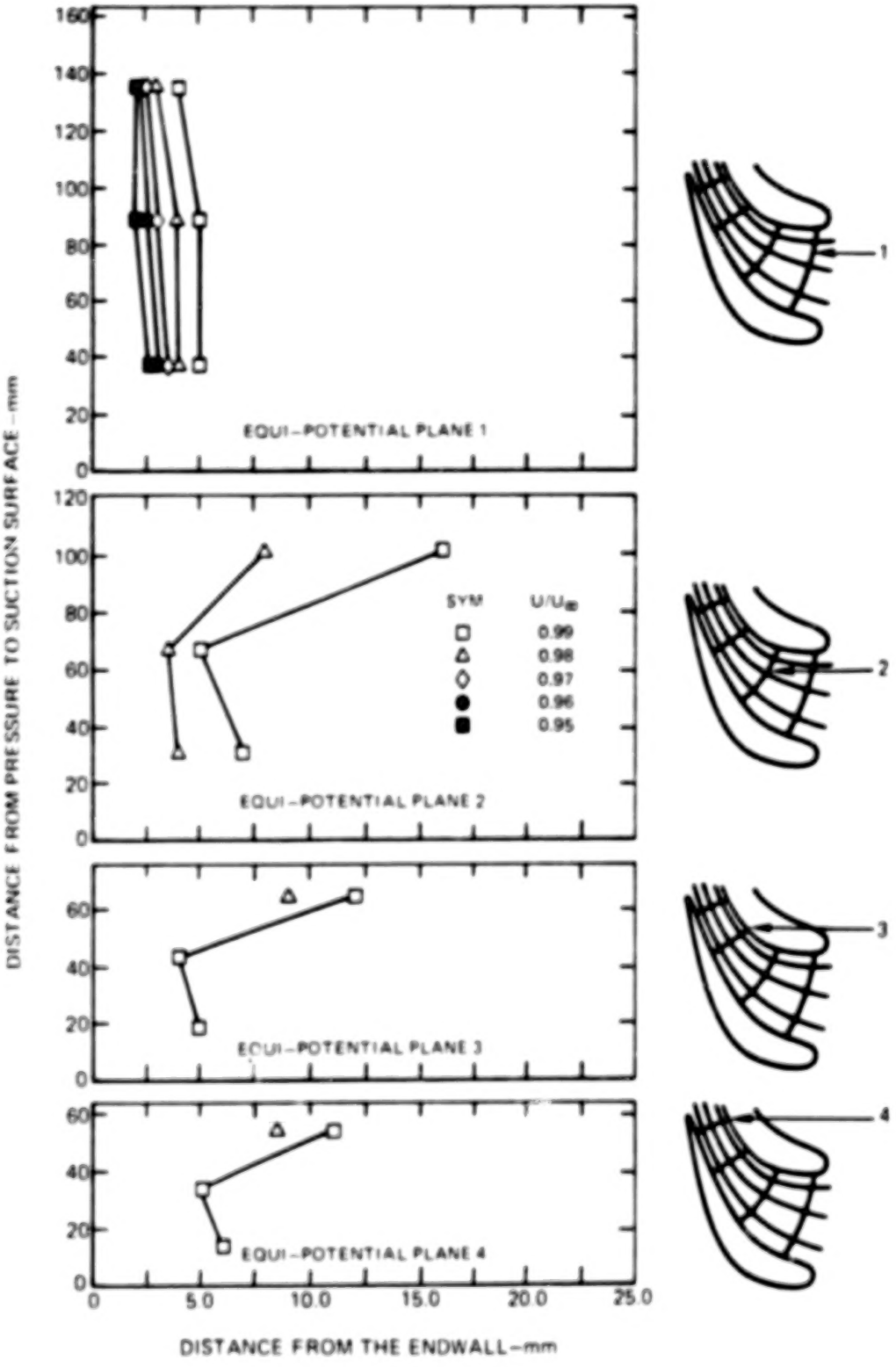

FIGURE 39–LONGITUDINAL VELOCITY FOR DIFFERENT PLANES FLOW CONDITION C

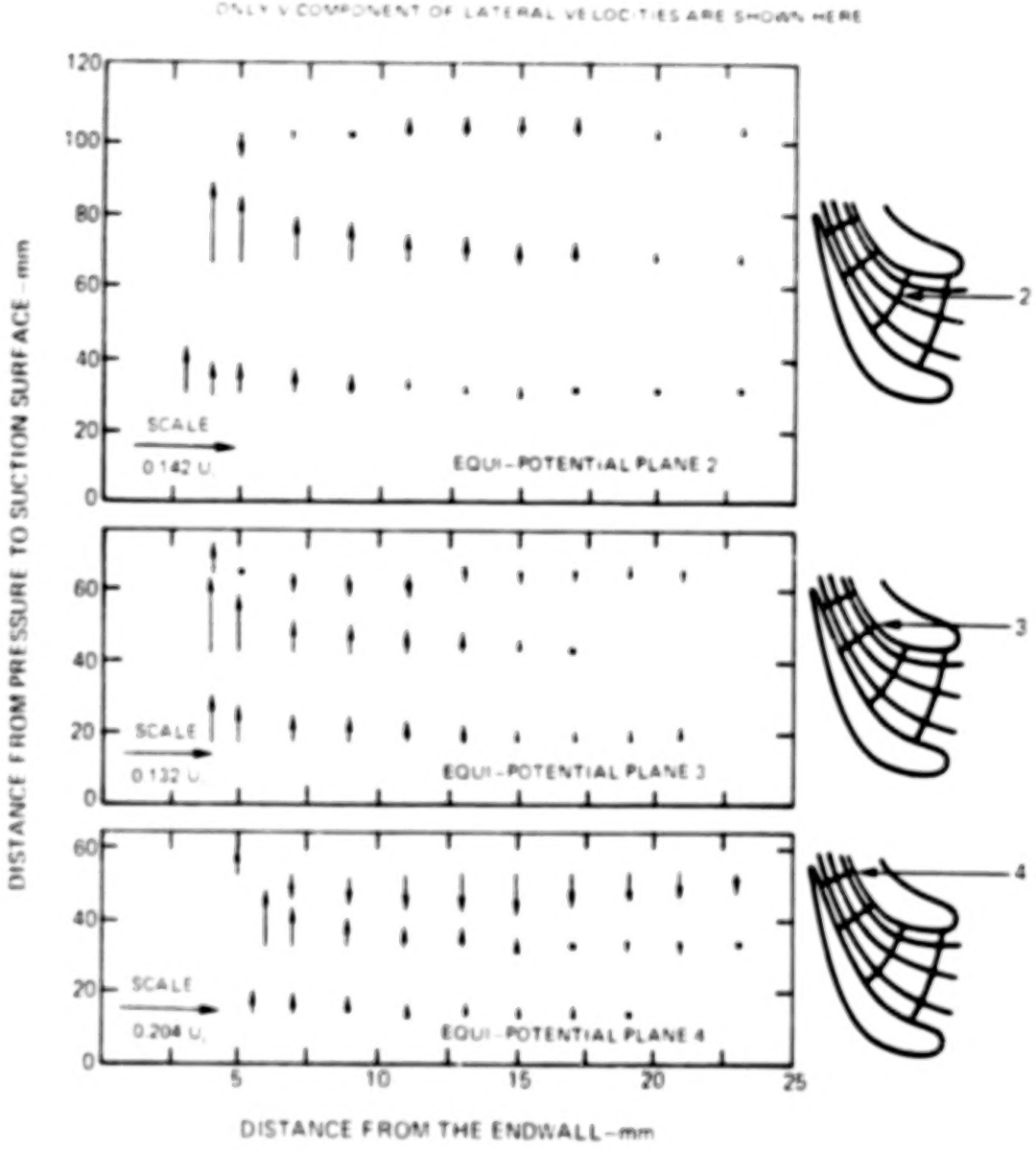

FIGURE 40 – LATERAL VELOCITY FOR DIFFERENT PLANES FLOW CONDITION C

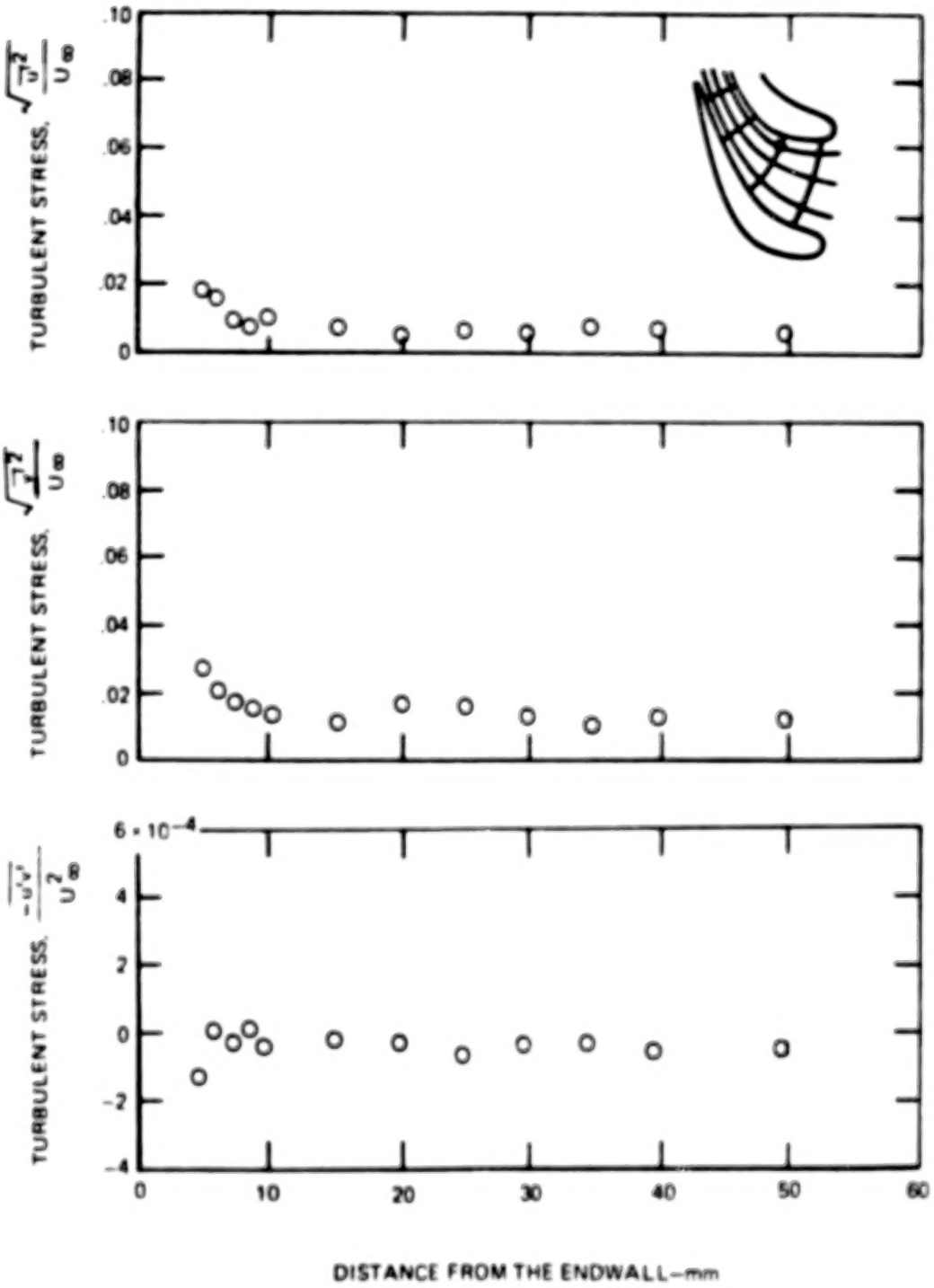

FIGURE 41—TURBULENT STRESS VS. DISTANCE FROM THE ENDWALL POSITION 4, FLOW CONDITION C

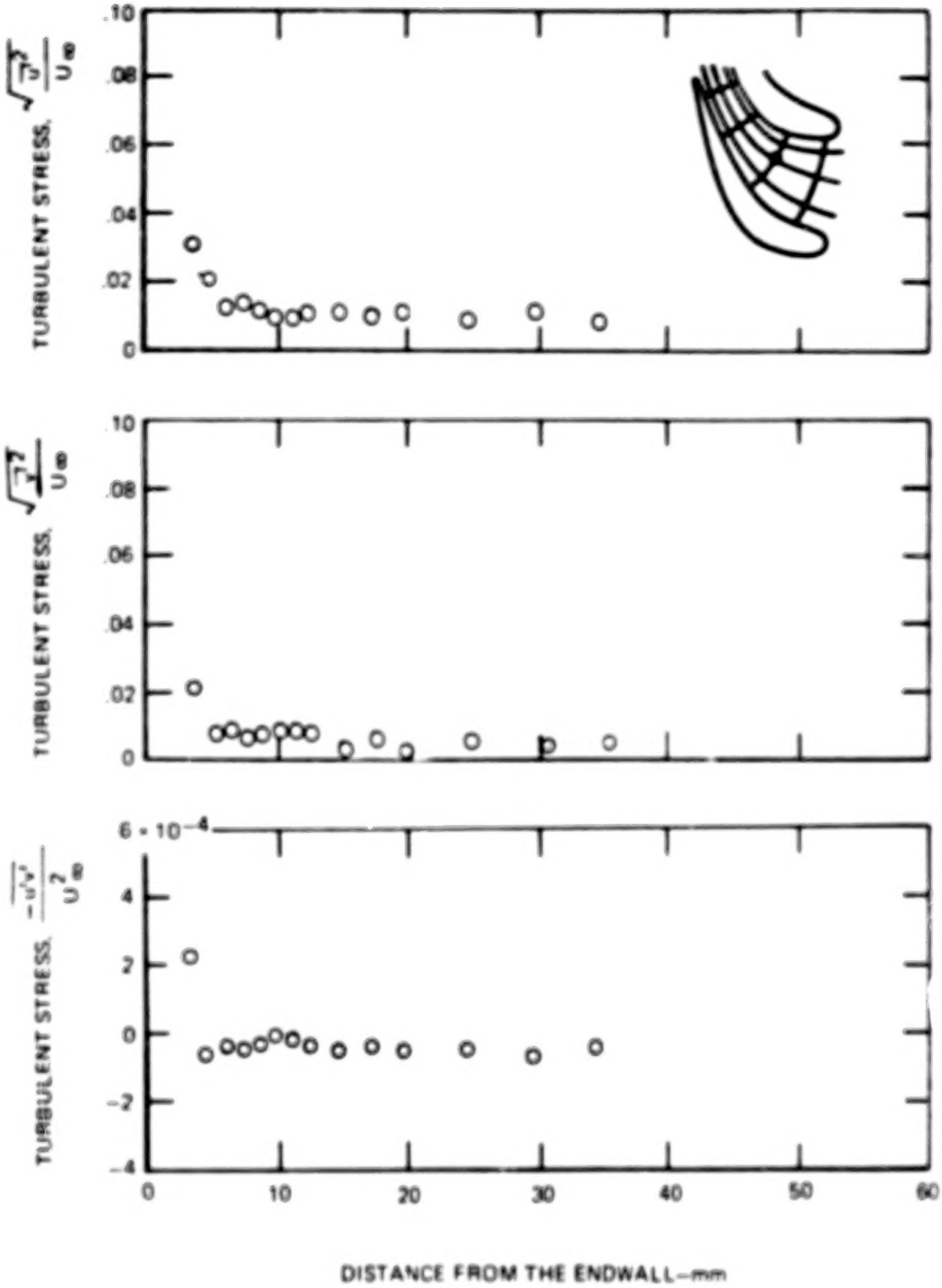

FIGURE 42 – TURBULENT STRESS VS. DISTANCE FROM THE ENDWALL POSITION 5, FLOW CONDITION C

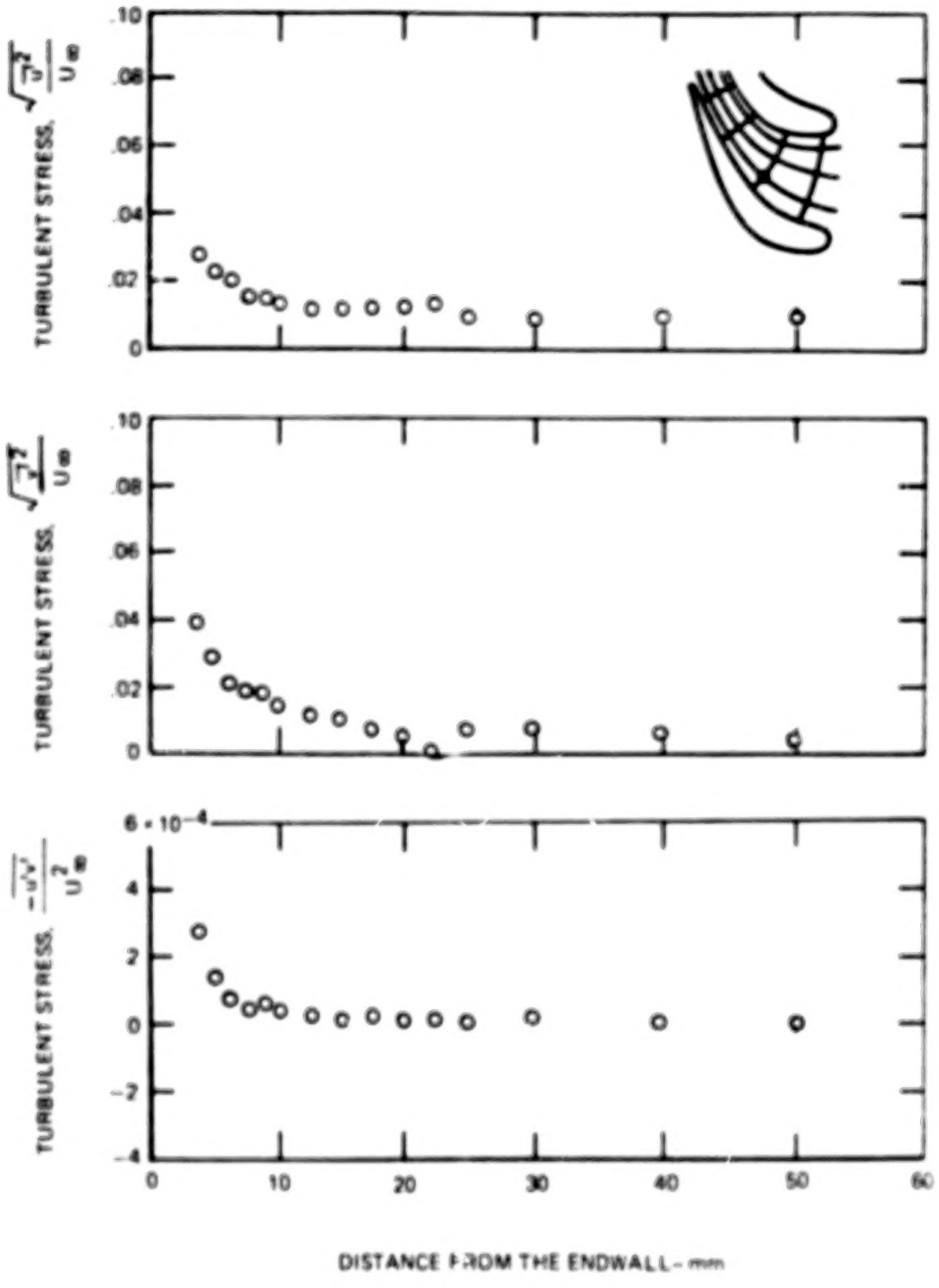

FIGURE 43 – TURBULENT STRESS VS. DISTANCE FROM THE ENDWALL POSITION 6, FLOW CONDITION C

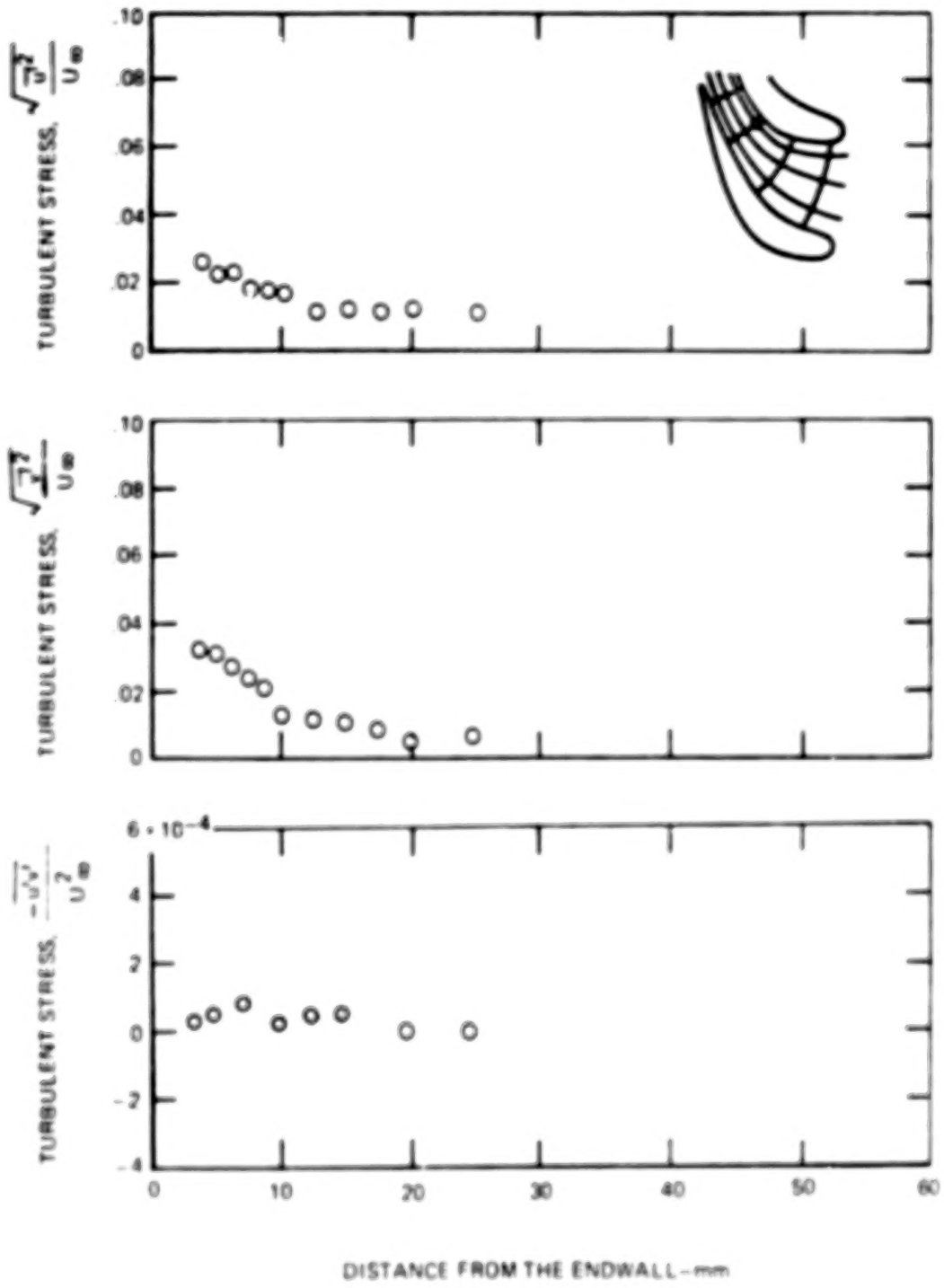

FIGURE 44 – TURBULENT STRESS VS. DISTANCE FROM THE ENDWALL POSITION 7, FLOW CONDITION C

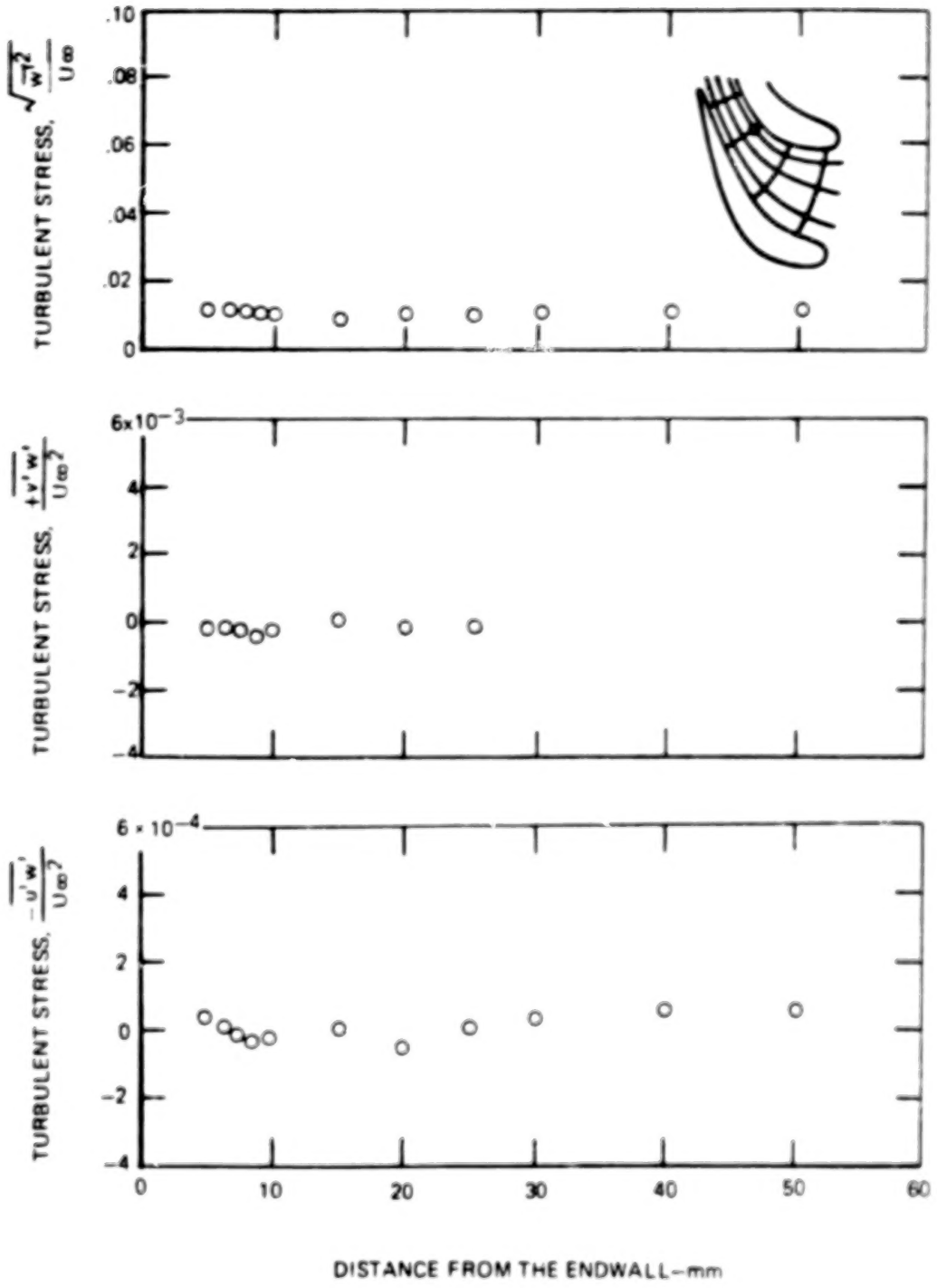

FIGURE 45–TURBULENT STRESS VS. DISTANCE FROM THE ENDWALL POSITION 7, FLOW CONDITION C

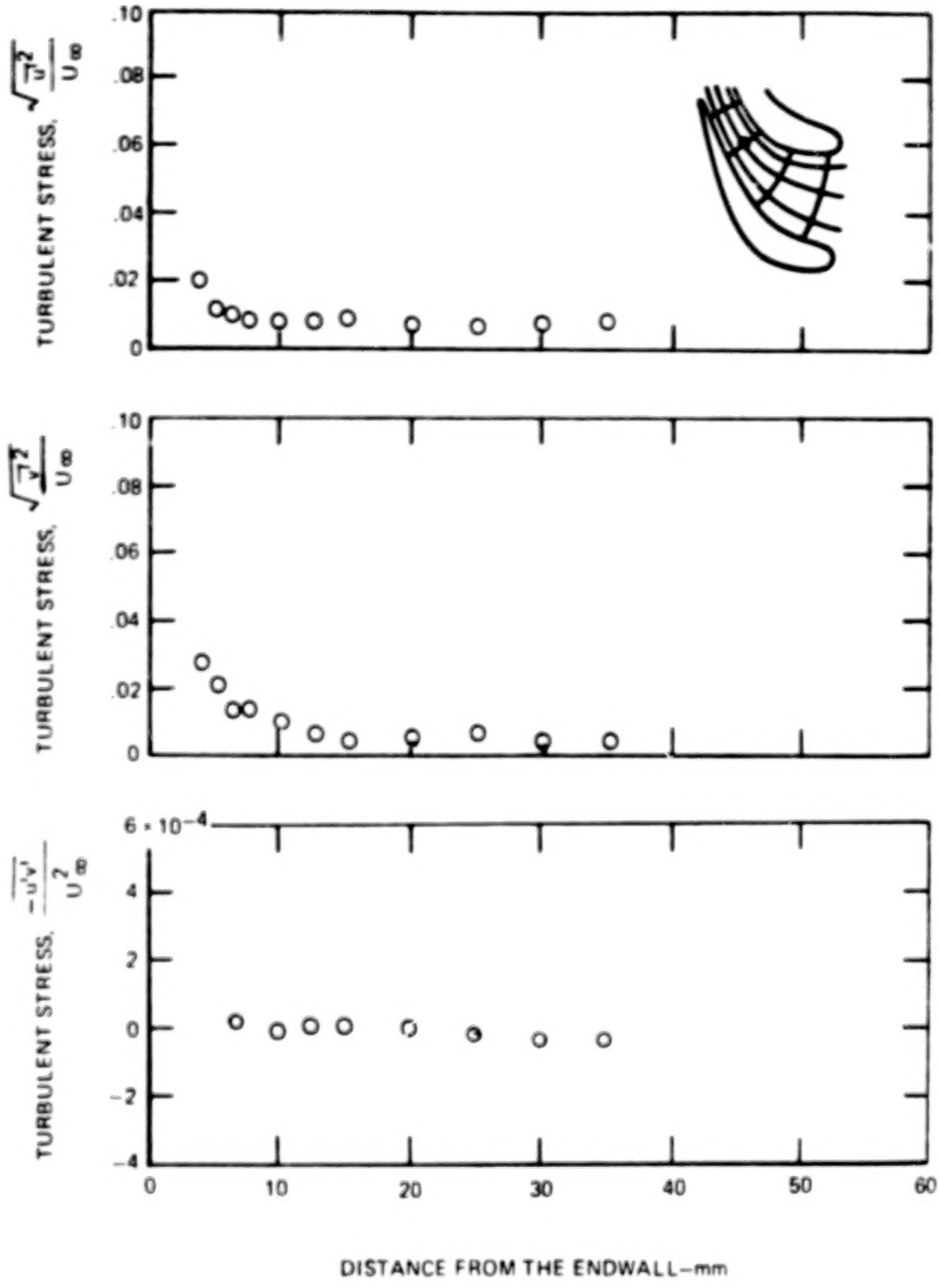

FIGURE 46 – TURBULENT STRESS VS. DISTANCE FROM THE ENDWALL POSITION 8 , FLOW CONDITION C

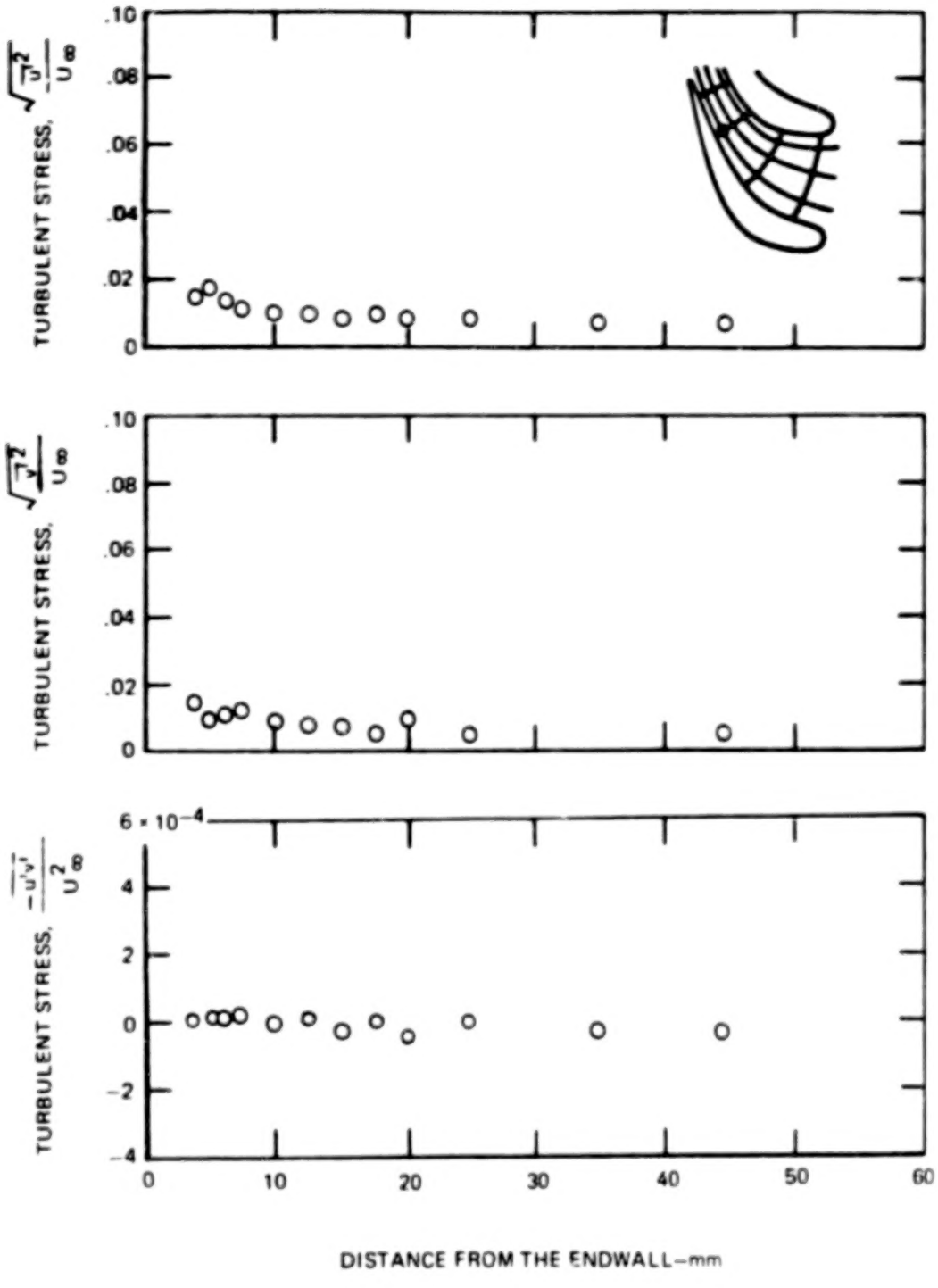

FIGURE 47–TURBULENT STRESS VS. DISTANCE FROM THE ENDWALL POSITION 9 , FLOW CONDITION C

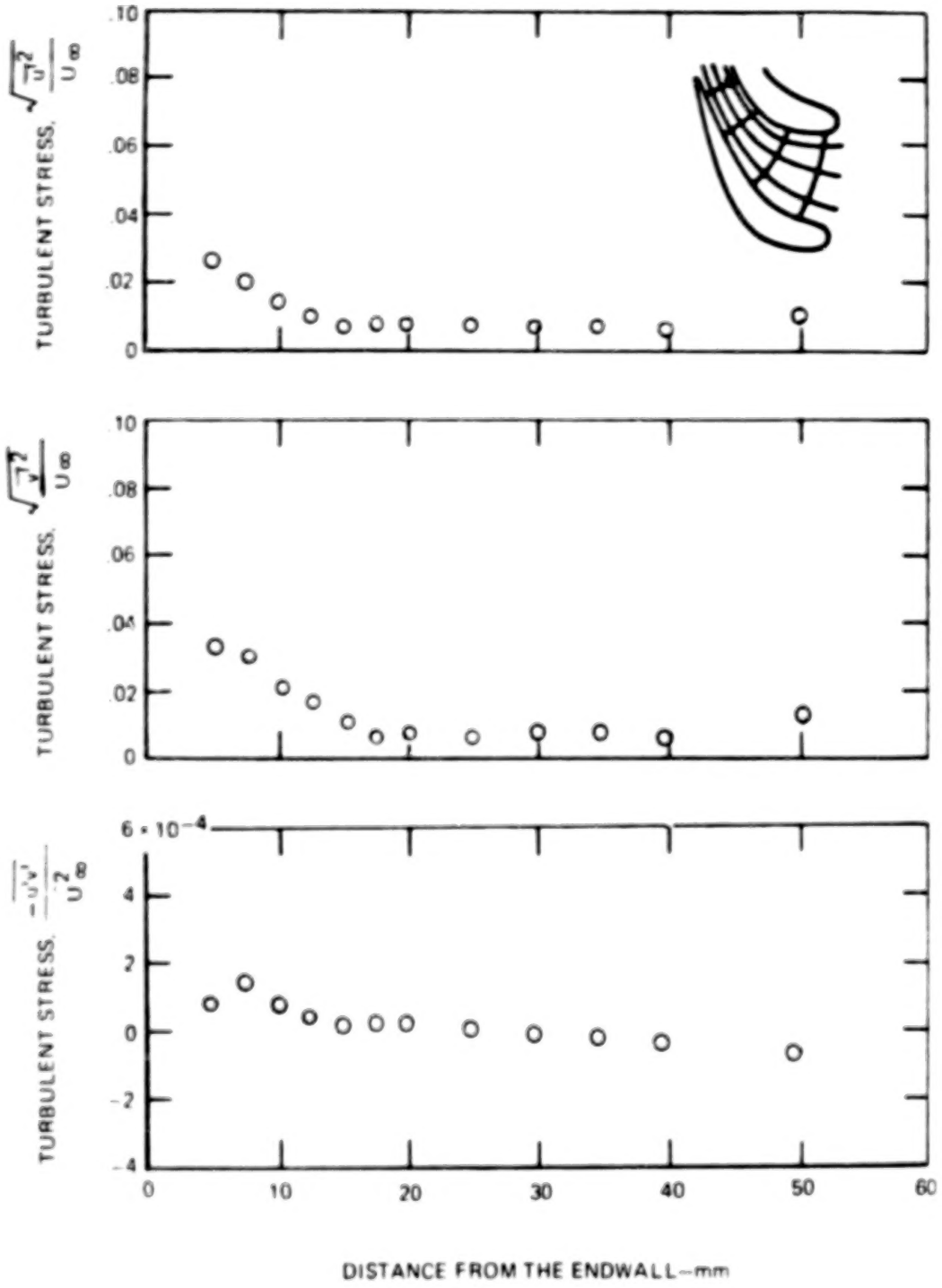

FIGURE 48 – TURBULENT STRESS VS. DISTANCE FROM THE ENDWALL POSITION 10, FLOW CONDITION C

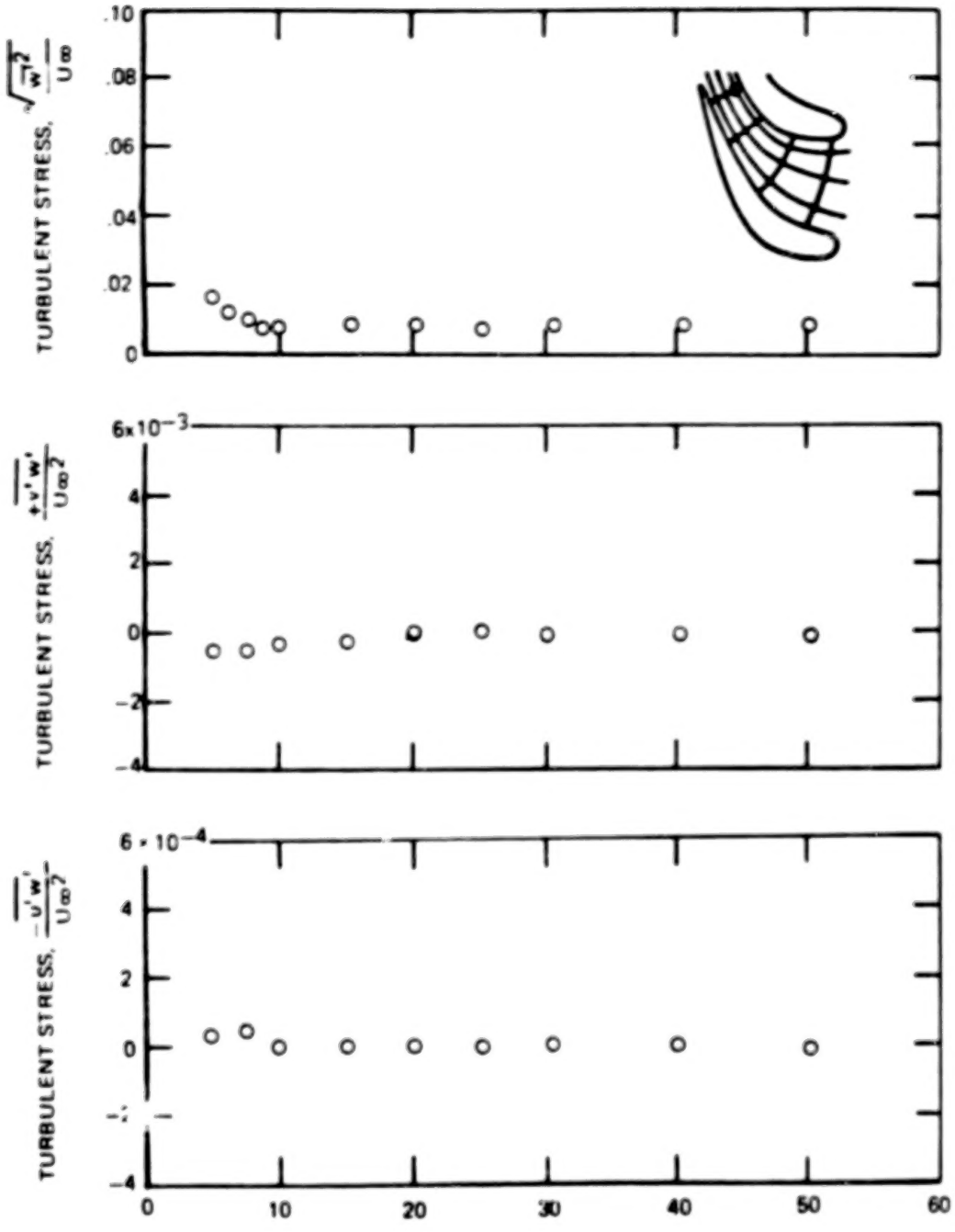

FIGURE 49—TURBULENT STRESS VS. DISTANCE FROM THE ENDWALL POSITION 10, FLOW CONDITION C

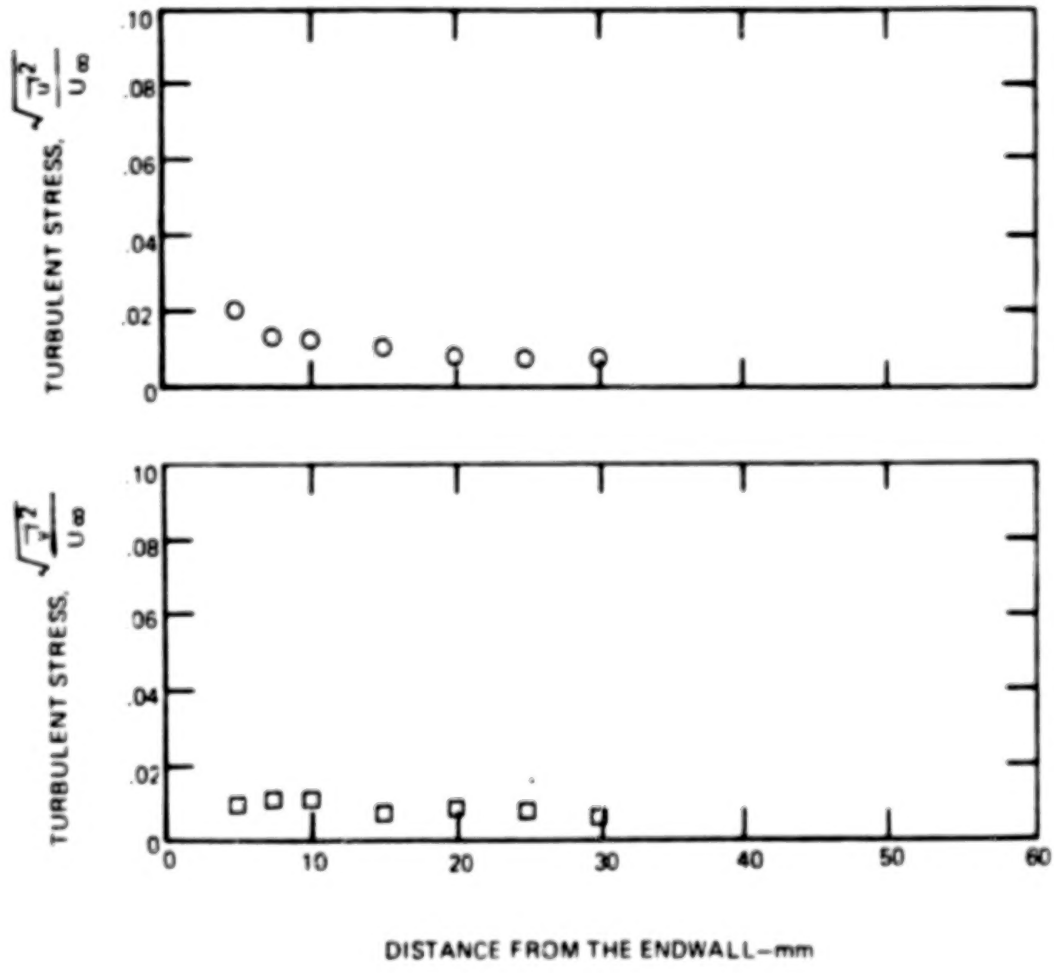

FIGURE 50–TURBULENT STRESS VS. DISTANCE FROM THE ENDWALL POSITION 11, FLOW CONDITION C

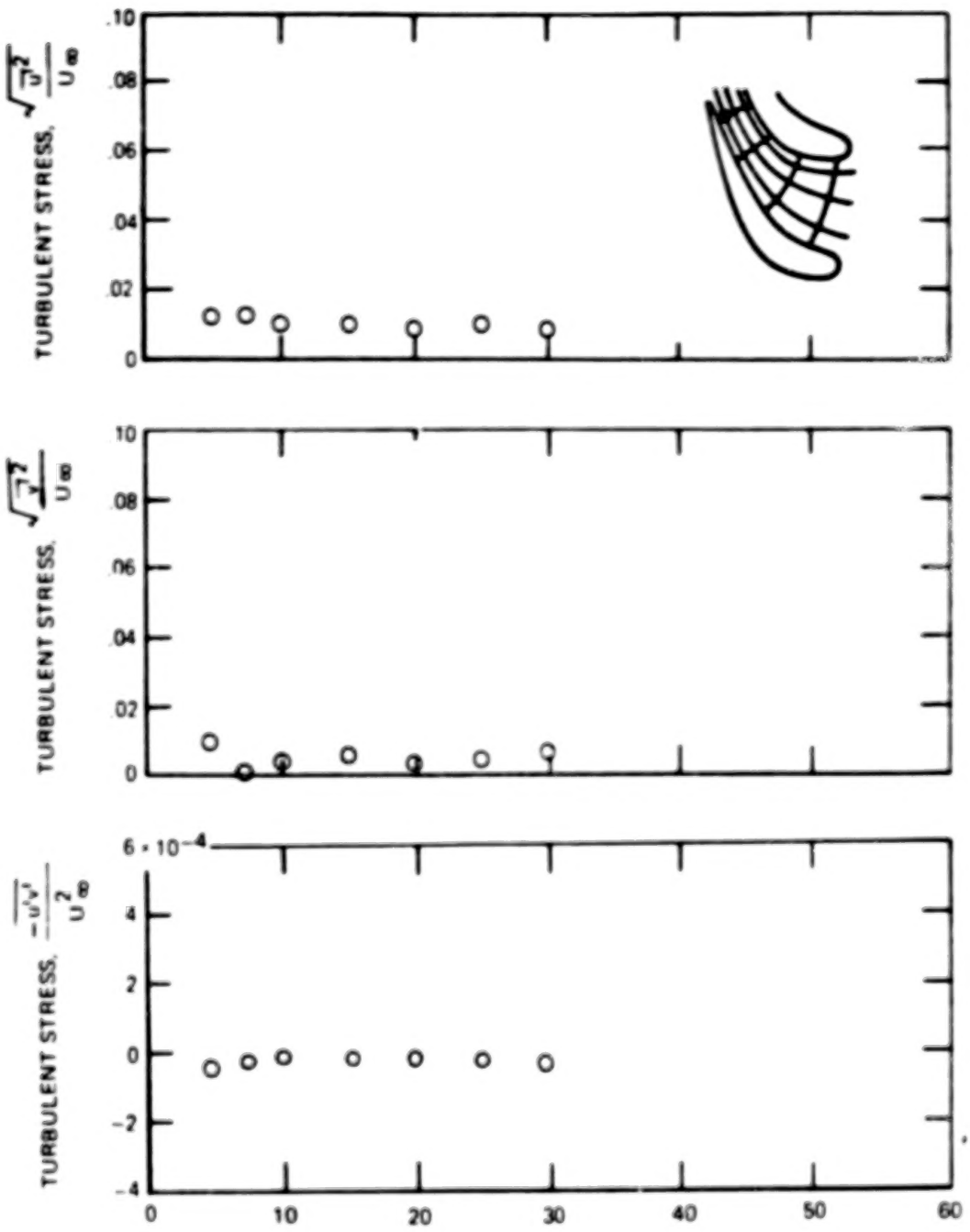

FIGURE 51 – TURBULENT STRESS VS. DISTANCE FROM THE ENDWALL POSITION 12, FLOW CONDITION C

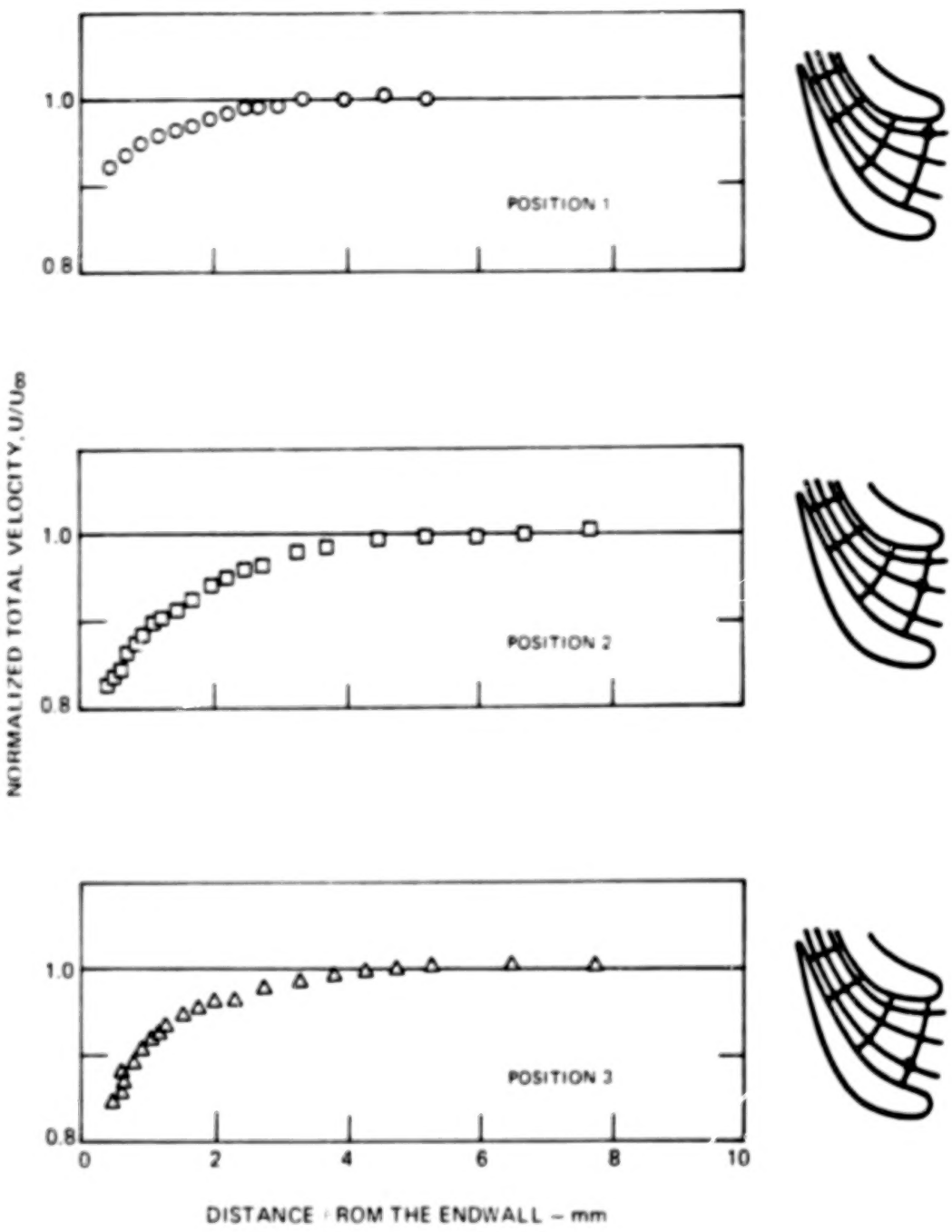

FIGURE 52 – MEAN VELOCITIES VS. DISTANCE FROM THE ENDWALL FLOW CONDITION B

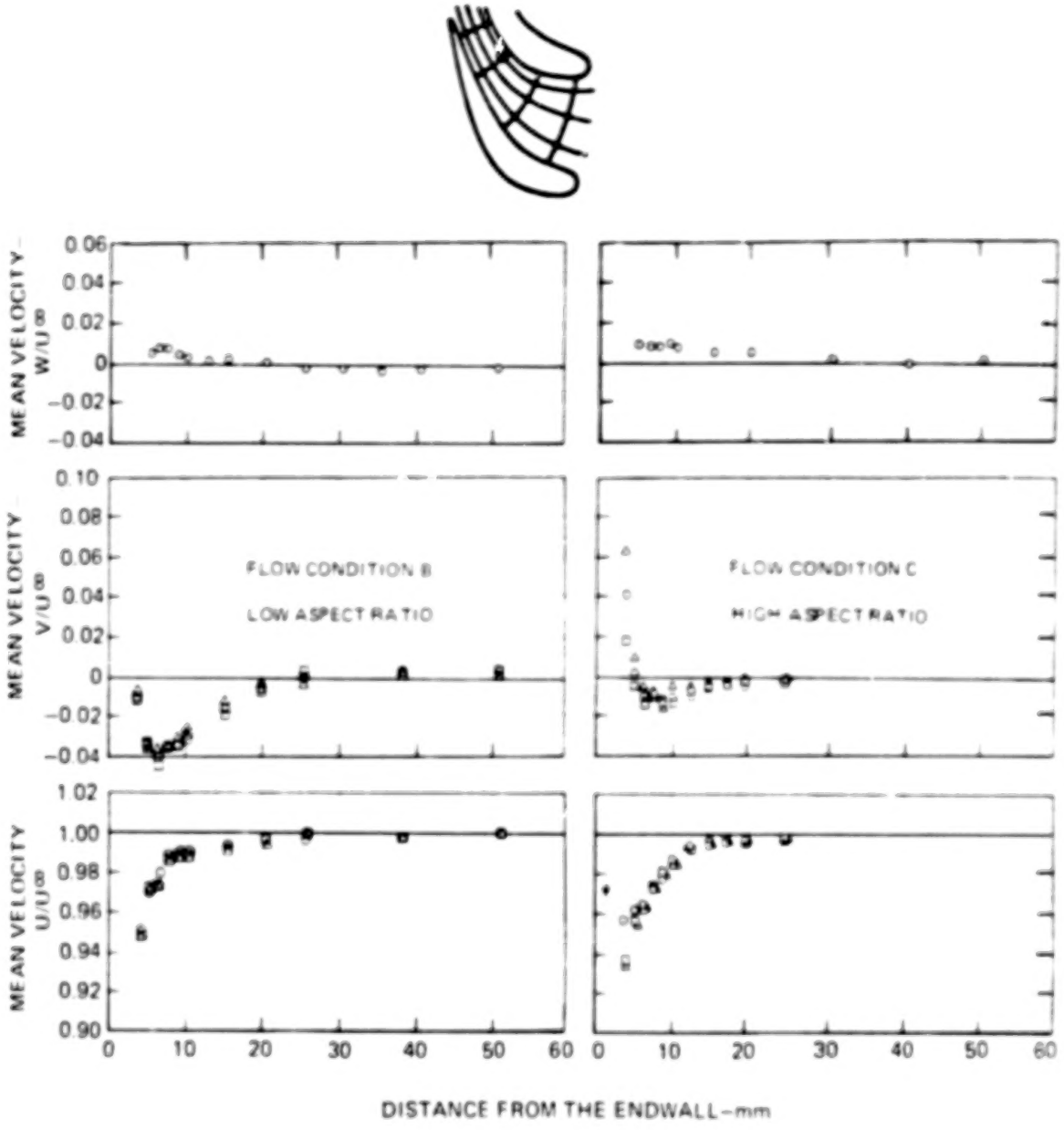

FIGURE 53 – MEAN VELOCITIES VS. DISTANCE FROM THE ENDWALL POSITION 7, FLOW CONDITIONS B AND C

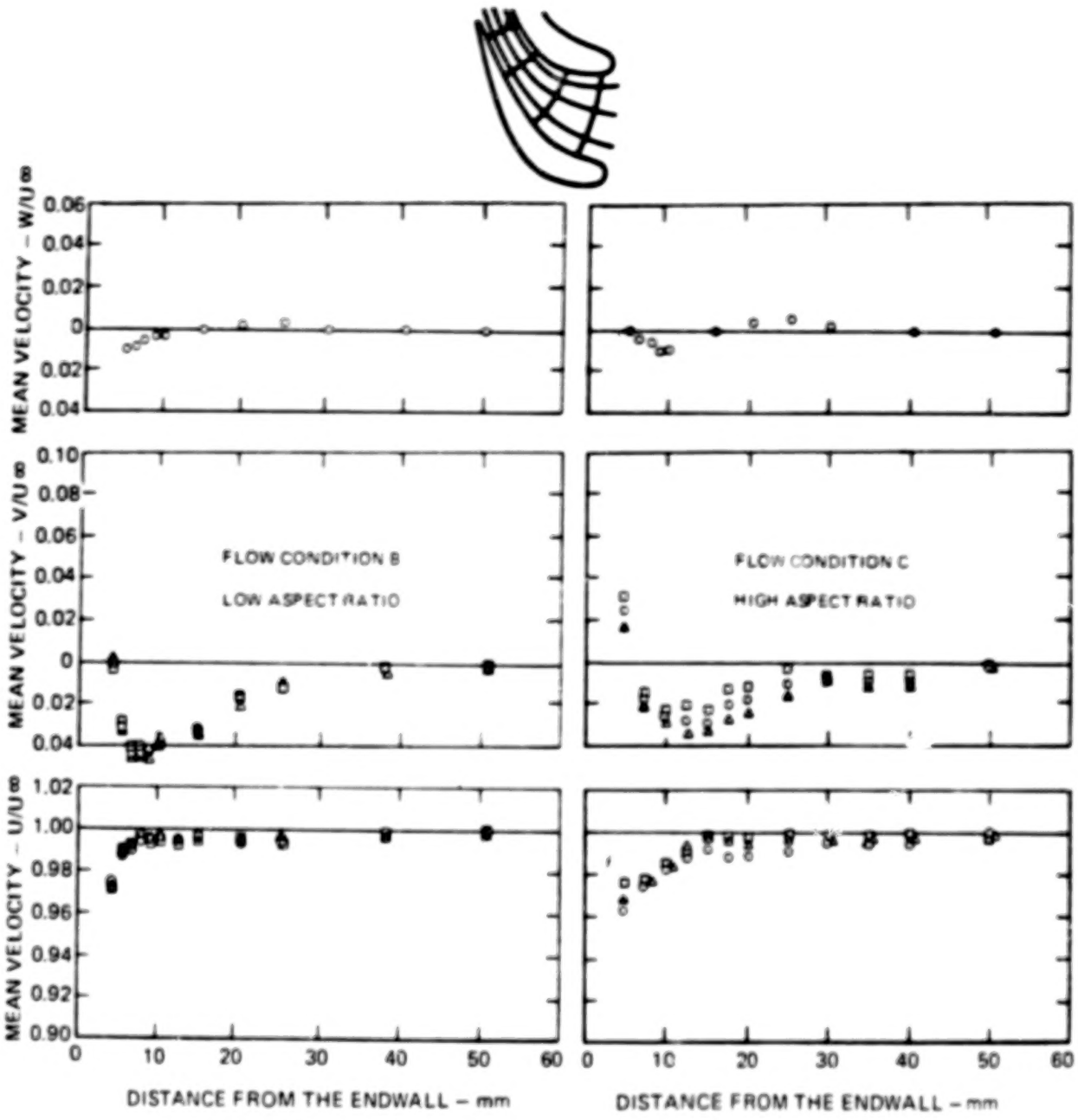

FIGURE 54 – MEAN VELOCITIES VS DISTANCE FROM THE ENDWALL POSITION 10, FLOW CONDITIONS B AND C

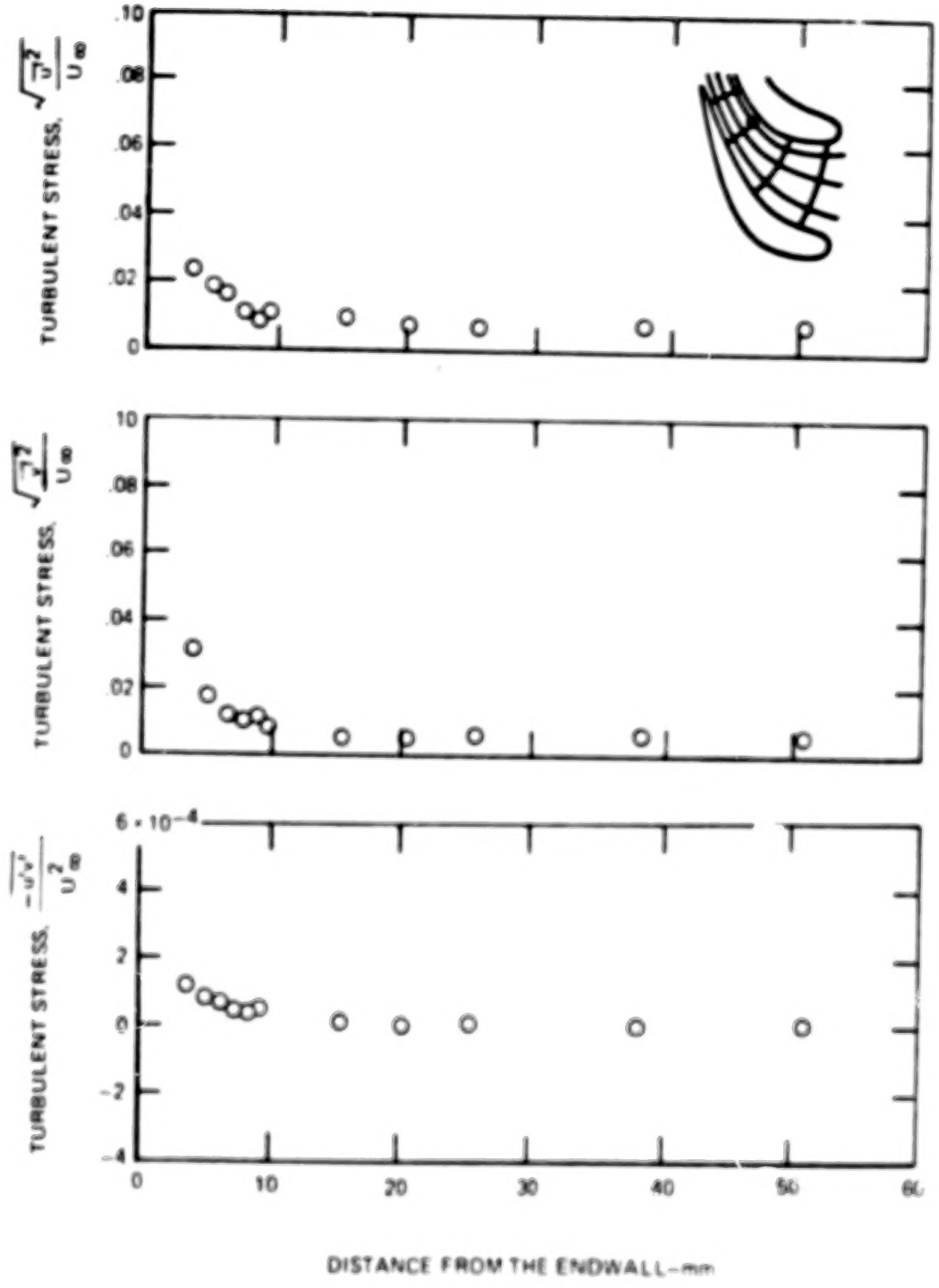

FIGURE 55 – TURBULENT STRESS VS. DISTANCE FROM THE ENDWALL POSITION 7, FLOW CONDITION B

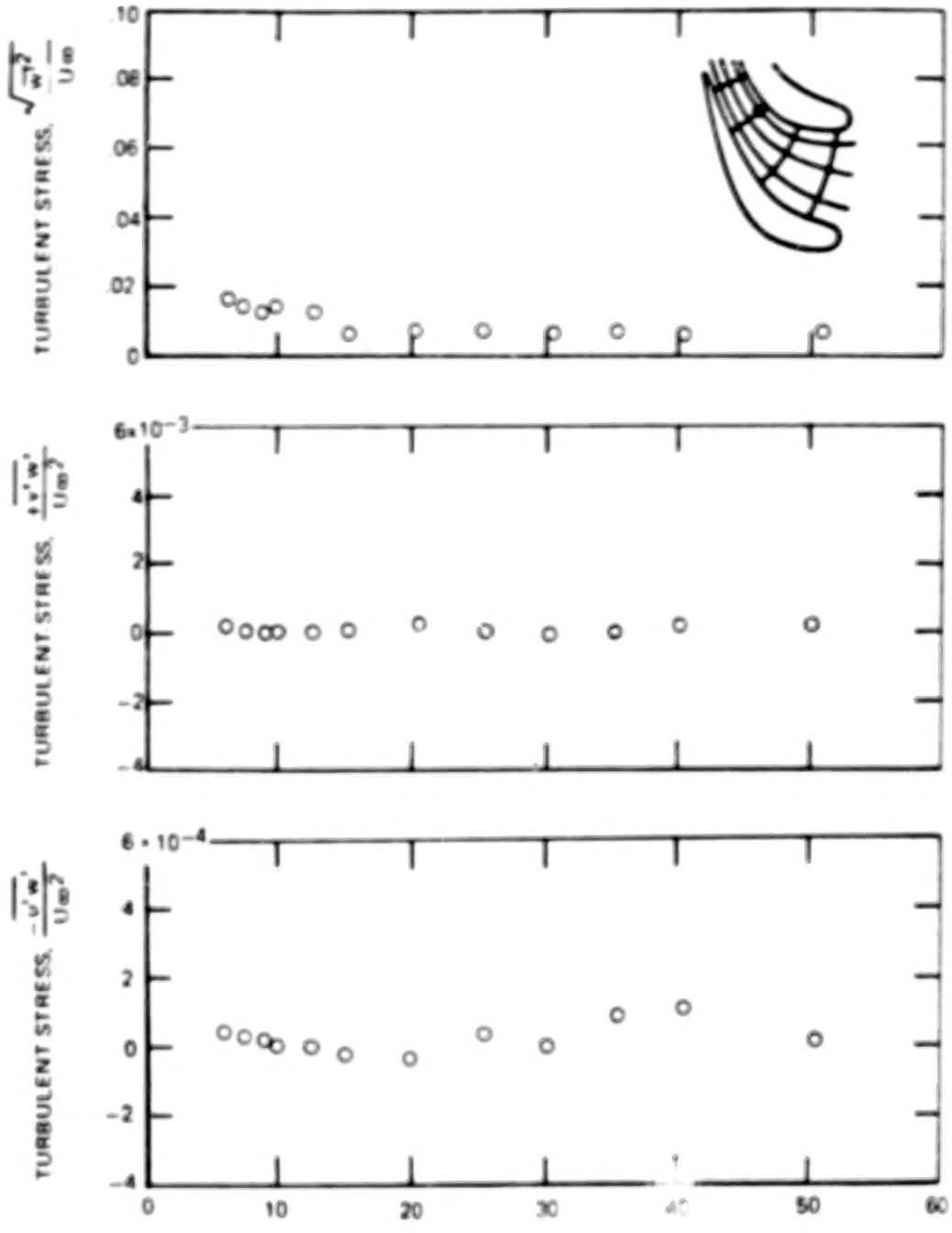

FIGURE 56 – TURBULENT STRESS VS. DISTANCE FROM THE ENDWALL POSITION 7, FLOW CONDITION B

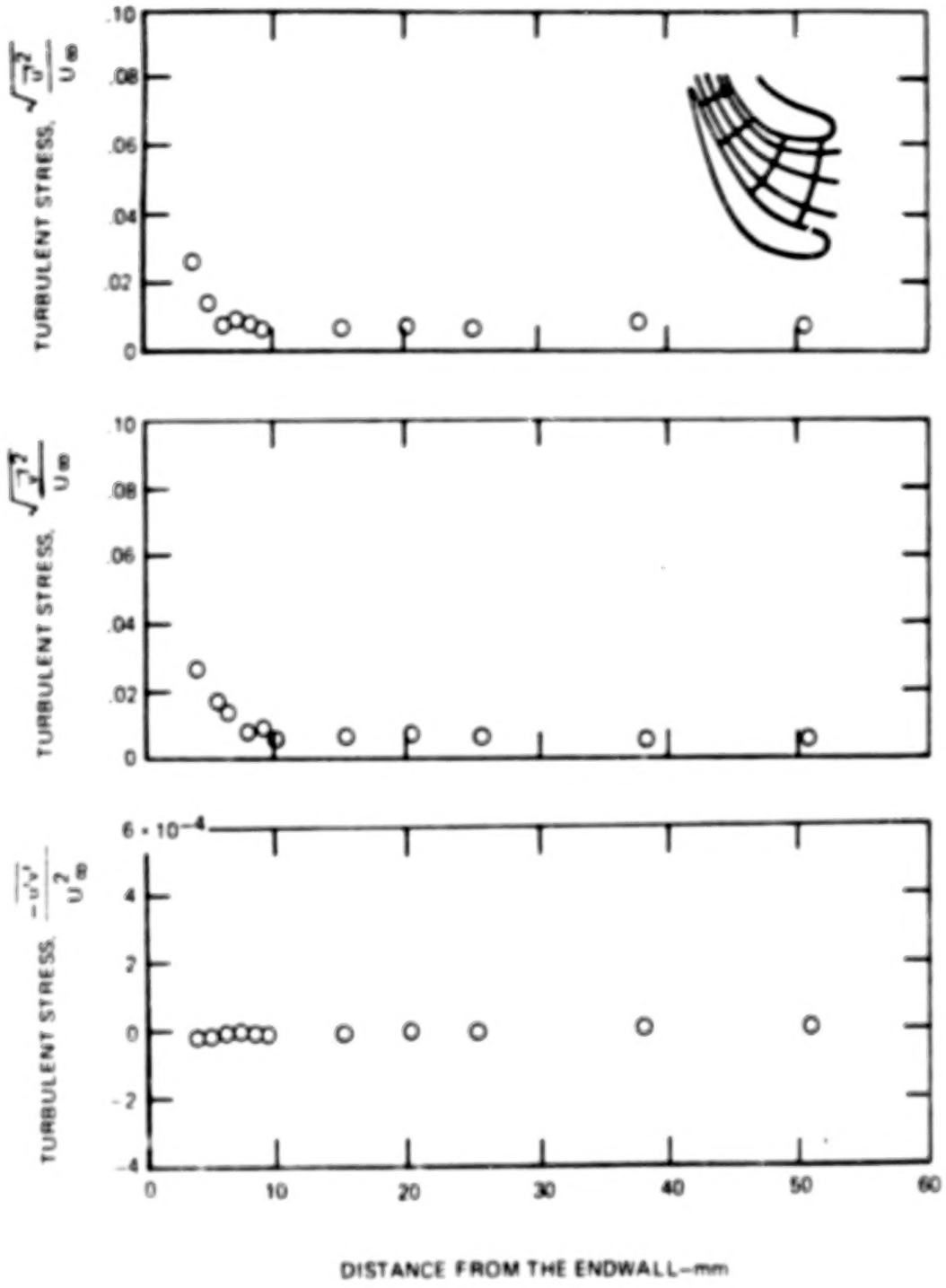

FIGURE 57 – TURBULENT STRESS VS. DISTANCE FROM THE ENDWALL POSITION 10, FLOW CONDITION B

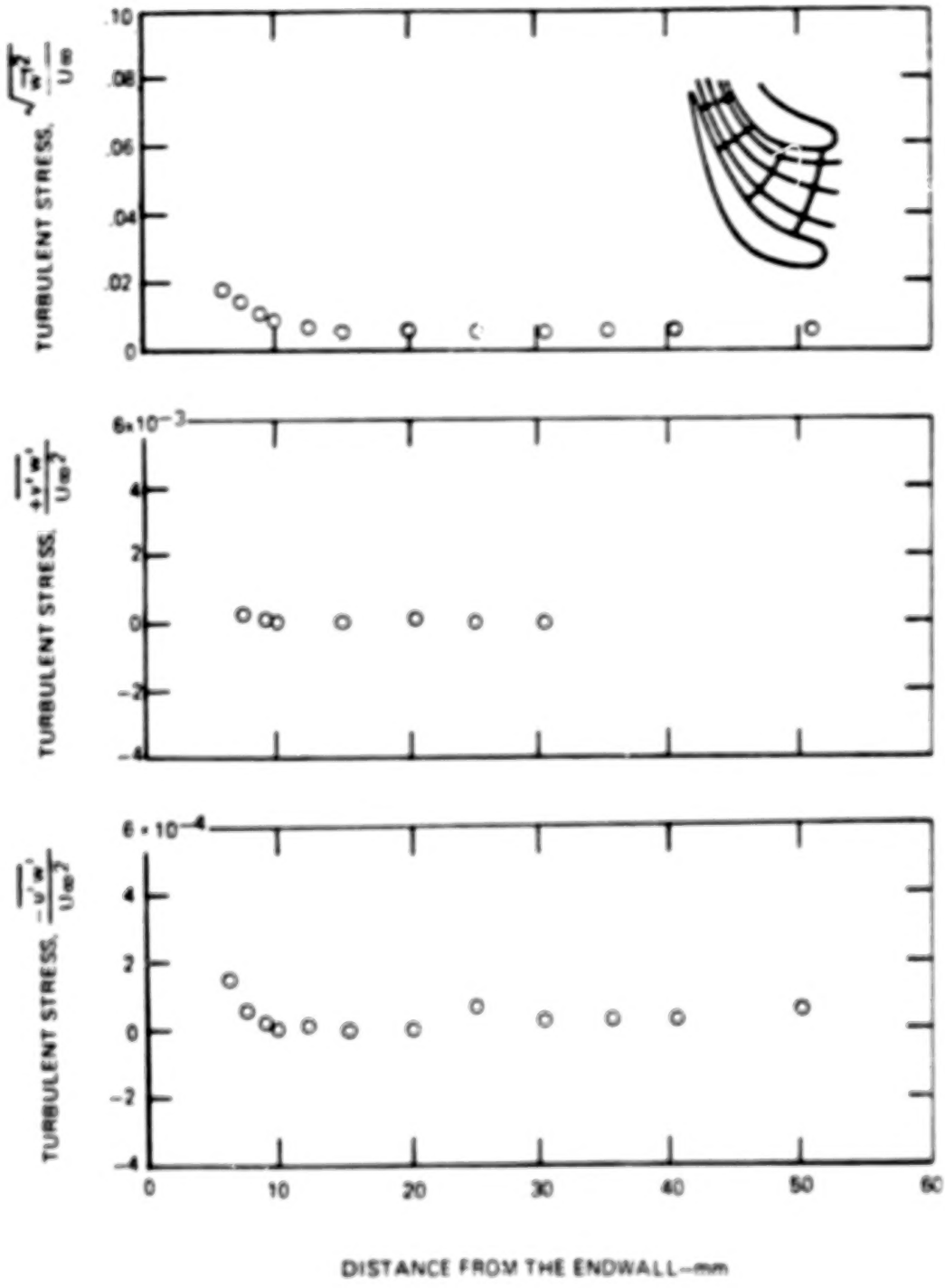

FIGURE 58—TURBULENT STRESS VS. DISTANCE FROM THE ENDWALL POSITION 10, FLOW CONDITION B

TABLE OF CONTENTS

	Page	
SUMMARY	1	1/A5
INTRODUCTION	2	1/A6
DESCRIPTION OF THE EXPERIMENT	5	1/A9
Wind Tunnel	5	1/A9
Test Section	7	1/A11
Test Conditions	8	1/A12
Measurements Obtained	9	1/A13
Instrumentation	10	1/A14
RESULTS AND DISCUSSION	17	1/B7
Flow Condition "A"	17	1/B7
Flow Condition "C"	23	1/B13
Flow Conditions "B"	25	1/C1
CONCLUSIONS	27	1/C3
FIGURES	28	1/C4
APPENDIX A - Mean-Velocity Data	90	2/A3
APPENDIX B - Additional Inlet-Flow Measurements	110	2/B9
APPENDIX C - List of Symbols	115	2/B14
REFERENCES	116	2/C1

APPENDIX A

Mean-Velocity Data

The individual mean velocity measurements for flow conditions "A" and "C" are shown in this appendix. These data were used to construct the plots in figures 15, 16, 39 and 40.

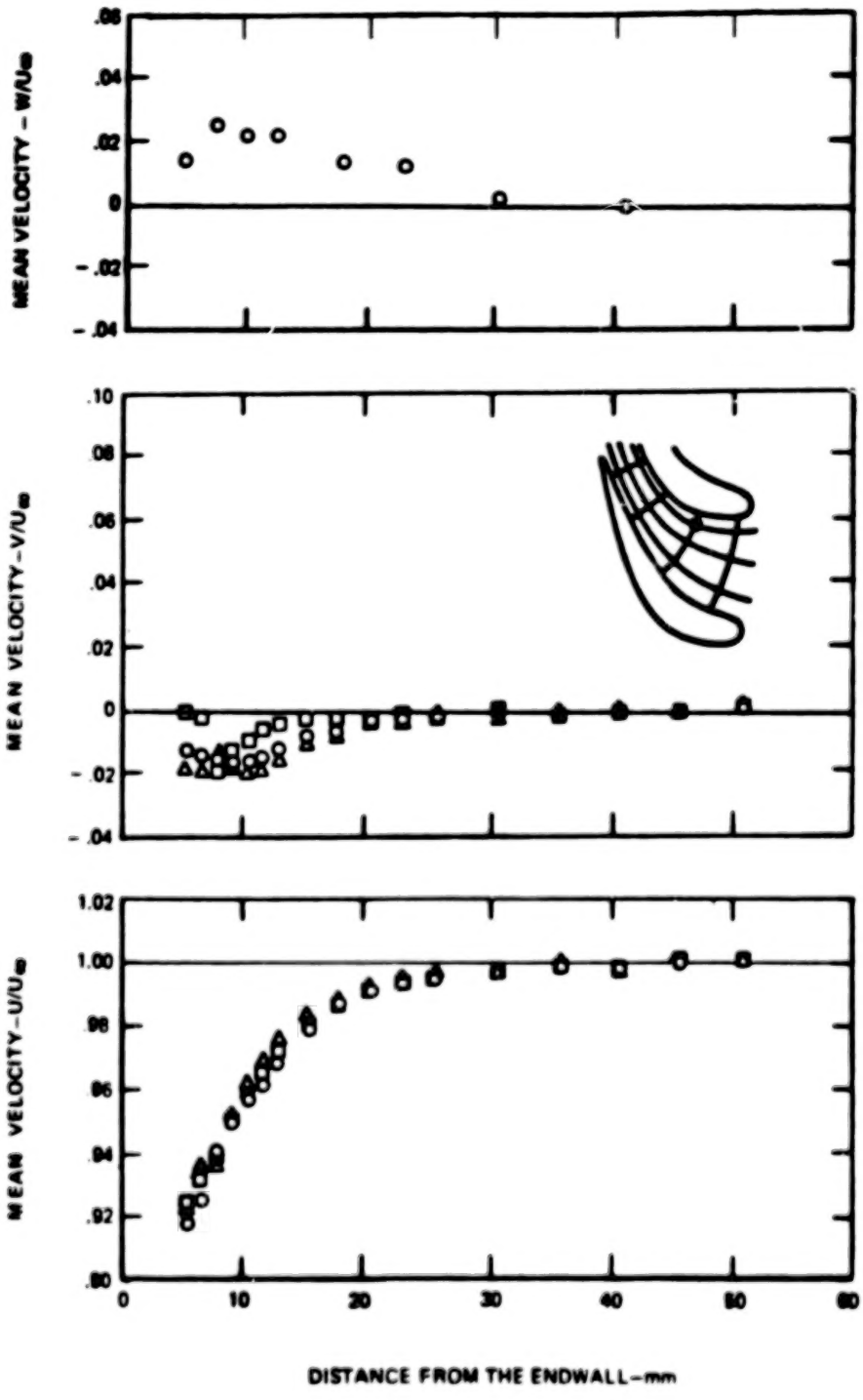

FIGURE A1 –MEAN VELOCITIES VS. DISTANCE FROM THE ENDWALL
POSITION 4, FLOW CONDITION A

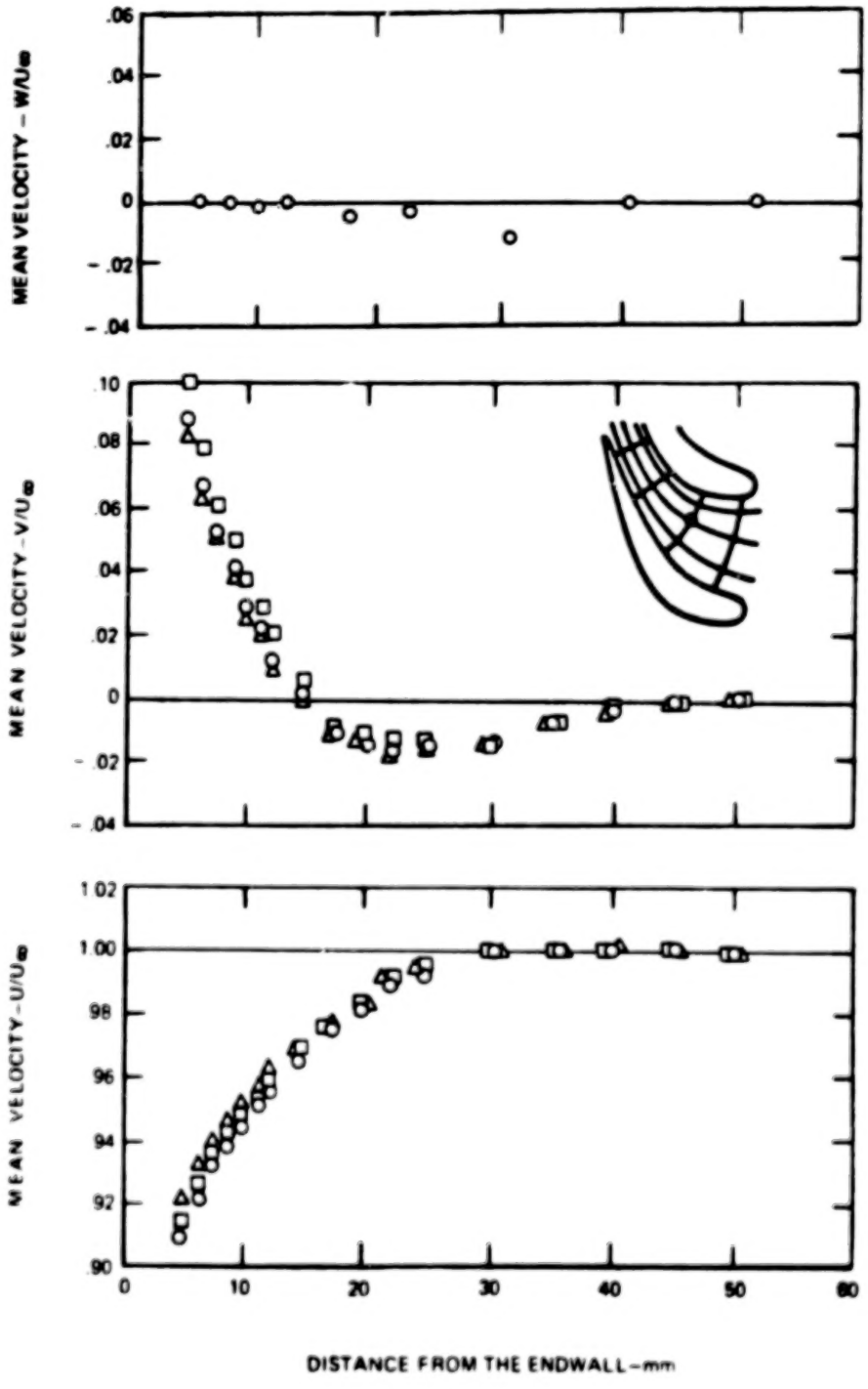

FIGURE A2 – MEAN VELOCITIES VS. DISTANCE FROM THE ENDWALL
POSITION 5, FLOW CONDITION A

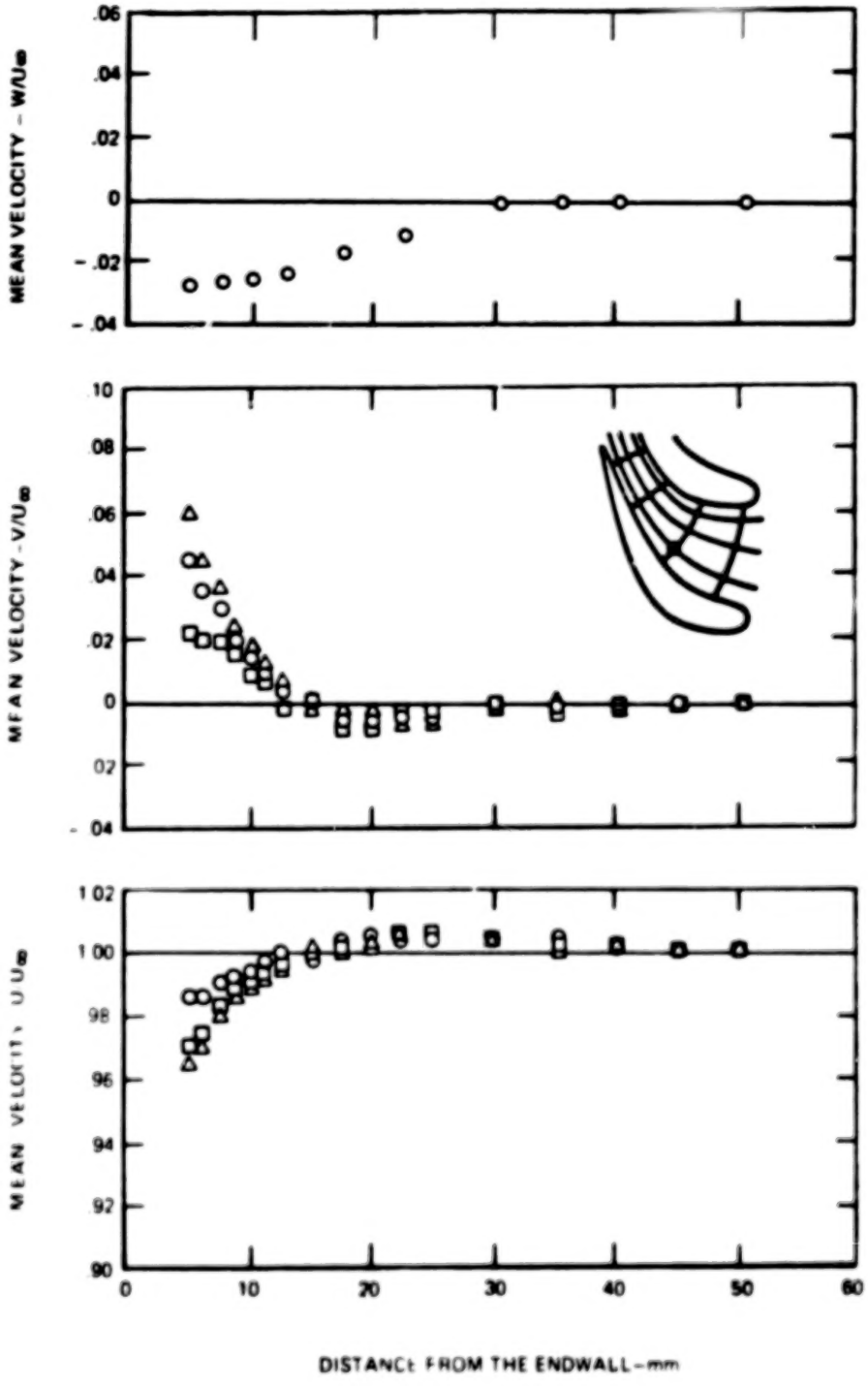

FIGURE A3 – MEAN VELOCITIES VS. DISTANCE FROM THE ENDWALL POSITION 6, FLOW CONDITION A

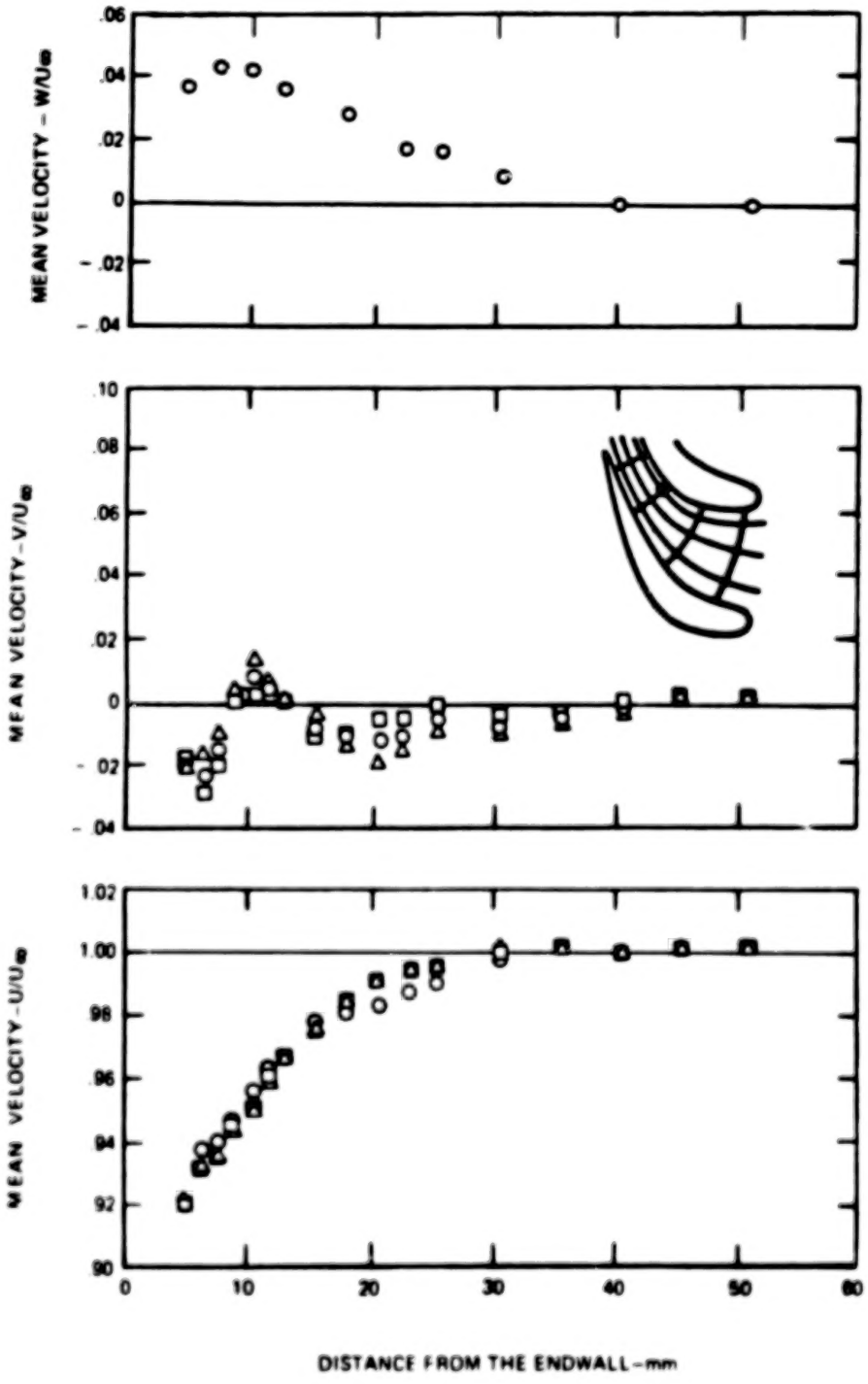

FIGURE A4 – MEAN VELOCITIES VS. DISTANCE FROM THE ENDWALL
POSITION 7, FLOW CONDITION A

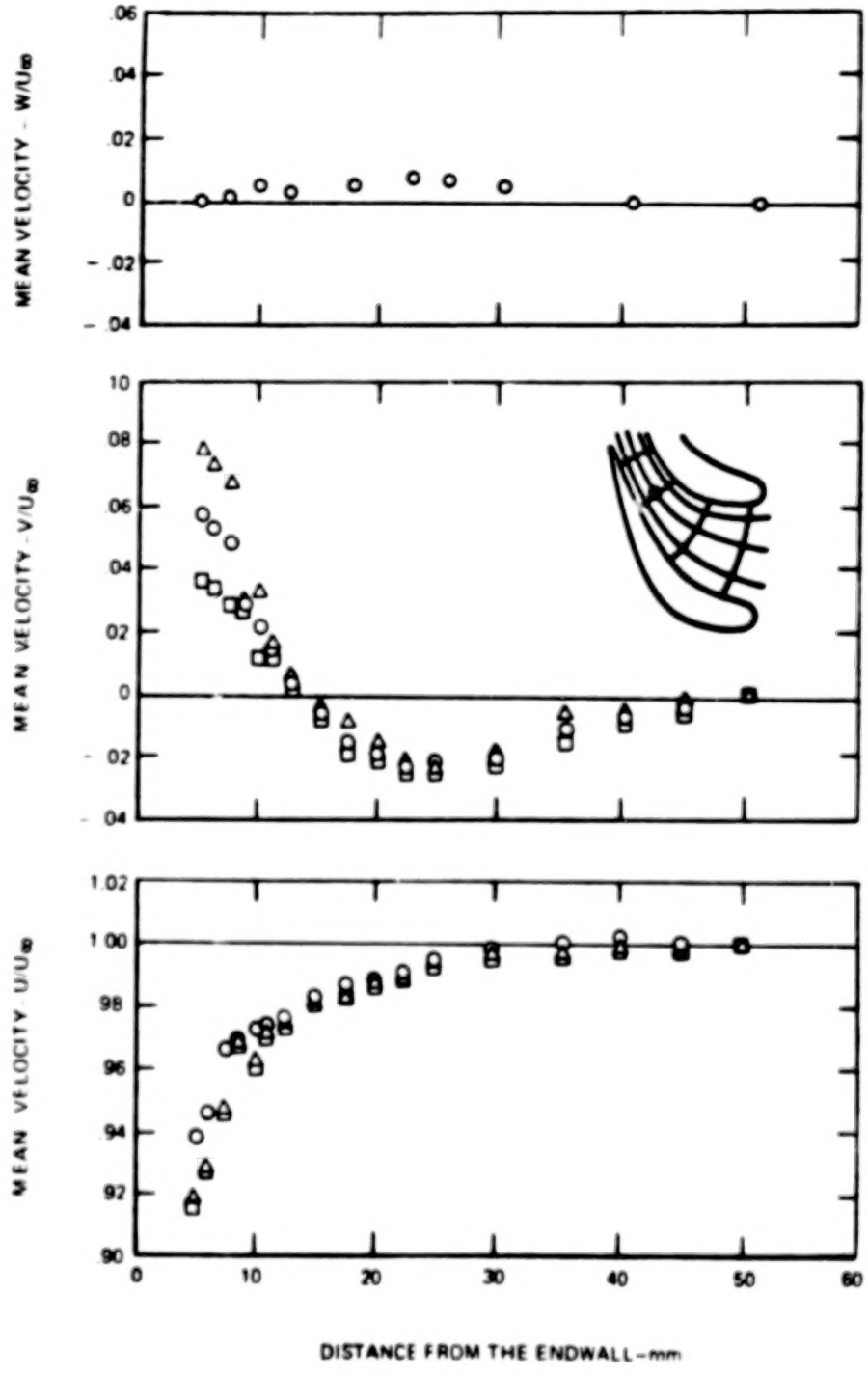

FIGURE A5–MEAN VELOCITIES VS. DISTANCE FROM THE ENDWALL
POSITION 8, FLOW CONDITION A

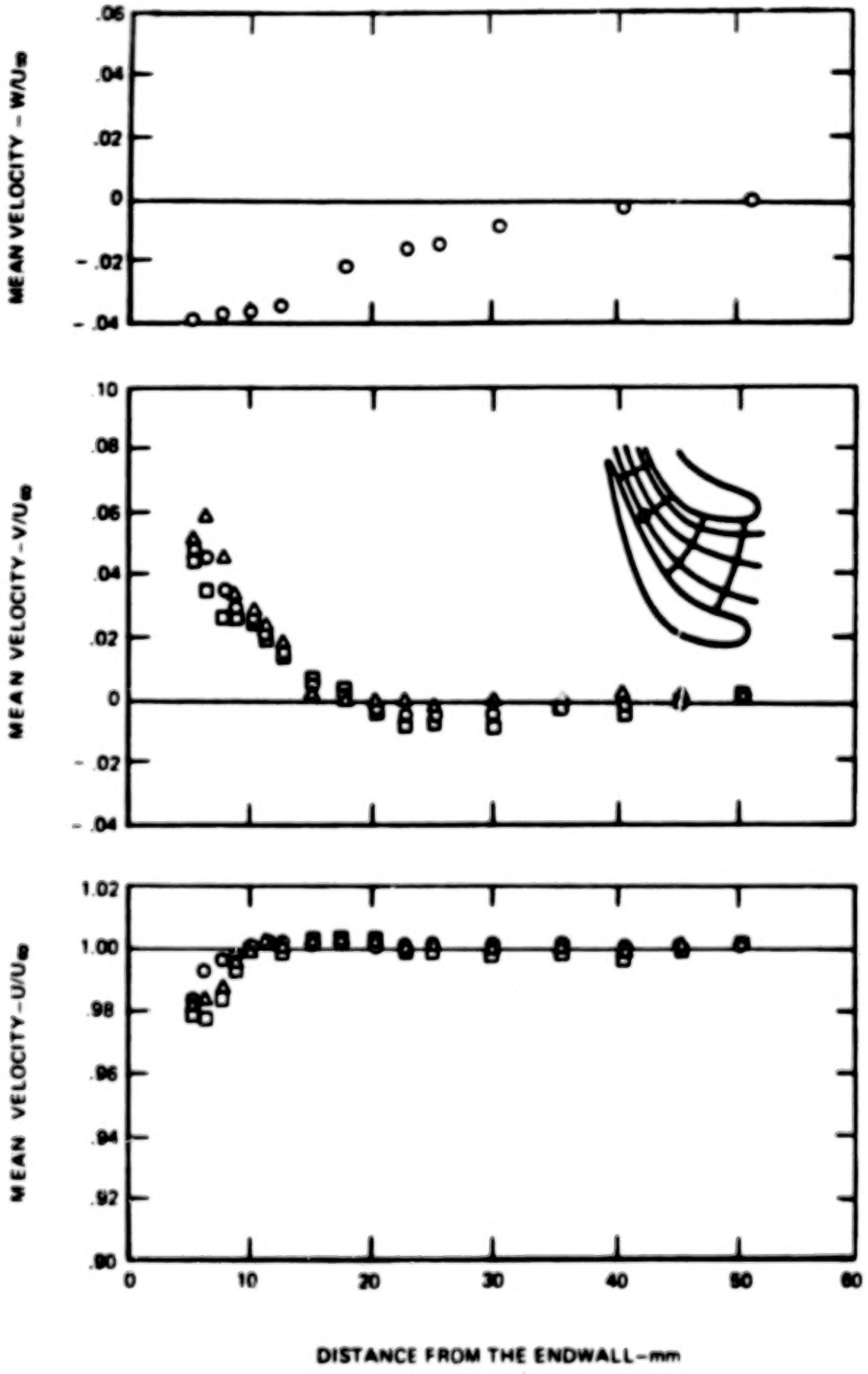

FIGURE A6 – MEAN VELOCITIES VS. DISTANCE FROM THE ENDWALL
POSITION 9, FLOW CONDITION A

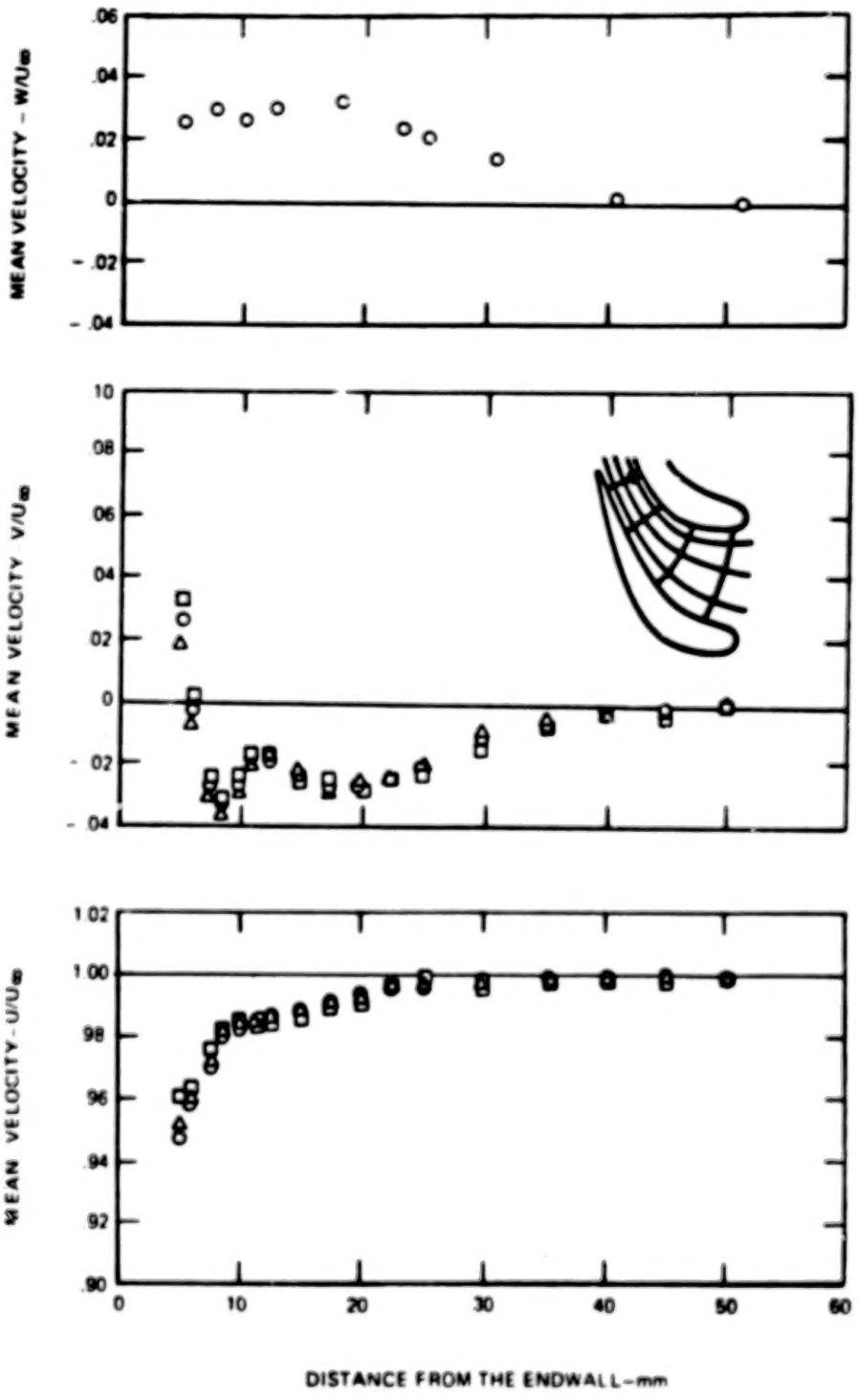

FIGURE A7 – MEAN VELOCITIES VS. DISTANCE FROM THE ENDWALL
POSITION 10, FLOW CONDITION A

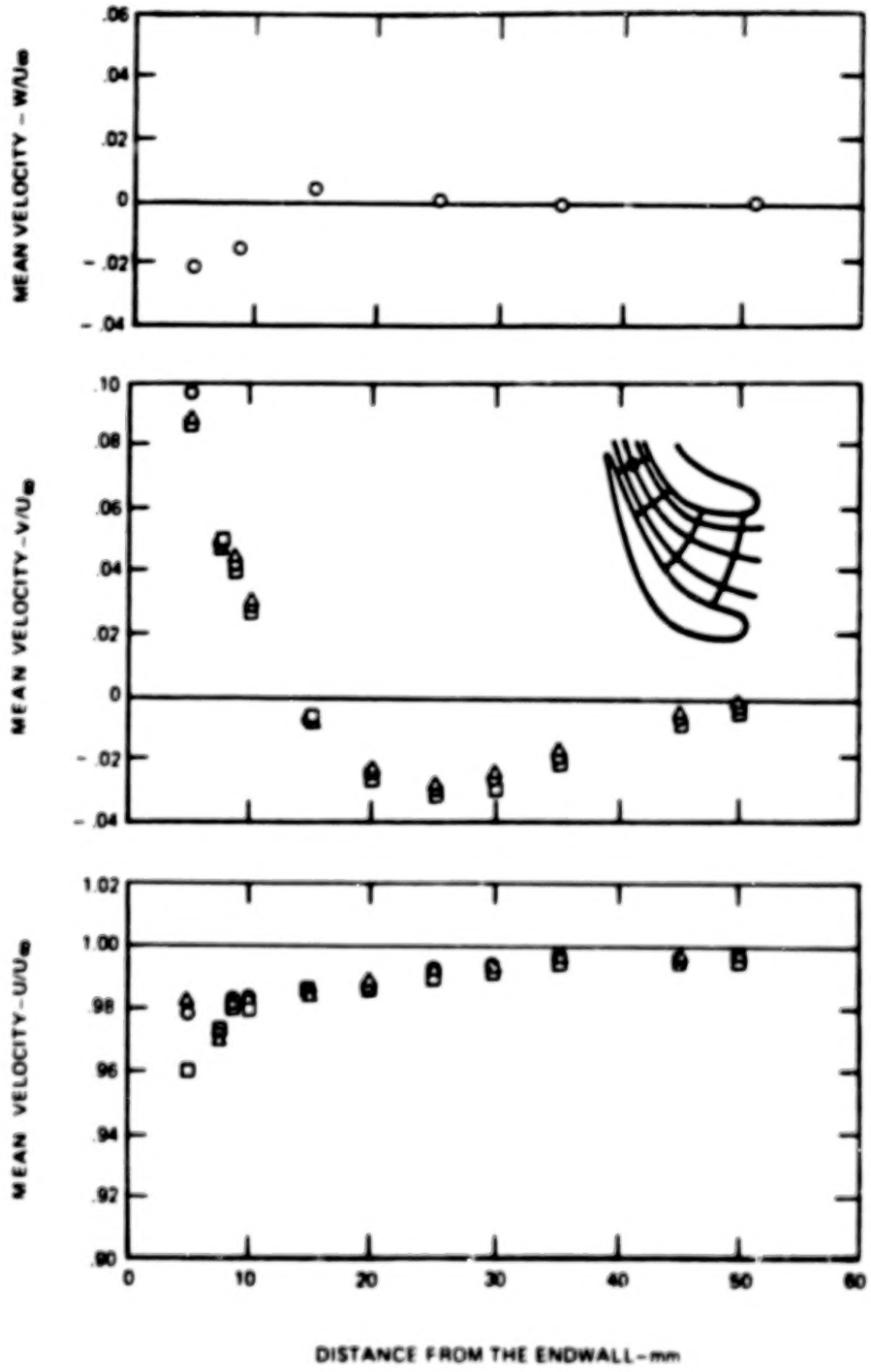

FIGURE A8–MEAN VELOCITIES VS. DISTANCE FROM THE ENDWALL
POSITION 11, FLOW CONDITION A

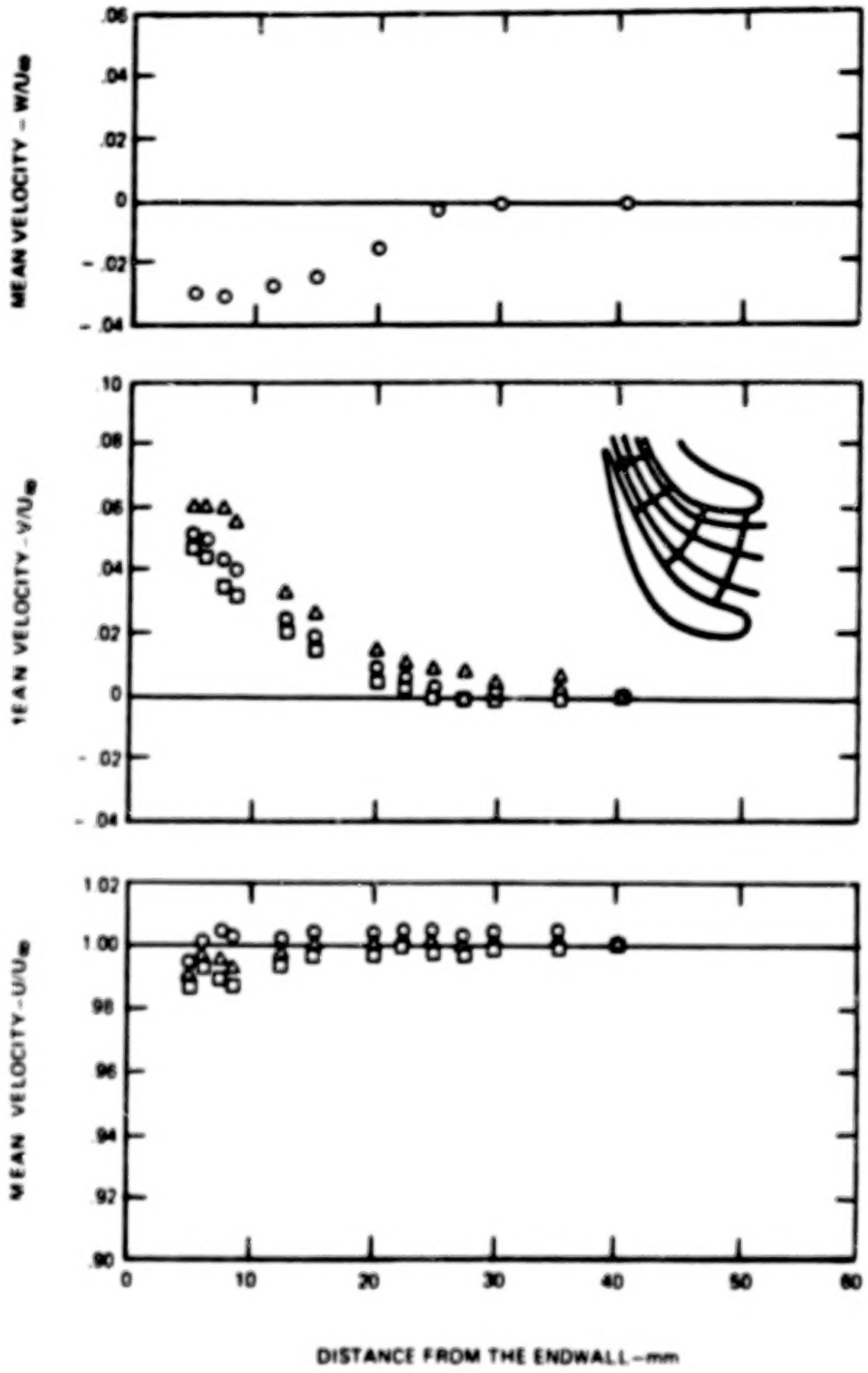

FIGURE A9—MEAN VELOCITIES VS. DISTANCE FROM THE ENDWALL
POSITION 12, FLOW CONDITION A

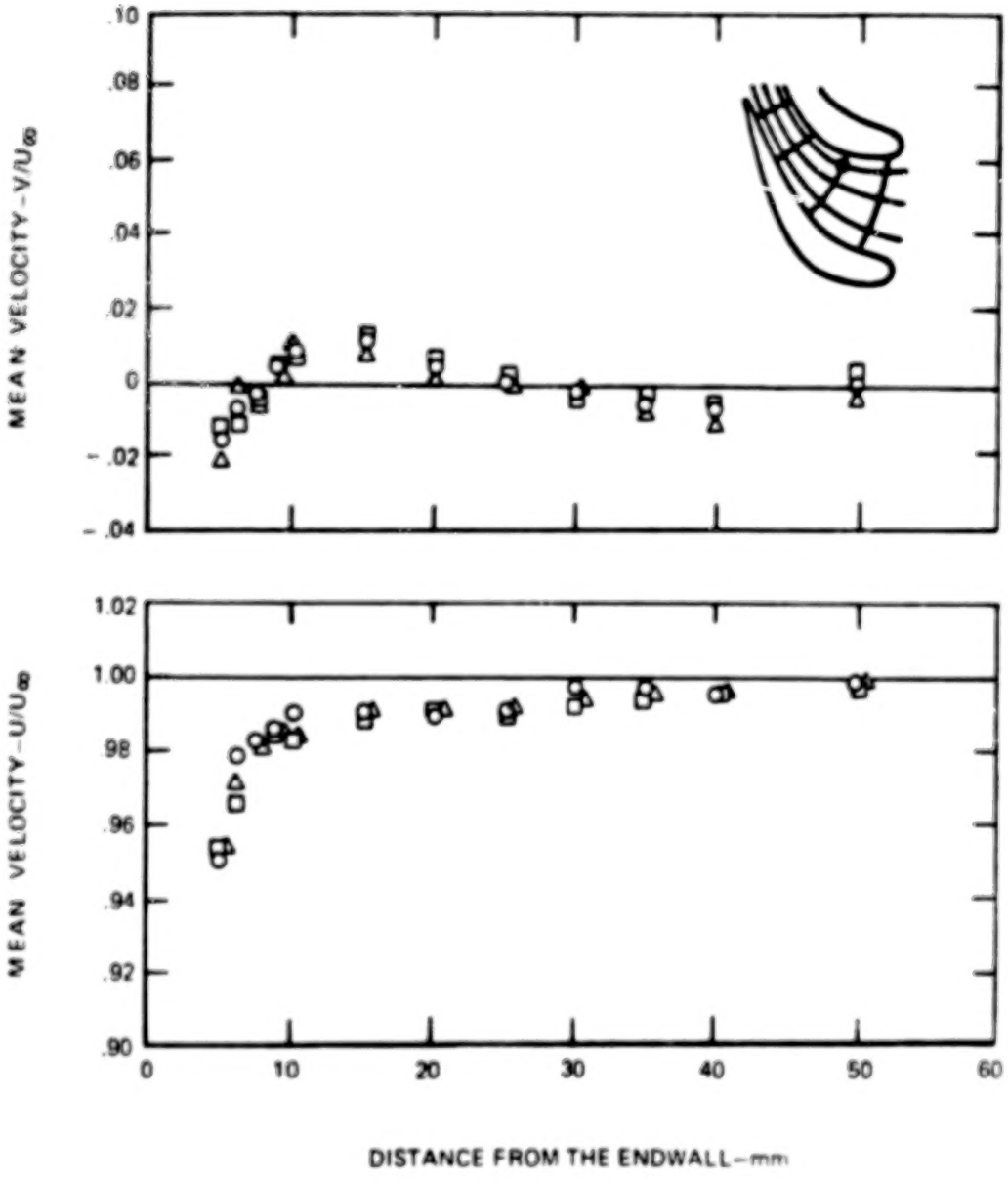

FIGURE A10-MEAN VELOCITIES VS. DISTANCE FROM THE ENDWALL
POSITION 4 , FLOW CONDITION C

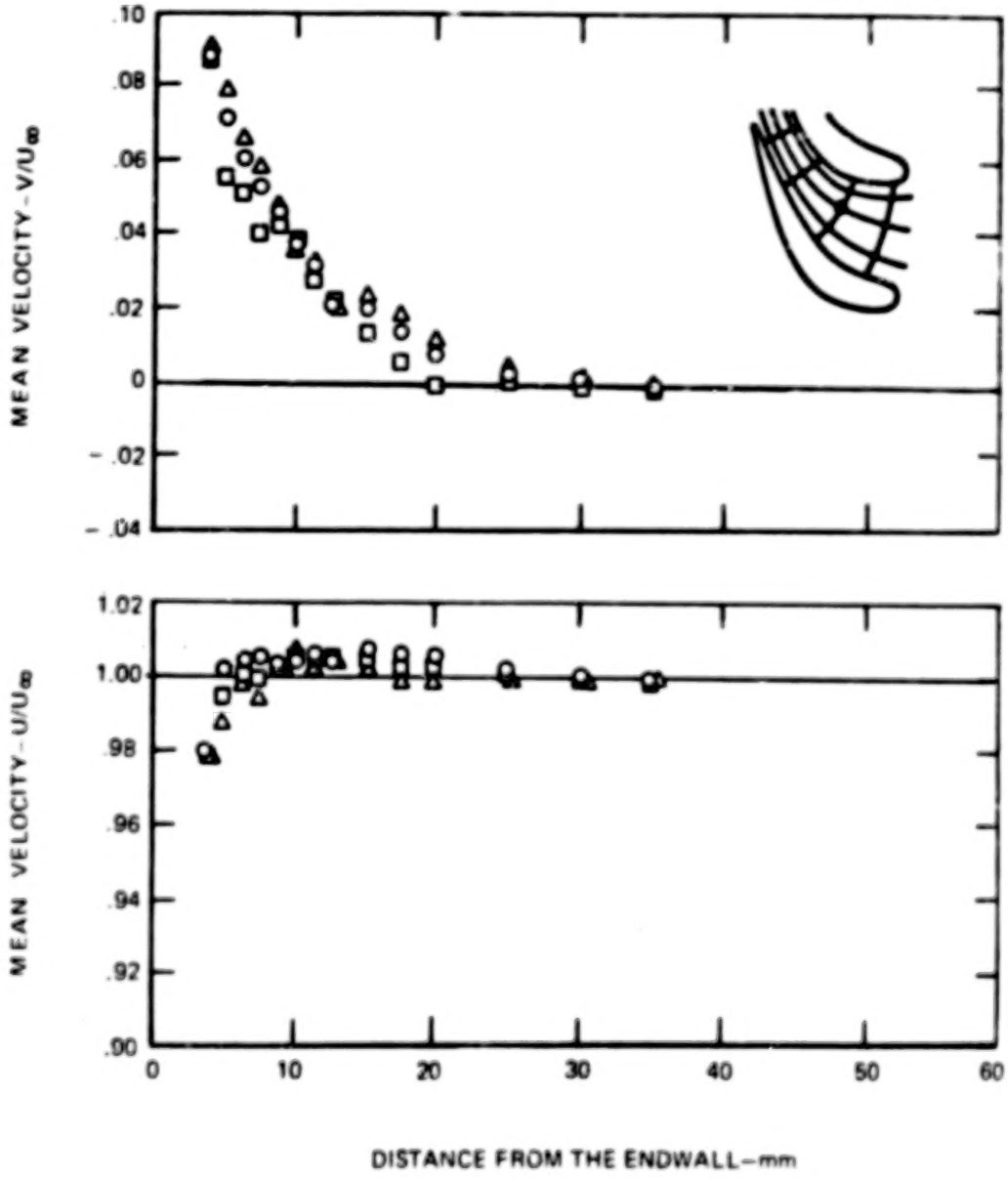

FIGURE A11–MEAN VELOCITIES VS. DISTANCE FROM THE ENDWALL
POSITION 5 , FLOW CONDITION C

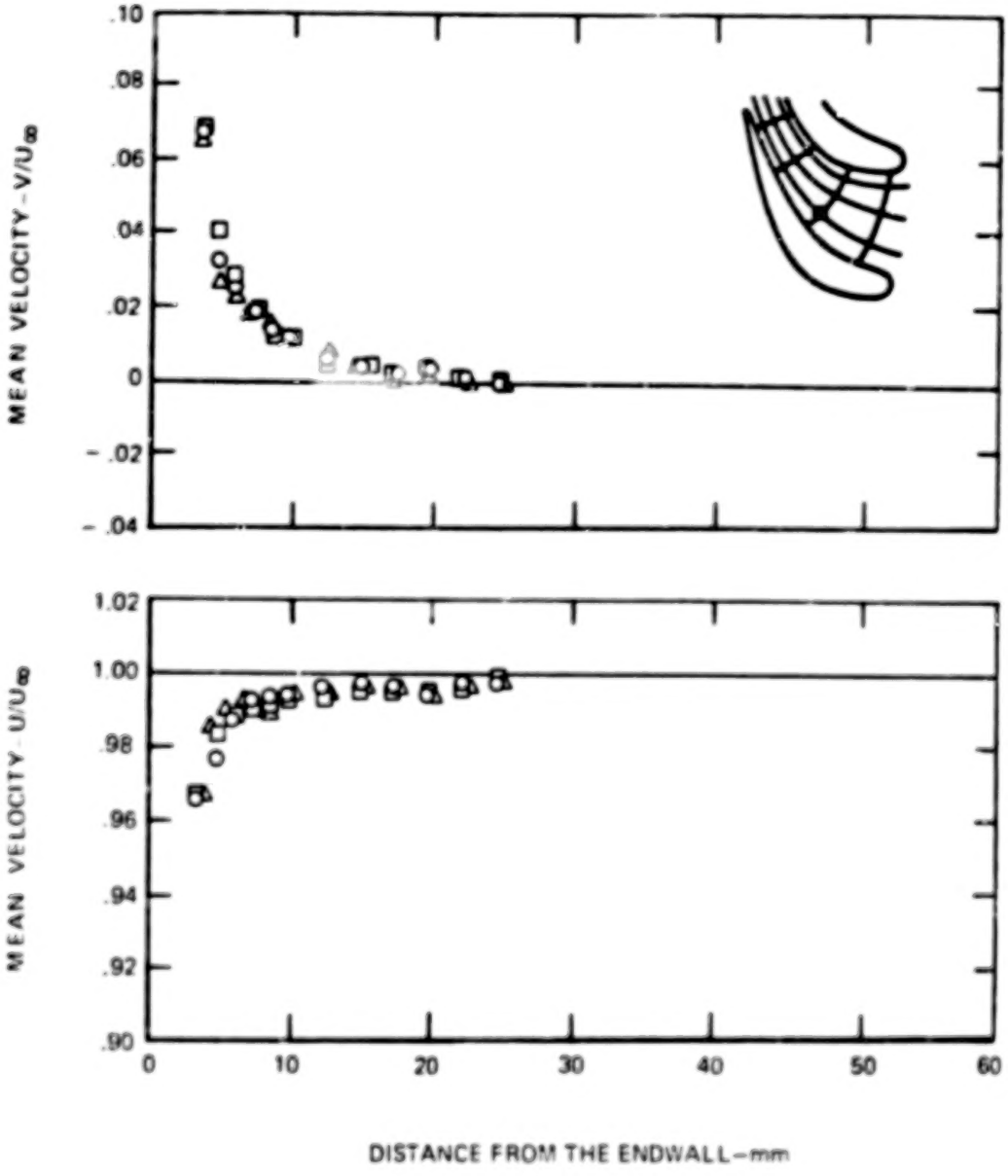

FIGURE A12 -MEAN VELOCITIES VS. DISTANCE FROM THE ENDWALL
POSITION 6 , FLOW CONDITION C

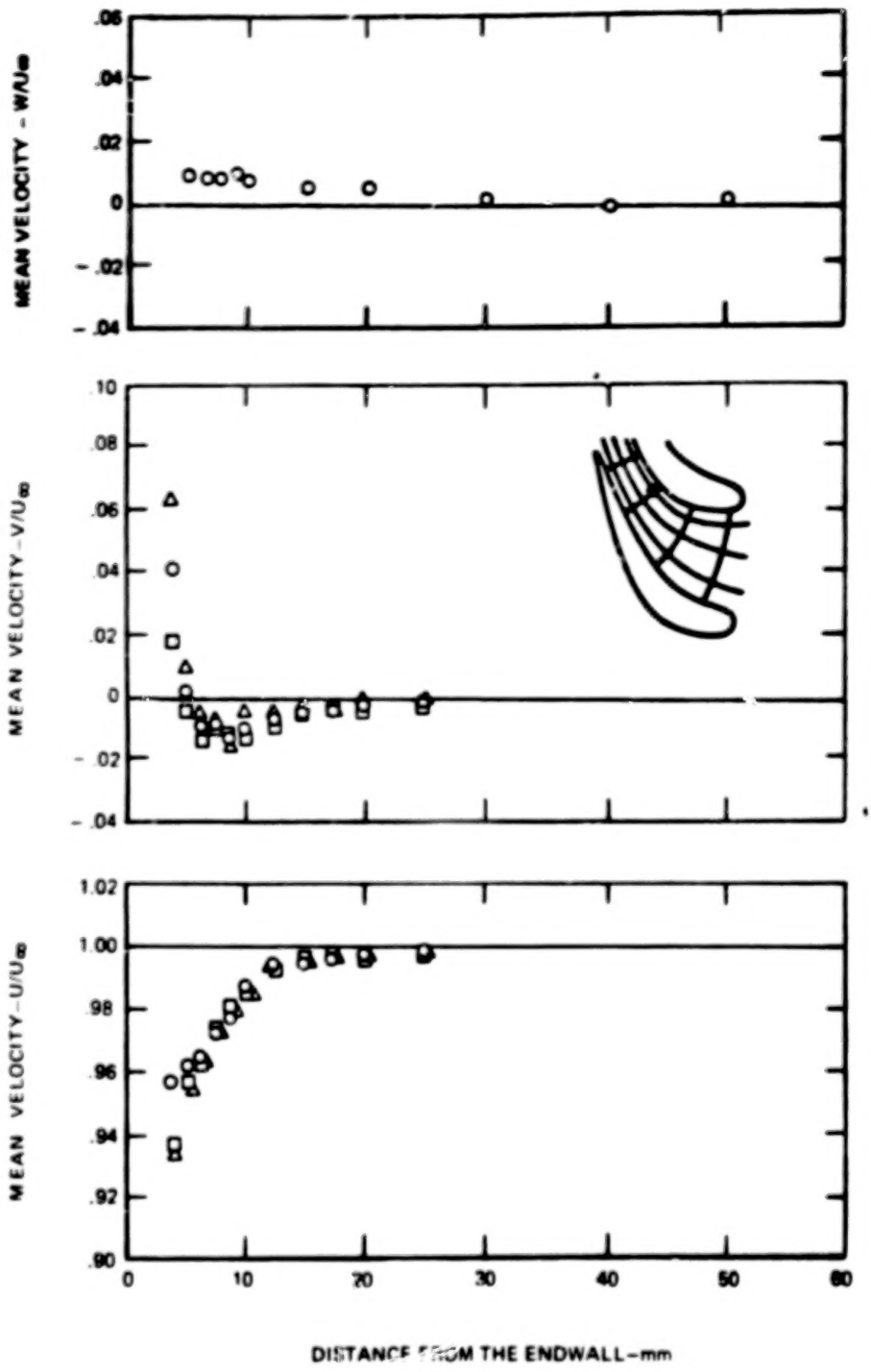

FIGURE A13–MEAN VELOCITIES VS. DISTANCE FROM THE ENDWALL POSITION 7, FLOW CONDITION C

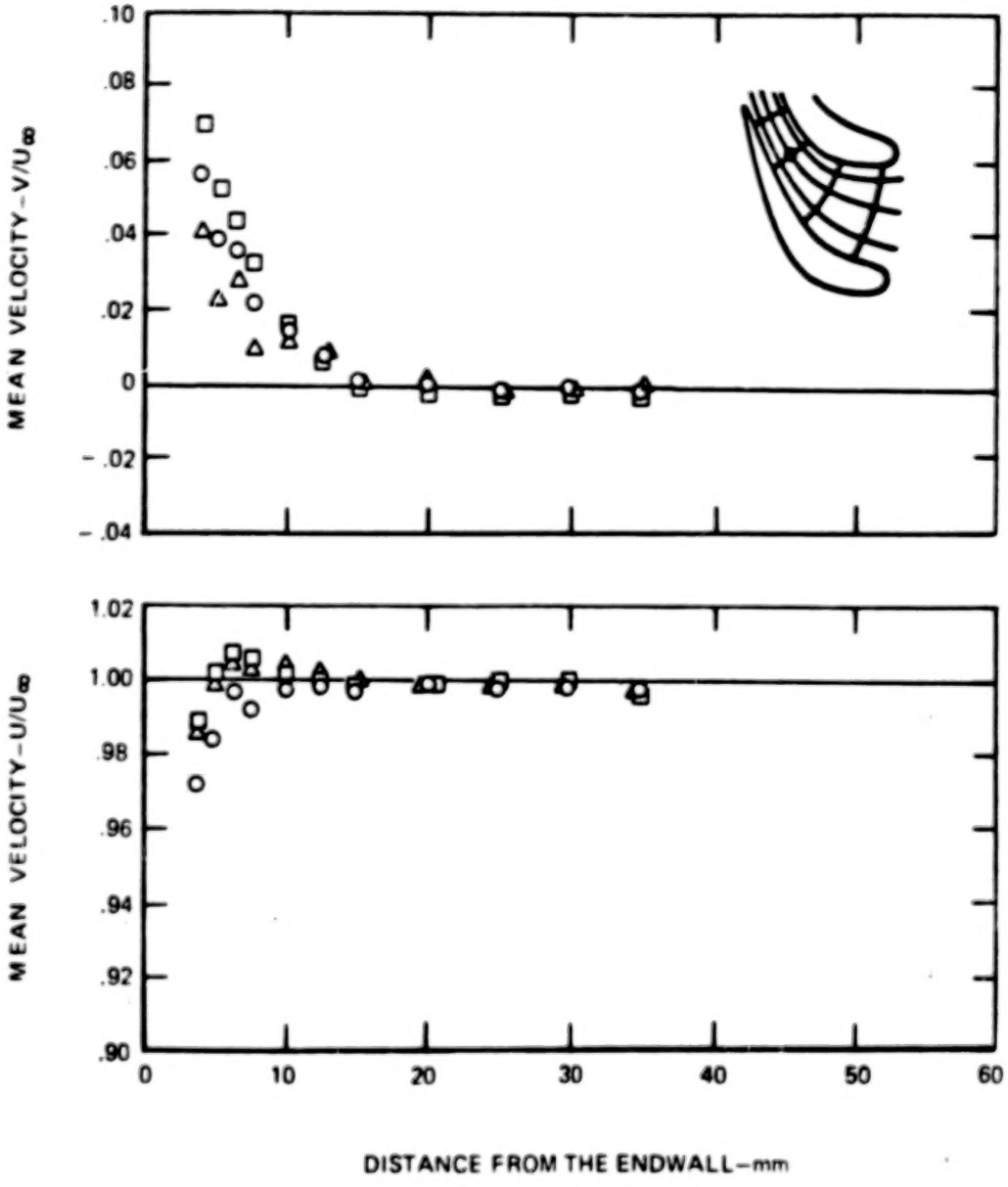

FIGURE A14--MEAN VELOCITIES VS. DISTANCE FROM THE ENDWALL POSITION 8 , FLOW CONDITION C

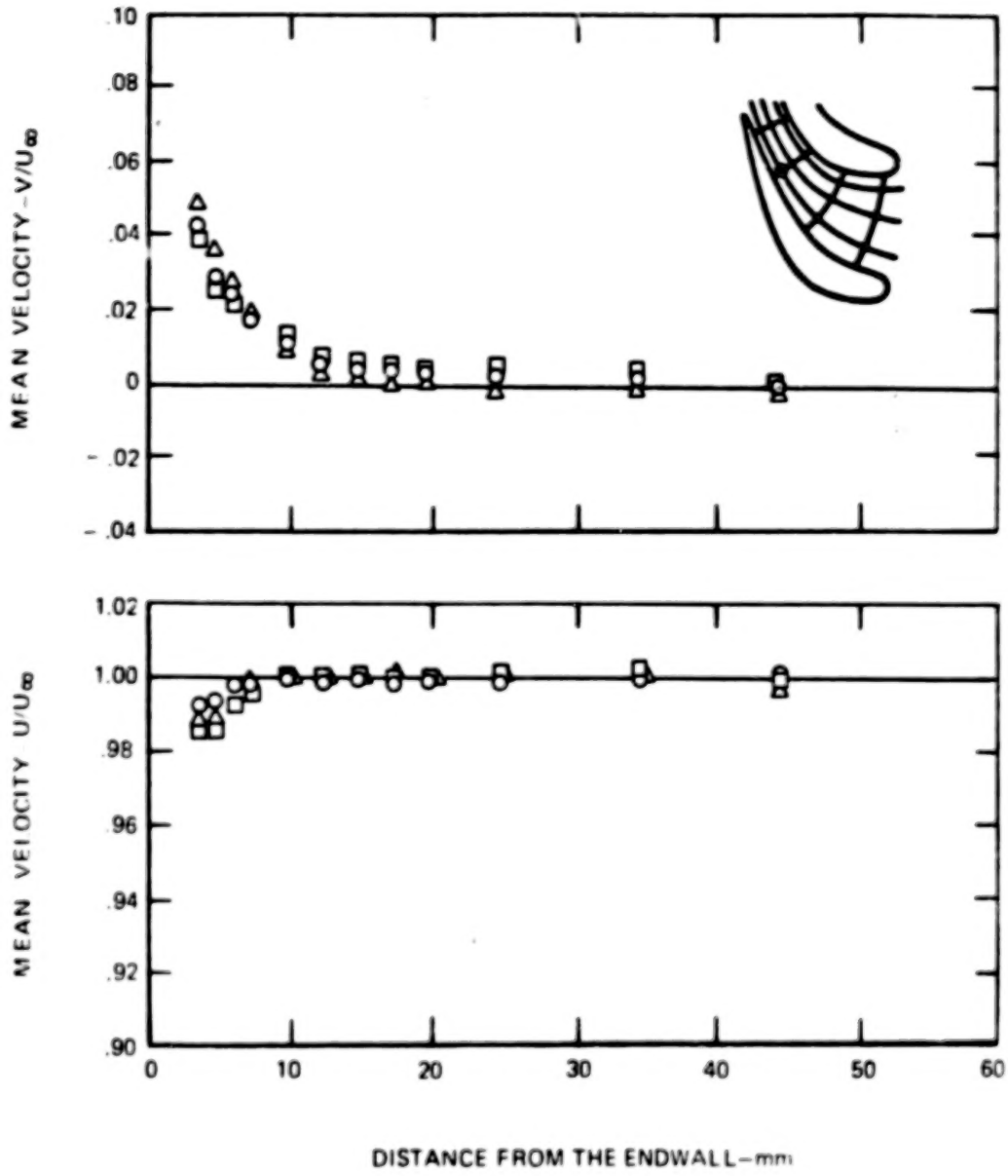

FIGURE A15–MEAN VELOCITIES VS. DISTANCE FROM THE ENDWALL POSITION 9 , FLOW CONDITION C

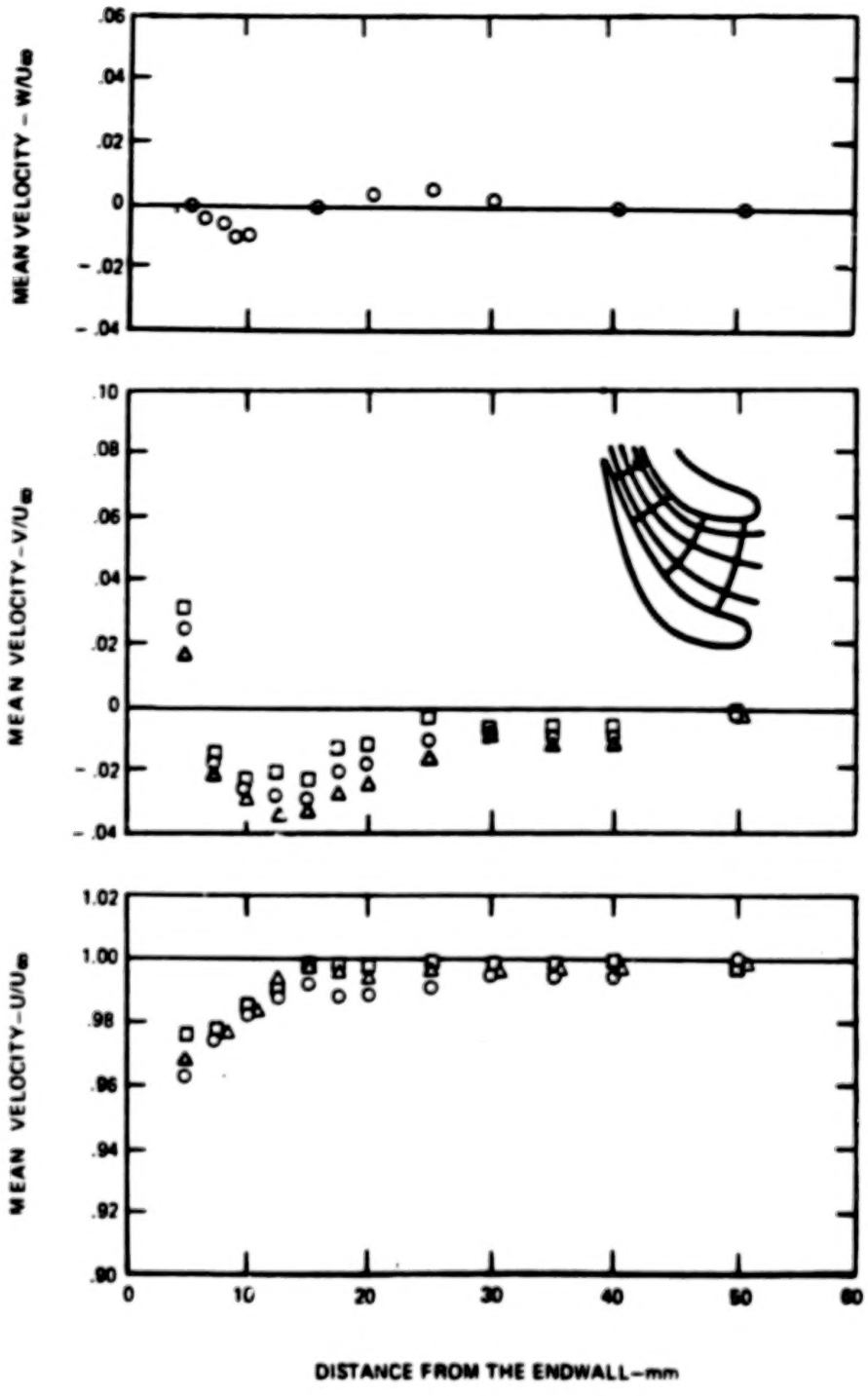

FIGURE A16–MEAN VELOCITIES VS. DISTANCE FROM THE ENDWALL POSITION 10, FLOW CONDITION C

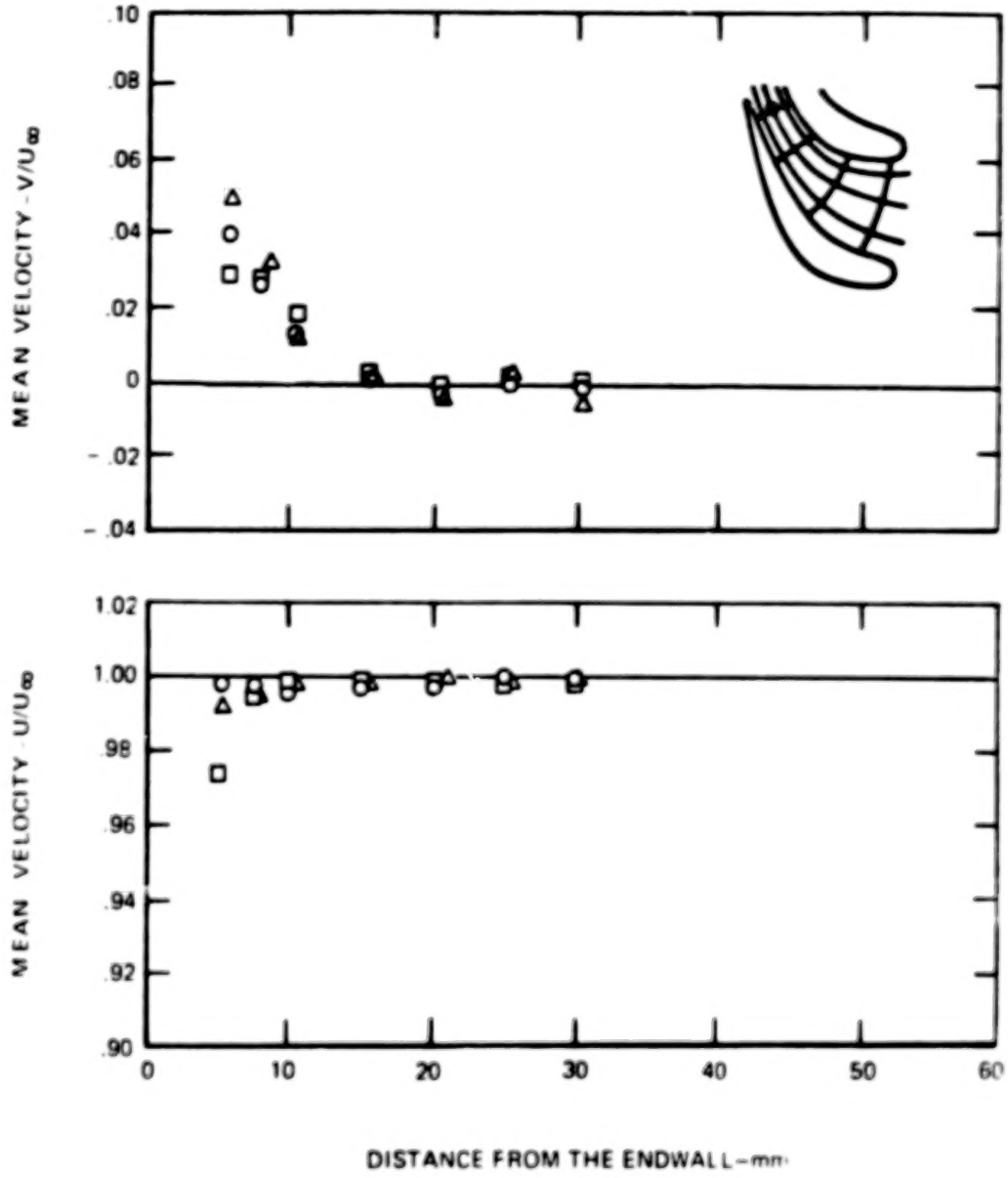

FIGURE A17–MEAN VELOCITIES VS. DISTANCE FROM THE ENDWALL
POSITION 11, FLOW CONDITION C

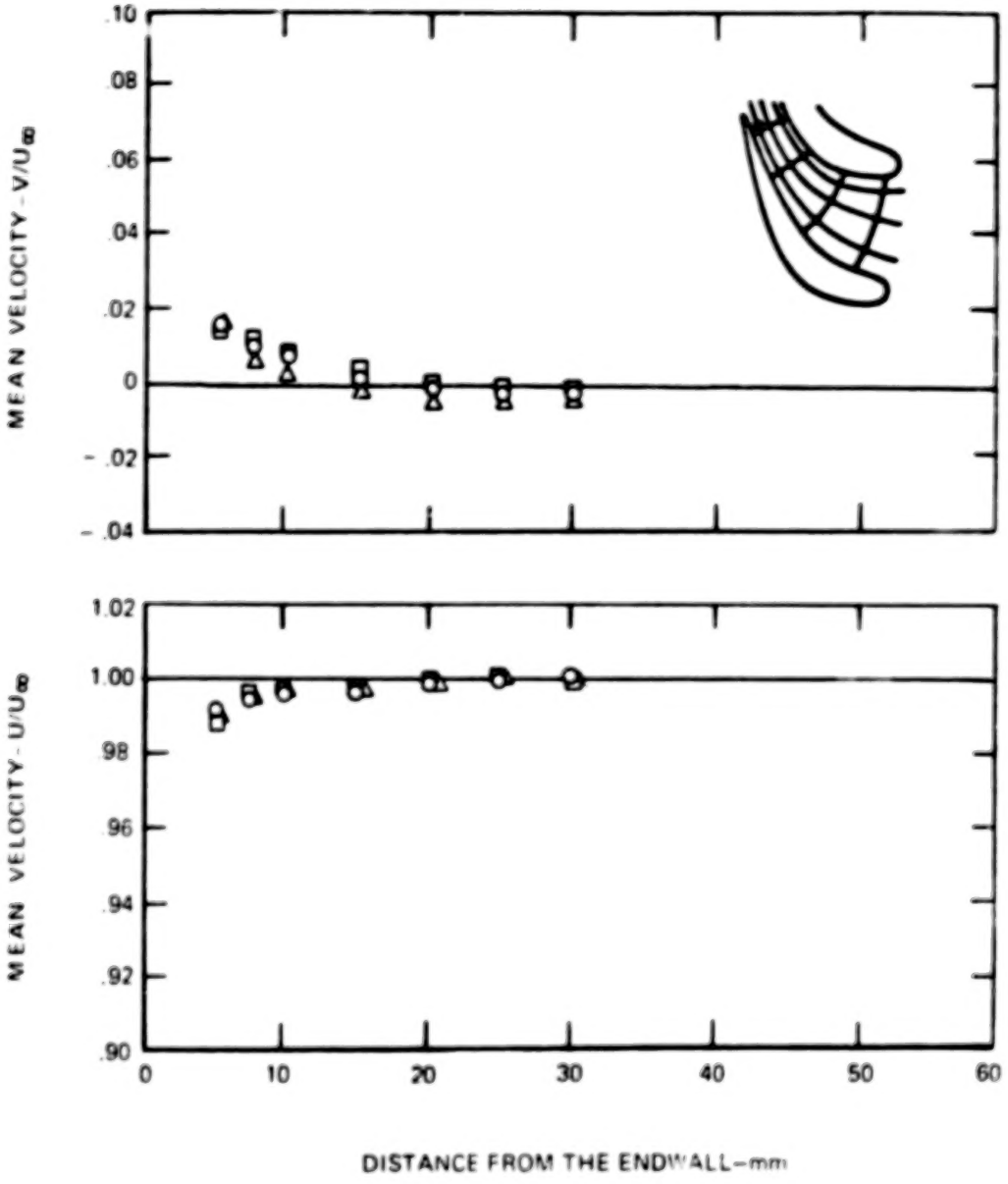

FIGURE A18–MEAN VELOCITIES VS. DISTANCE FROM THE ENDWALL POSITION 12 , FLOW CONDITION C

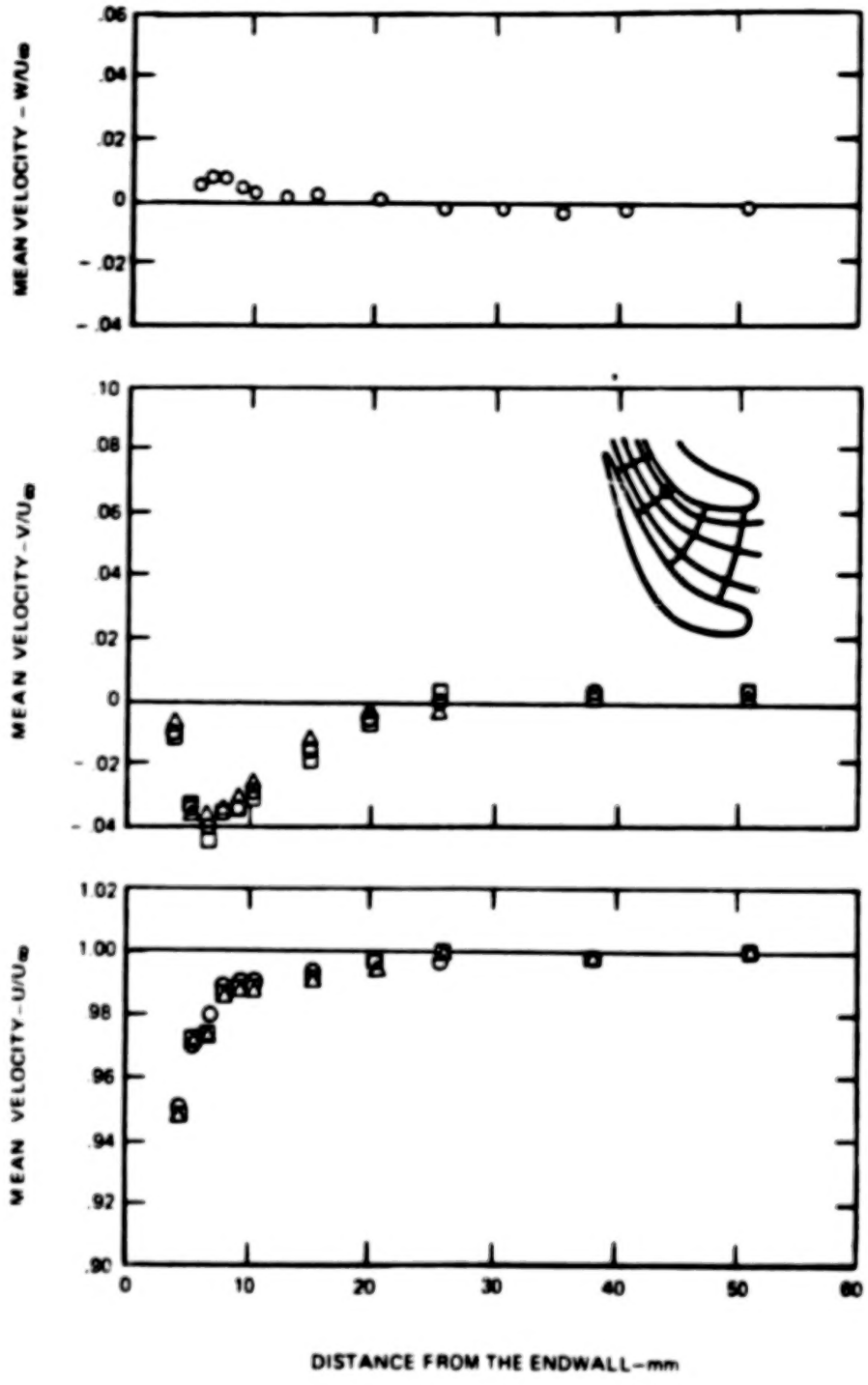

FIGURE A19—MEAN VELOCITIES VS. DISTANCE FROM THE ENDWALL POSITION 7, FLOW CONDITION B

APPENDIX B

Additional Inlet-Flow Measurements

Complicated, three-dimensional flows are sensitive to initial flow conditions. Because of this sensitivity, flows that are being studied for comparison with computational procedures should have a well documented initial condition. To provide such detailed documentation, additional measurements, for flow condition "A", were obtained in the first equi-potential plane of figure 6, at the locations listed in Table B1. The results are shown as longitudinal velocities (figure B1) and lateral velocities parallel to the endwall (figure B2) versus distance from the endwall. The data show that there were no abnormal features in the flow.

To further assist the verification of computational procedures, the flow angles and velocities of the core flow were measured for the twelve measurements locations of figure 6. These results are shown in Table B2.

TABLE B1

MEASUREMENT LOCATIONS

Location	x/C_x	z/s	x(mm)	z(mm)
A	0.110	-0.130	29.97	-27.18
B	0.106	-0.162	28.96	-34.04
1	0.106	-0.216	28.96	-45.21
C	0.105	-0.292	28.70	-61.21
2	0.122	-0.441	33.27	-92.46
D	0.152	-0.594	41.40	-124.46
3	0.177	-0.676	48.26	-141.73
E	0.197	-0.755	53.59	-158.24
F	0.211	-0.802	57.39	-167.62

x - axial distance from leading edge
z - tangential distance from leading edge
C_x - axial chord
s - pitch

TABLE B2

FLOW ANGLE AND VELOCITY MEASURED 76–mm FROM THE ENDWALL

Position	Flow Angle*	Local Velocity/Inlet Velocity**
1	-0° 52'	1.43
2	9° 56'	1.26
3	16° 34'	1.14
4	17° 8'	2.05
5	26° 7'	1.73
6	35° 34'	1.48
7	43° 27'	2.92
8	48° 14'	2.64
9	54° 33'	2.45
10	60° 17'	3.42
11	60° 48'	3.25
12	61° 55'	3.13

*Flow angle measured clockwise from horizontal, as viewed in Figure 6.
**Inlet velocity denotes the far-upstream, undisturbed velocity, approximately 29 m/sec.

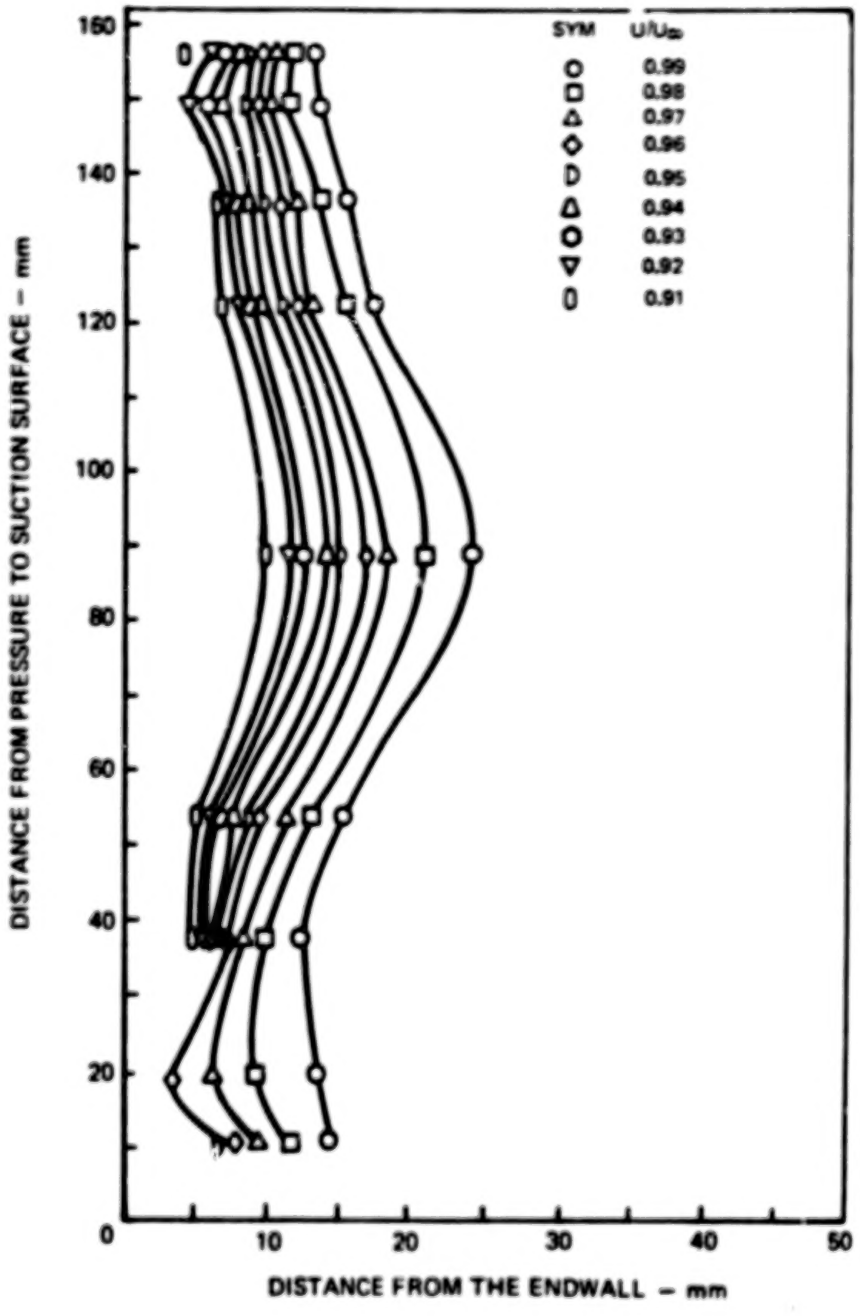

FIGURE B1– LONGITUDINAL VELOCITIES AT PLANE 1, FLOW CONDITION A

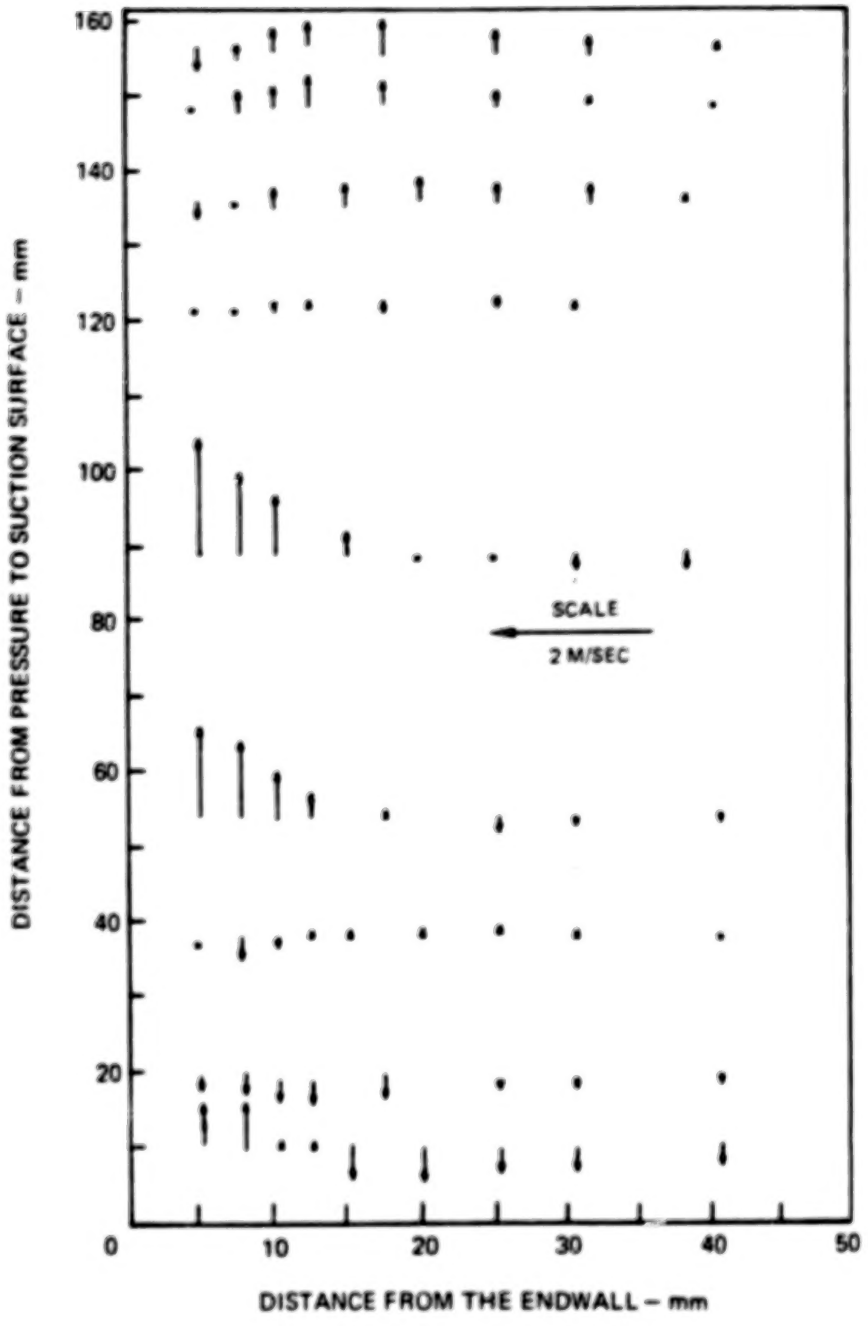

FIGURE B2– LATERAL VELOCITIES, V , AT PLANE 1, FLOW CONDITION A

APPENDIX C

List of Symbols

d	Diameter (LDV seeding particles)
$E(f)$	Power-spectral density
f	Frequency
K	Pressure-loss coefficient ($\Delta P/\frac{1}{2}\rho U^2$)
N_s	Stokes number (ν/fd_p^2) $\frac{1}{2}$
P	Pressure
t	Time
U, V, W	Velocity in directions x, y and z, respectively (U and V are also used to designate total velocity)
u', v', w'	Fluctuating component of above velocities
x	Spatial coordinate, in direction of core flow
y	Spatial coordinate, in direction from pressure to suction surface
z	Spatial coordinate, in direction from endwall to midspan
Λ_f	Integral length scale of longitudinal turbulence
ν	Kinematic viscosity
δ	Boundary-layer thickness
ρ	Density

Subscripts

$\mathrm{C_L}$	Centerline (such as test-section approach duct)
f	Fluid
p	Particle (LDV seeding)
t	Total (as in total pressure)
∞	Reference condition, core flow or total velocity

REFERENCES

1. Ainley, D. G.: Performance of Axial-flow Turbine. Proc. Inst. Mech. Engr., Vol. 154, 1948, pp. 230-244.

2. Rohlik, R. E.; Kofskey, M. G.; Allen, H. W.; and Herzig, H. Z.: Secondary Flows and Boundary-Layer Accumulations in Turbine Nozzles. NACA Rept. 1168, 1953. (Supersedes NACA TN 2871, 2909 and 2989.)

3. Herzig, H. Z.; Hansen, A. G.; and Costello, G. R.: A Visualization Study of Secondary Flows in Cascades. NACA Rept. 1163, 1954. (Supersedes NACA TN 2974.)

4. Blair, M. F.: An Experimental Study of Heat Transfer and Film Cooling on Large-Scale Turbine Endwalls. Trans. ASME, Vol. 96, Series C, No. 4, Dec. 1974, pp. 524-529.

5. Sjolander, S. A.: The Endwall Boundary Layer in an Annular Cascade of Turbine Nozzle Guide Vane. Tech. Rept. No. ME/A 75-4, Dept. Mech. & Aero Engr., Carleton Univ., Dec. 1975.

6. Langston, L. S.; Nice, M. L.; and Hooper, R. M.: Three-Dimensional Flow Within a Turbine Cascade Passage. Trans. ASME, Vol. 99, Series A, No. 1, Jan. 1977, pp. 21-28.

7. Dunham, J.: A Review of Cascade Data on Secondary Losses in Turbine. J. Mech. Eng. Sci., Vol. 12, No. 1, Feb. 1970, pp. 48-59.

8. Hansen, A. G.; and Herzig, H. Z.: Cross Flow in Laminar Incompressible Boundary Layers. NACA TN 3651, 1956.

9. Sowerby, L.: Secondary Flow in a Boundary Layer. Rept. No. 16832, British A.R.C., 1954.

10. Loos, H. G.: A Simple Laminar Boundary Layer With Secondary Flow. J. Aeron. Sci., Vol. 22, Jan 1955, pp. 35-40.

11. Mager, A.; and Hansen, A. G.: Laminar Boundary Layer over a Flat Plate in a Flow Having Circular Streamlines. NACA TN 2685, 1952.

12. Hawthorne, W. R.: Secondary Circulation in Fluid Flow. Proc. Roy. Soc. (London), Vol. 206, Series A, May 1951, pp. 374-387.

13. Hawthorne, W. R.: Flow in Bent Pipes. Proceedings of Seminar in Aeronautical Sciences, Nat. Aero. Lab., Bangalore, India, 1961, pp. 305-333.

14. Denton, J. D.: Time Marching Methods for Two- and Three-Dimensional Blade to Blade Flows. R. & M. No. 3775, British A. R. C., 1974.

15. Denton, J. D.: Extension of the Finite Area Time Marching Method to Three-Dimensions. Lecture Series 84, von Karman Institute, 1976.

16. Stuart, A. R.; and Hetherington, R.: The Solution of Three-Variable Duct Flow Equations. Fluid Mechanics, Acoustics, and Design of Turbomachinery, Part I, NASA SP-304, 1974, pp. 135-150; Discussion, pp. 151-153.

17. Briley, W. R.: Numerical Method of Predicting Three-Dimensional Steady Viscous Flow in Ducts. J. Comp. Phys., Vol. 14, No. 1, Jan. 1974, pp. 8-28.

18. Patankar, S. V.; and Spalding, D. B.: A Calculation Procedure for Heat, Mass and Momentum Transfer in Three-Dimensional Parabolic Flows. Int. J. Heat Mass Transfer, Vol. 15, Oct. 1972, pp. 1787-1806.

19. Ghia, U.; Ghia, K. N.; and Studerus, C. J.: A Study of Three-Dimensional Laminar Incompressible Flow in Ducts. Preprint 76-424, AIAA, July 1976.

20. Dodge, P. R.: Numerical Method for 2D and 3D Viscous Flows. AIAA Journal, Vol. 15, No. 7, July 1977, pp. 961-965.

21. Briley, W. R.; Kreskovsky, J. P.; and McDonald, H.: Computation of Three-Dimensional Viscous Flow in Straight and Curved Passages. Rept. R76-911841-9 (Contract Rept. NASC Contract N00019-74-C-0302) United Technologies Research Center, August 1976.

22. Reneau, L. R.; Johnston, J. P.; and Kline, S. J.: Performance and Design of Straight, Two-Dimensional Diffusers. Trans. ASME, Vol. 89, Series D, No. 1, March 1967, pp. 141-150.

23. Schubauer, G. B.; Spangenberg, W. G.; and Klebanoff, P. S.: Aerodynamic Characteristics of Damping Screens. NACA TN 2001, 1949.

24. Weighardt, K. E. G.: On the Resistance of Screens. Aeron. Quart., Vol. IV, Feb. 1953, pp. 186-192.

25. Bansod, P.; and Bradshaw, P.: The Flow in S-shaped Ducts. Aeron. Quart., Vol. XXIII, May 1972, pp. 131-140.

26. Dryden, H. L.: A Review of the Statistical Theory of Turbulence. Quart. Appl. Math., Vol. 1, No. 1, April 1943, pp. 7-42.

27. Frenkiel, F. N.: Effects of Wire Length in Turbulence Investigations With a Hot-Wire Anemometer. Aeron. Quart., Vol. V, May 1954, pp. 1-24.

28. Hinze, J. O.: Turbulence; An Introduction to Its Mechanism and Theory, McGraw-Hill Book Co., Inc., 1959.

29. Burbank, P. B.; Newlander, R. A.; and Collins, I. K.: Heat Transfer and Pressure Measurements on Attached Protuberances in a Supersonic Turbulent Boundary Layer at Mach Numbers of 2.65, 3.51 and 4.44. NASA TN-D-1372, 1962.

30. Bělík, L.: The Secondary Flow About Circular Cylinders Mounted Normal to a Flat Plate. Aeron. Quart., Vol. XXIV, Feb. 1973, pp. 47-54.

31. Ram, V. V.: Untersuchungen uder die Eckengrenzschict an einem Kreiszylinder mit Seitenwand. Bericht 63/64, Institut fur Stromungsmechanik, Technische Hochschule Braunschweig, 1963.

32. Peake, D. J.; and Galway, R. D.: The Three-Dimensional Separation of a Plane Incompressible Laminar Boundary Layer Produced by a Circular Cylinder Mounted Normal to a Flat Plate. Aeron. Rept. LR-428, Nat. Aero. Est., Ottawa, May 1965.

33. East, L. F.; and Hoxey, R. P.: Low-Speed Three-Dimensional Turbulent Boundary Layer Data. Parts 1 and 2. R. & M. No. 3653, British A.R.C., 1971.

34. Dechow, R.; and Felsch, K. O.: Measurements of the Mean Velocity and the Reynolds Stress Tensor in a Three-Dimensional Turbulent Boundary Layer Induced by a Cylinder Standing on a Flat Wall. Proceedings of Symposium on Turbulent Shear Flow - Penn. State Univ., April 1977, pp. 9.11-9.20.

35. Hornung, H. G.; and Joubert, P. M.: The Mean Velocity Profile in Three-Dimensional Turbulent Boundary Layers. J. Fluid Mech., Vol. 15, Part 3, March 1963, pp. 368-384.

36. Preston, J. H.: The Minimum Reynolds Number for a Turbulent Boundary Layer and the Selection of a Transition Device. J. Fluid Mech., Vol. 3, Part 4, Jan. 1958, pp. 373-384.

37. Klebanoff, P. S.; and Diehl, Z. W.: Some Features of Artificially Thickened Fully Developed Turbulent Boundary Layers with Zero Pressure Gradient, NACA Rept. 1110, 1952.

38. Morkovin, M. V.: An Approach to Flow Engineering Via Functional Flow Modules. Rept. No. JIT-Themis-R72-1-1972 AFORS-TR-72-0908 (Contract F44620-69-C-0022), Dept. Mechanics, Mech, and Aero Engr., Illinois Inst. of Tech., Chicago, 1972.

39. Stevenson, W. H.; and Thompson, H. D., eds.: The Use of the Laser Doppler Velocimeter for Flow Measurements. (N00014-67-0226-0005) Proceedings of a Project Squid Workshop. Purdue Univ., March 9-10, 1972.

40. Thompson, H. D.; and Stevenson, W. H., eds.: Proceedings of the Second International Workshop on Laser Velocimetry. Bulletin No. 144, Eng. Expt. Sta., Purdue Univ., March 27-29, 1974.

41. Eckert, E. R. G., ed.: Minnesota Symposium on Laser Anemometry Proceedings. Dept. of Conf. Continuing Education and Extension, Univ. of Minn., Oct. 22-24, 1975 (published Jan. 1976).

42. Applications of Non-Intrusive Instrumentation in Fluid Flow Research. AGARD-CP-193 (Saint-Louis, France), May 3-5, 1976.

43. Laser Optical Measurement Methods for Aero Engine Research and Development. AGARD-LS-90 (Trenton, New Jersey, USA), Aug. 25-26, 1977. Also (London, UK), Aug. 30-31, 1977 and (Urbino, Italy), Sept. 5-6, 1977.

44. Durst, F.; Melling, A.; and Whitelaw, J. H.: Principles and Practices of Laser-Doppler Anemometry. Academic Press, 1976.

45. Watrasiewicz, B. M.; and Rudd, M. J.: Laser Doppler Measurements. Butterworths (Publishers) Inc., 1976.

46. Melling, A.; and Whitelaw, J. H.: Seeding of Gas Flow for Laser Anemometry. DISA Information, No. 15, Oct. 1973, pp. 5-14.

47. Marteney, P. J.: Experimental Investigation of the Opacity of Small Particles. NASA CR-211, Apr. 1965.

48. Seasholtz, R. G.: Laser Doppler Velocimeter System for Turbine Stator Cascade Studies and Error Analysis of Statistical Biasing Errors. NASA TN D-8297, 1977.

49. Whiffen, M. C.: Polar Response of an LV Measuring Volume. Minnesota Symposium on Laser Anemometry Proceedings. Dept. of Conf. Continuing Education and Extension, Univ. of Minn., Oct. 22-24, 1975 (published Jan. 1976).

50. Bradshaw, P.: An Introduction to Turbulence and its Measurement. Pergamon Press, Inc., 1971.

51. Milne-Thomson, L. M.: Theoretical Hydrodynamics. Fifth ed., The Macmillan Co., 1969.

52. Marchal, Ph.; and Sieverding, C. H.: Secondary Flow Within Turbomachinery Bladings. Secondary Flows in Turbomachinery. AGARD-CP-214 (The Hague, The Netherlands), Mar. 28-30, 1977.

53. Klebanoff P. S.: Characteristics of Turbulence in a Boundary Layer With Zero Pressure Gradient, NACA TN 3178, 1954.

1. Report No.	2. Government Accession No.	3. Recipient's Catalog No.
NASA CR-3067		

4. Title and Subtitle	5. Report Date
STUDY OF MEAN- AND TURBULENT-VELOCITY FIELDS IN A LARGE-SCALE TURBINE-VANE PASSAGE	February 1979
	6. Performing Organization Code

7. Author(s)	8. Performing Organization Report No.
Douglas A. Bailey	
	10. Work Unit No.
9. Performing Organization Name and Address	
United Technologies Research Center East Hartford, Connecticut	11. Contract or Grant No. NAS3-19752
	13. Type of Report and Period Covered Contractor Report
12. Sponsoring Agency Name and Address	
National Aeronautics and Space Administration Washington, D.C. 20546	14. Sponsoring Agency Code

15. Supplementary Notes

Final report. Project Manager, Eric R. McFarland, Fluid System Components Division, NASA Lewis Research Center, Cleveland, Ohio 44135.

16. Abstract

An experimental investigation was conducted on the mean- and turbulent-velocity fields in a large-scale turbine inlet-guide-vane passage. The experiment was performed in a 210-mm pitch, 272-mm axial chord model in the United Technologies Research Center (UTRC) Low-Speed Wind Tunnel at an inlet Mach number of 0.07. The Reynolds number, based on the axial chord and the inlet velocity, matched seal-level, take-off conditions for modern gas-turbine engines. Laser-doppler velocimetry, and to a lesser extent hot-wire anemometry, was employed to measure three components of the mean velocity and the six turbulent stresses at four planes within the passage. One variation in the turbulent inlet boundary-layer thickness and one variation in the blade aspect ratio (span/axial chord) were studied. A longitudinal vortex (passage vortex) was clearly identified in the exit plane of the passage for the three test cases. The maximum turbulence intensities within the longitudinal vortex were found to be on the order of 2 to 4 percent, with large regions appearing nonturbulent. Since a turbulent wall boundary layer was the source of vorticity that produced the passage vortex, these low turbulence levels were not anticipated. For the three test cases studied, the lateral velocity field extended significantly beyond the region of the longitudinal velocity defect. Changing the inlet boundary-layer thickness produced a difference in the location, the strength and the extent of the passage vortex. Changing the aspect ratio of the blade passage had a measurable but less significant effect.

17. Key Words (Suggested by Author(s))	18. Distribution Statement
Secondary flows LDV flow measurements Experimental flow measurements Turbine passage flow	Unclassified - unlimited STAR Category 07

19. Security Classif. (of this report)	20. Security Classif. (of this page)	21. No. of Pages	22. Price*
Unclassified	Unclassified	121	A06

* For sale by the National Technical Information Service, Springfield, Virginia 22161

NASA-Langley, 1979

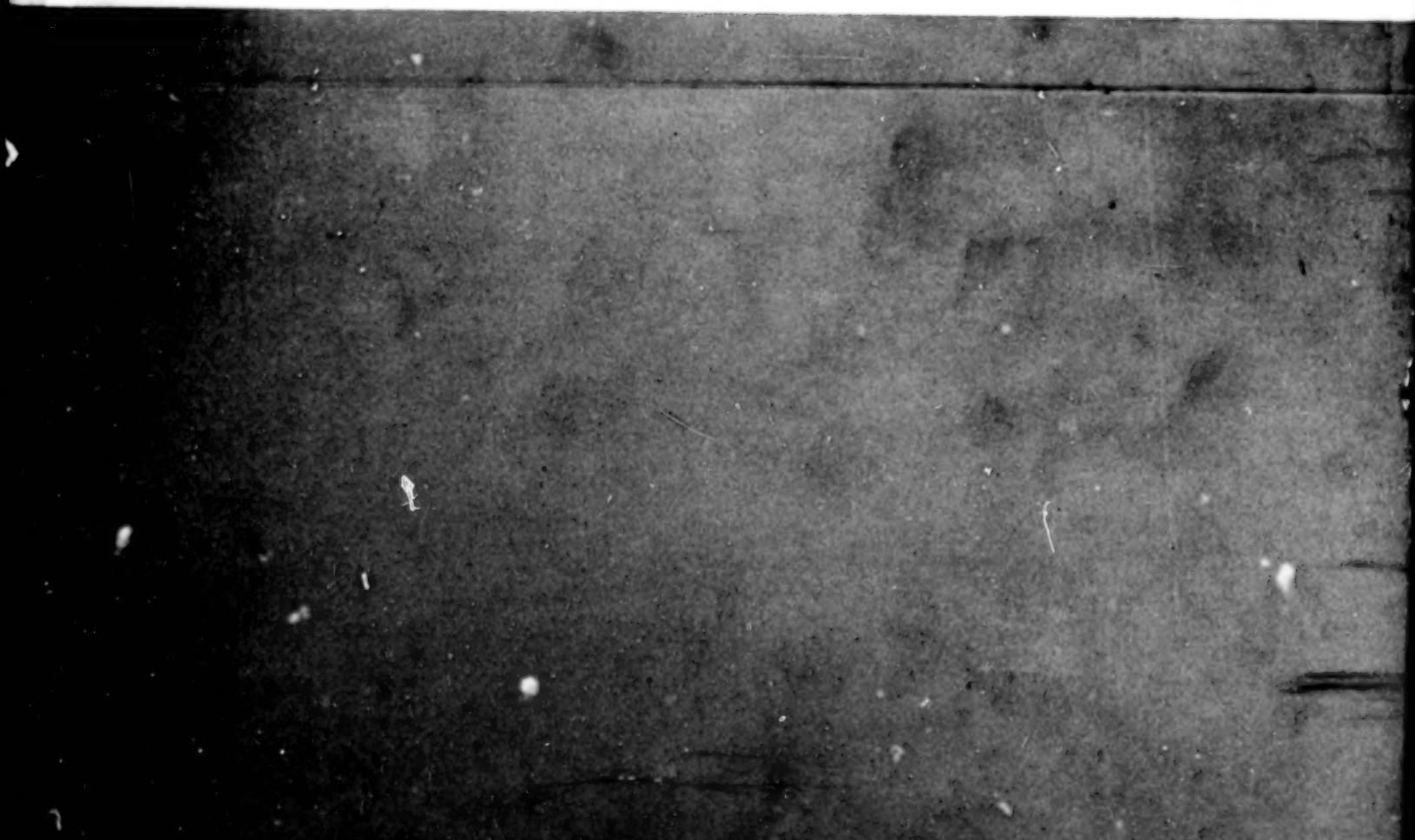

END

June 15, 1981